Electronic structures of twisted two-dimensional materials studied by angle-resolved photoemission spectroscopy

Ding Pei

St Hugh's College

University of Oxford

A thesis submitted for the degree of

Doctor of Philosophy

Trinity 2021

Acknowledgements

I would like to take this opportunity to express my gratitude to all those who accompanied and helped me during my DPhil journey in Oxford.

First, I would like to thank my supervisor Prof. Yulin Chen. He always keeps a high standard of research projects and inspires me to think critically on experimental results. He always encourages me to explore the frontier of condensed matter physics and supports me during the difficult time. I really appreciate him for providing this platform to realize my ideas and carry out my research.

I want to thank my former and present colleagues in Chen's group in Oxford, including Niels Schröeter, Cheng Chen, Yiwei Li, Han Peng, Sandy Ekahana, Chaofan Zhang, Jieyi Liu, Huijun Zheng and Shanmei He. Niels inspired me to pursue my research goal eagerly instead of passively waiting for the chance. Cheng introduced me to the ARPES technique and taught me the experimental skills, which helped me lay the first stone to be an experimentalist. Yiwei showed me how to analyse data systematically. I would like to give thanks to Jieyi and Huijun who helped proofread this thesis. It has been a great pleasure to work with these talented guys.

I am grateful for the help from all the members in Chen's group around the world. Especially, I appreciate the assistance from Prof. Lexian Yang in Tsinghua University, who has been always willing to discuss with me in detail about my projects, and helped me a lot in the manuscript preparation of BiCuSO and PtGa. I also thank Zhongxu Yin in Tsinghua University for his help in proofreading.

My gratitude is given to all collaborators and friends. Within the list there are all the experimentalists that prepared high quality samples used in our studies: Prof. Ning Wang, Dr. Liheng An, Zishu Zhou, Prof. Yanbin Chen, Dr. Yangyang Lv, etc.; all theorists that performed either analytical or numerical calculations for our studies: Dr. Joshua Thompson, Dr. Marcin Mucha- Kruczyński, Dr. Jianpeng Liu, Dr. Zhihai He, Prof. Gang Li, Dr. Yunyouyou Xia, Dr. Yan Sun, Dr. Qun Yang, etc.; all staff scientists in the synchrotron facilities: Dr. Cephise Cacho, Dr. Pavel Dudin, Dr. Sungwon Jung, Dr. Matthew Watson, Dr. Alexey Barinov, Dr. Viktor Kandyba, Dr. Alessio Giampietri, etc.; STM guys: Prof. Jiamin Xue and Binbin Wang.; my friends in Oxford Physics: Dr. Shilei Zhang, Jheng-Cyuan Lin, Dr. Junjie Liu, Ryuji Fujita, Jiahao Chen, etc.

Finally, I would express my special thanks to my parents, Jingwen Pei and Furong Yuan, for their unconditional love and support. All I achieved during my DPhil years also belong to them.

Abstract

This thesis is a summary of my DPhil research projects, in which we describe the angle-resolved photoemission spectroscopy (ARPES) study on the electronic structure of twisted two-dimensional and other crystalline materials:

1. Twisted van der Waals heterostructures have recently been proposed as a condensed-matter platform for realizing controllable quantum models due to the low-energy moiré bands with specific charge distributions in moiré superlattices. Here, using angle-resolved photoemission spectroscopy with sub-micron spatial resolution (μ-ARPES) and scanning tunneling microscopy (STM), we performed a systematic investigation on the electronic structure of 5.1° twisted bilayer WSe_2, which was previously reported to host correlated insulating and zero-resistance states. We only observe the Γ-valley moiré bands but not the proposed K-valley moiré band. In addition, we have unambiguously identified the real-space honeycomb- and kagome-shaped charge distributions at the moiré length scale, which are associated with Γ-valley moiré bands. Our results not only reveal the valley dependent moiré-modified electronic structure, but also highlight the Γ-valley moiré bands as a promising platform for exploring strongly correlated physics in emergent honeycomb and kagome lattices .

2. The graphene-based heterostructures host competing periodicities that are favorable for Umklapp scattering. Using μ-ARPES, we have revealed that Umklapp scattering is a universal process in the large angle twisted graphene regardless of the twist angle and the number of layers, by showing the replica Dirac cones in the 30° twisted trilayer and 33° twisted bilayer graphene. We have also confirmed the existence of Umklapp scattering in the graphene/WSe_2 heterostructures with 11° and 14° twist angles. Interestingly, we find that 11° could be a magic angle for the graphene/WSe_2 heterostructure, which can lead to the formation of flat band via the second order Umklapp scattering.

3. BiCuChO (Ch=S and Se) family are promising thermoelectric materials with a high figure of merit, and also have been predicted as possible parent compounds for unconventional superconductivity. Using high-resolution ARPES, we have confirmed the co-existence of heavy and light hole-bands near the valence band maximum, which is favorable for maintaining the large Seebeck coefficient and the good electrical conductivity simultaneously. We also observed the predicted flat bands closing to the Fermi level, which can dramatically enhance the charge density upon p-type doping. Further polarization dependent study reveals the quasi-one-dimensional orbital configuration of the valence band top. Our results contribute to a better understanding of the thermoelectric properties and serve as an important reference for searching for superconductivity in BiCuChO family.

4. Chiral semimetals the PtGa family (PtGa, PtAl,PdGa) are expected to host topologically non-trivial electronic structure, such as the multi-fold band crossings

with large Chern number at high symmetry points connected by long Fermi-arc surface states. Using ARPES in different energy ranges (from vacuum ultraviolet to soft X-ray), we report a comprehensive study on their electronic structures. By comparing with our ab initio calculation, we identified the six-fold and four-fold fermions at the R and Γ points, respectively. Besides, we observed iconic topological surface states with chiral edge modes around the Γ point, forming long Fermi-arc winding across the Brillouin zone. Surprisingly, we found the anomalous polarization dependence of the observed arc states in PtGa, the origin of which could be rooted in the chiral crystal structure.

List of Related Publications

Twisted two-dimensional materials

D. Pei, B. Wang, Z. Zhou, Z. He, L. An, S. He, C. Chen, Y. Li, L. Wei, A. Liang, J. Avila, P. Dudin, A. Barinov, V. Kandyba, A. Giampietri, M. Cattelan, Z. Liu, J. Liu, H. Weng, N. Wang, J. Xue, Y. Chen
"Observation of Γ-valley moiré bands and emergent hexagonal lattice in twisted transition metal dichalcogenides"
submitted

J. J. P. Thompson, **D. Pei**, H. Peng, H. Wang, N. Channa, H. L. Peng, A. Barinov, N. B. M. Schröter, Y. Chen, M. Mucha-Kruczyński
"Determination of interatomic coupling between two-dimensional crystals using angle-resolved photoemission spectroscopy"
Nature Communications, 11, 3582(2020)

L. An, X. Cai, **D. Pei**, M. Huang, Z. Wu, Z. Zhou, J. Lin, Z. Ying, Z. Ye, X. Feng, R. Gao, C. Cacho, M. Watson, Y. Chen, N. Wang
"Interaction effects and superconductivity signatures in twisted double-bilayer WSe_2"
Nanoscale Horizons, 5, 1309-1316(2020)

L. Sun, Z. Wang, Y. Wang, L. Zhao, Y. Li, B. Chen, S. Huang, S. Zhang, W. Wang, **D. Pei**, H. Fang, S. Zhong, H. Liu, J. Zhang, L. Tong, Y. Chen, Z. Li, M. H. Rümmeli, K. S. Novoselov, H. Peng, L. Lin, Z. Liu
"Hetero-site nucleation for growing twisted bilayer graphene with a wide range of twist angles"
Nature Communications, 12, 2391(2021)

BiCuChO family

D. Pei, Y.-Y. Lv, Y. Y. Y. Xia, Y. W. Li, J. Y. Liu, N. B. M. Schröter, C. Cacho, Z. K. Liu, L. X. Yang, G. Li, Y. B. Chen, and Y. L. Chen
"Electronic structure of a thermoelectric material: BiCuSO"
Physical Review B, 103, 245121(2021)

PtGa family

N. B. M. Schröter, **D. Pei**, M. G. Vergniory, Y. Sun, K. Manna, F. de Juan, J. A. Krieger, V. Süss, M. Schmidt, P. Dudin, B. Bradlyn, T. K. Kim, T. Schmitt, C. Cacho, C. Felser, V. N. Strocov, Y. Chen
"Chiral topological semimetal with multifold band crossings and long Fermi arcs"

Nature Physics, 15, 759–765(2019)

N. B. M. Schröter, S. Stolz, K. Manna, F. de Juan, M. G. Vergniory, J. A. Krieger, **D. Pei**, T. Schmitt, P. Dudin, T. K. Kim, C. Cacho, B. Bradlyn, H. Borrmann, Ma. Schmidt, R. Widmer, V. N. Strocov, C. Felser
"Observation and control of maximal Chern numbers in a chiral topological semimetal"
Science, 369, 6500, 179-183(2020)

P. Sessi, F.-R. Fan, F. Küster, K. Manna, N. B. M. Schröter, J.-R. Ji, S. Stolz, J. A. Krieger, **D. Pei**, T. K. Kim, P. Dudin, C. Cacho, R. Widmer, H. Borrmann, W. Shi, K. Chang, Y. Sun, C. Felser, S. S. P. Parkin
"Handedness-dependent quasiparticle interference in the two enantiomers of the topological chiral semimetal PdGa"
Nature Communications, 11, 3507(2020)

Contents

List of Figures

List of Abbreviations

1D . . . . . One dimensional

2D . . . . . Two dimensional

2D . . . . . Three dimensional

AFM . . . . . Atomic force microscopy

ARPES . . . . Angle-resolved photoemission spectroscopy

BS . . . . . Bulk state

BZ . . . . . Brillouin zone

CC . . . . . Constant-current

CCD . . . . . Charge-coupled device

CDW . . . . . Charge density wave

CEC . . . . . Constant energy contour

CH . . . . . Constant-height

CVD . . . . . Chemical vapor deposition

DC . . . . . Dirac cone

DFT . . . . . Density functional theory

DOS . . . . . Density of states

$\mathbf{E}_B$ . . . . . Binding energy

$\mathbf{E}_F$ . . . . . Fermi level

$\mathbf{E}_k$ . . . . . Kinetic energy

EDC . . . . . Energy distribution curve

EDS . . . . . Energy-dispersive x-ray spectroscopy

FS . . . . . Fermi surface

FSS . . . . . Fermi-arc surface state

f.u. . . . . . Formula unit

GGA . . . . . Generalized gradient approximation

Gr . . . . . Graphene or graphite

hBN . . . . . Hexagonal Boron nitride

HOPG . . . . . Highly oriented pyrolytic graphite

HR . . . . . High resolution

IB . . . . . Intrinsic bilayer

LDOS . . . . . Local density of states

LEED . . . . . Low-energy electron diffraction

LH . . . . . Linear horizontal

LV . . . . . Linear vertical

MATBG . . . Magic angle twisted bilayer graphene

MBE . . . . . Molecular-beam epitaxy

MCP . . . . . Multichannel plate

MDC . . . . . Momentum distribution curve

MR . . . . . Magnetoresistance

PBE . . . . . Perdew-Burke-Ernzerhof

QAH . . . . . Quantum anomalous Hall

rDC . . . . . Replica Dirac cone

SOC . . . . . Spin-orbital coupling

SEM . . . . . Scanning electron microscope

SPEM . . . . . Scanning photoemission microscopy

SS . . . . . Surface state

STM . . . . . Scanning tunnelling microscope

STS . . . . . Scanning tunnelling spectroscopy

tbWSe$_2$ . . . . Twisted bilayer WSe_2

TB . . . . . Twisted bilayer

TE . . . . . Thermoelectric

TMD . . . . . Transition metal dichalcogenide

TSP . . . . . Titanium sublimation pump

VASP . . . . . Vienna ab initio simulation package

VBM . . . . . Valence band maximum

VBT . . . . . Valence band top

XRD . . . . . X-ray diffraction

1

Introduction to angle-resolved photoemission spectroscopy

Contents

Angle-resolved photoemission spectroscopy (ARPES) is a powerful experimental method that can directly visualize the electronic structure of crystalline materials [1–5]. In this chapter, we present a systematic review on the ARPES technique, from the basic principles to the experimental workflow. This chapter includes three sections: the first section provides an insightful interpretation of ARPES spectrum from basic quantum mechanics; the second section presents an overview of ARPES equipment, which covers necessary components for a synchrotron-based ARPES facility; the third section serves as a tutorial for ARPES experiment, in which details about sample preparation and data acquisition are demonstrated.

1.1 Principles of photoemission

1.1.1 General description

A typical ARPES measurement consists of a crystalline sample irradiated by monochromatic light of energy $h\nu$, which gives out photoelectrons emitted in all possible directions [4]. The electron analyser can collect and record the emitted electrons with certain kinetic energies E_k and emission angles (ϕ and θ), where θ is defined as the polar angle with respect to the surface normal, and ϕ is the azimuthal angle related with the in-plane orientation of sample or the experimental geometry [Fig. 1.1]. Using the conservation law of energy and momentum, the binding energy E_B and the crystal momentum $\hbar\mathbf{k}$ of the electron before photoemission can be deduced as:

$$E_B = h\nu - \Phi - E_k \tag{1.1}$$

$$\hbar k_{\parallel} = \sqrt{2mE_k} \cdot \sin(\theta) \tag{1.2}$$

where Φ is the sample surface work function, $\hbar k_{\parallel}$ is the parallel (defined with respect to the sample surface) component of crystal momentum and m is the electron mass. We should notice that the detected kinetic energy of a photoelectron in an electron analyser E_k^A may be different from the real kinetic energy E_k, as the work function of sample surface Φ may not equal to the work function of analyser Φ_A, detailed

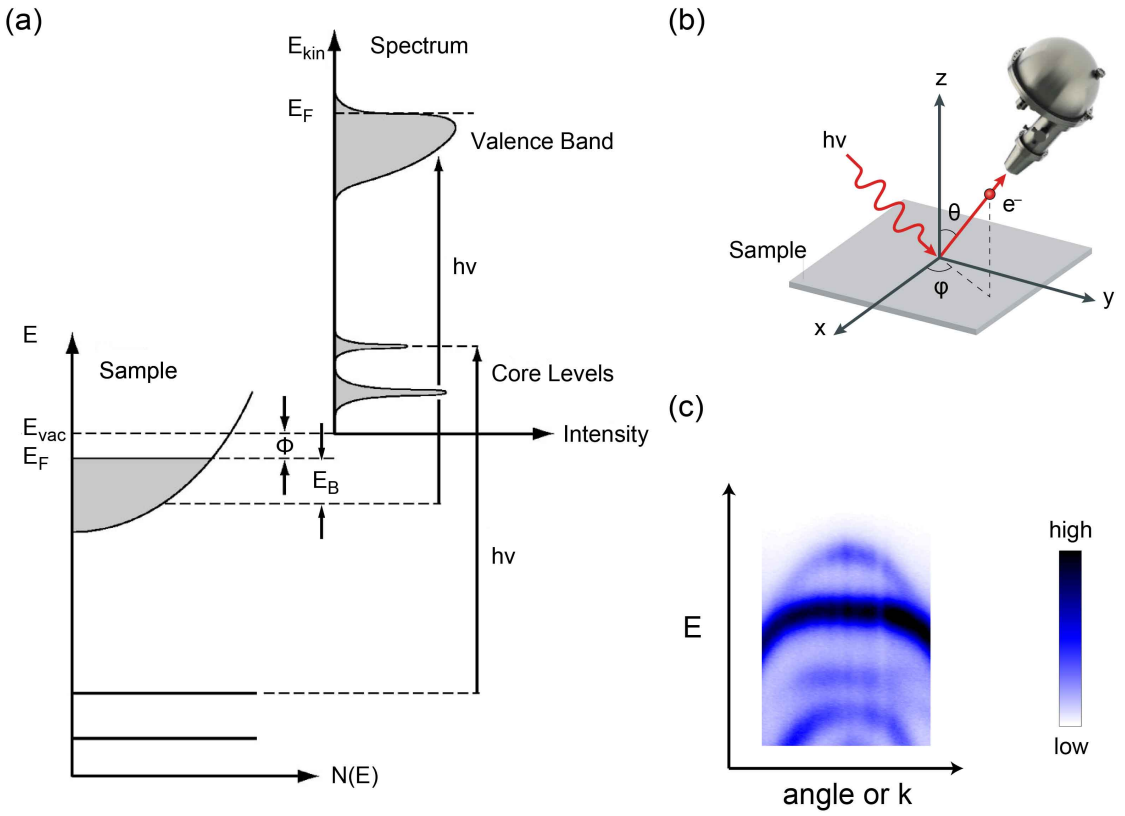

Figure 1.1: Basic concepts of ARPES. (a) Energetics of the photoemission process. An electron is excited from an initial state with binding energy E_B (or at corelevel) below E_F to a final state above the vacuum energy E_{vac}. After transmission through the surface barrier, the photoelectron has kinetic energy $E_{kin} = h\nu$-E_B-Φ, where Φ is the sample work function. (b) Schematic illustration of ARPES measurement. An electron is excited by a photon with energy $h\nu$, emitted to the direction (ϕ, θ), and then collected by the electron analyser. (c) Typical energy-momentum dispersion obtained from ARPES measurements. This data shows the Γ-valley bands of bilayer WSe_2. (a) is adapted from [1]. (b) is adapted from [2].

discussion of which is available in Ref. [6]. (Here, we have neglected the momentum of incident photon as it is negligible compared with that of emitted electron in the ultraviolet range (<150 eV), though it cannot be neglected in the higher energy range [7].) As the in-plane periodicity of the crystal structure is a subset of that of the vacuum, the eigenvalue of in-plane momentum of the photoelectron remains valid after emission, so that $k_{\parallel}$ is conserved through the photoemission process. On the contrary, the orthogonal component $k_{\perp}$ is not conserved due to the discontinuity between the surface and the vacuum. Empirically, $k_{\perp}$ can be estimated with the

assumption of a free-electron final-state:

$$\hbar k_{\perp} = \sqrt{2m(E_k \cos^2(\theta) + V_0)} \tag{1.3}$$

where V_0 is the inner potential, which is in principle the expectation value of pseudo-potential experienced by the electron on Fermi surface [8]. However, in practice, we usually treat the inner potential as an empirical parameter (usually 5-20 eV) based on the periodicity in $h\nu$-dependent data.

1.1.2 Interpretation of ARPES spectrum

A typical ARPES spectrum presents the energy-momentum dispersion weighted by photoemission intensity [Fig. 1.1(c)], which reflects the electronic structure of crystalline materials. The interpretation of dispersion and photoemission intensity can be deduced from the transition probability w_{ij} for an optical excitation between an N-electron ground state $\left|\Phi_i^N\right\rangle$ to one of the available final states $\left|\Phi_f^N\right\rangle$ [4]. Assuming the interaction between the incident light and the sample to be weak, we can use Fermi's Golden rule for the first order approximation:

$$w_{fi} = \frac{2\pi}{\hbar}\left|\left\langle\Phi_f^N\middle|H_{int}\middle|\Phi_i^N\right\rangle\right|^2 \delta(E_f^N - E_i^N - h\nu) \tag{1.4}$$

where E_f^N and E_i^N are the final and initial state energies, respectively, and H_{int} is the Hamiltonian that includes all interaction. When only the electron-photon interaction is considered, H_{int} can be expressed:

$$\begin{aligned} H_{int} &= \frac{1}{2m}(\mathbf{p} + \frac{e}{c}\mathbf{A})^2 - \frac{\mathbf{p}^2}{2m} - e\boldsymbol{\phi} \\ &\approx \frac{e}{2mc}(\mathbf{A}\cdot\mathbf{p} + \mathbf{p}\cdot\mathbf{A}) \\ &\approx \frac{e}{mc}\mathbf{A}\cdot\mathbf{p} \end{aligned} \tag{1.5}$$

where $\mathbf{p}$ is the electron momentum operator, and $\mathbf{A}$ and $\boldsymbol{\phi}$ are the electromagnetic vector and scalar potentials, respectively. In the first step approximation,we enforce the Weyl gauge in which the scalar potential $\boldsymbol{\phi} = 0$, and disregard the quadratic terms of vector potential $\mathbf{A}$. The second approximation step uses the dipole approximation in which $[\mathbf{A}, \mathbf{p}] \sim 0$.

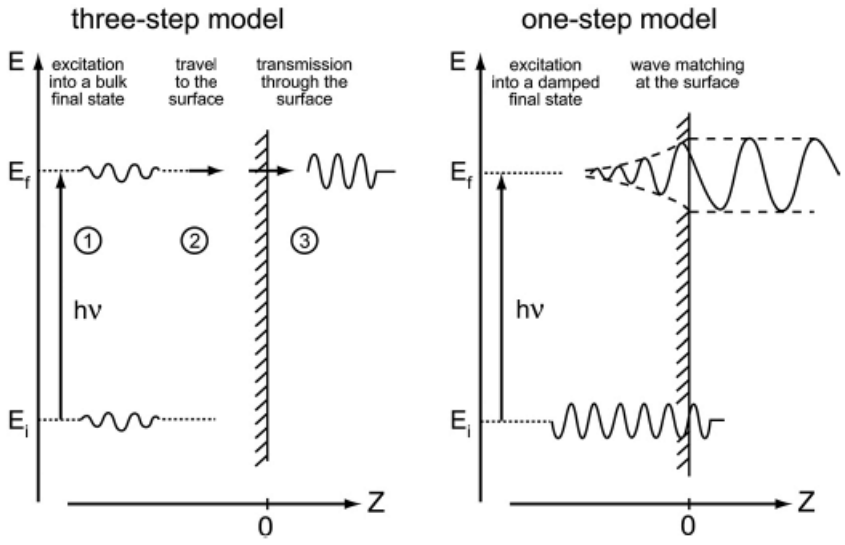

Figure 1.2: Three-step and one-step models. This figure is adapted from [1].

Equation 1.4 corresponds to the *one-step model*, which treats photoemission as a single coherent process [1]. This expression is straightforward in formularization, while inexplicable in physics picture, as all the procedures, from photon absorption to electron detection, are entangled in the interaction term. It is more convenient to use the *three-step model* [Fig. 1.2], which divides the photoemission process into three steps phenomenologically : (1) The excitation of photoelectron in the sample bulk; (2) The propagation of photoelectron to the sample surface; (3) The escape of photoelectron to the vacuum. The three-step model has the advantage of decoupling the photoemission into tractable procedures. Step (1) contains the information of the intrinsic electronic structure, which can be directly calculated under suitable approximation. Step (2) considers the scattering process during the photoelectron's traveling to the surface. This complex scattering process is often generally described by the inelastic mean free paths for electrons in solids λ_{MFP}, which indicates only a fraction of photoelectrons can take the intrinsic information and emphasizes the surface-sensitivity of ARPES techniques. Step (3) considers the energy barrier between the solid and vacuum, which blocks the photoelectron with low energy and modifies the energy and momentum of emitted electrons.

According to the three-step model, one can develop intuition for the intrinsic electronic structure by formularizing step (1). We start with the simple case of non-

interacting system. Using the sudden approximation, the N initial and final states can be factorized into 1 photoelectron state and N-1 background electron states:

$$\left|\Phi_i^N\right\rangle = \mathcal{A}\left|\phi_i^{\mathbf{k}}\right\rangle \otimes \left|\Phi_i^{N-1}\right\rangle \tag{1.6}$$

$$\left|\Phi_f^N\right\rangle = \mathcal{A}\left|\phi_f^{\mathbf{k}}\right\rangle \otimes \left|\Phi_f^{N-1}\right\rangle \tag{1.7}$$

where $\mathcal{A}$ is the antisymmetric operator enforcing Pauli principle, $\left|\phi_i^{\mathbf{k}}\right\rangle$ and $\left|\phi_f^{\mathbf{k}}\right\rangle$ are the wave functions of the photoelectron before and after interacting with the incident photon, $\mathbf{k}$ is the same wave vector due to momentum conservation. In the non-interacting limit, where the background electrons remain unchanged and can be decoupled from the photoelectron, equation 1.4 can be written as:

$$\begin{aligned} w_{fi}(\mathbf{k}, E_{\mathbf{k}}) &\propto \left|\left\langle \phi_f^{\mathbf{k}}\middle|\mathbf{A}\cdot\mathbf{p}\middle|\phi_i^{\mathbf{k}}\right\rangle\right|^2 \left|\left\langle \Phi_f^{N-1}\middle|\Phi_i^{N-1}\right\rangle\right|^2 \delta(E_f - E_{\mathbf{k}} - h\nu) \\ &= \left|M_{f,i}(\mathbf{k})\right|^2 \delta(E_f - E_i - h\nu) \end{aligned} \tag{1.8}$$

where E_f and $E_{\mathbf{k}}$ are the energies of initial and final state of the photoelectron. $M_{f,i}(\mathbf{k}) = \left\langle \phi_f^{\mathbf{k}}\middle|\mathbf{A}\cdot\mathbf{p}\middle|\phi_i^{\mathbf{k}}\right\rangle$ is the one-electron dipole matrix element, or matrix element for short. Equation 1.8 demonstrates that, in the non-interacting limit, ARPES spectrum directly renders the energy-momentum dispersion of the electron in solid and the photoemission intensity is determined by the matrix element.

In general case, where the many-body effect cannot be ignored, the final state of the background electrons can be left in a random number of excited states with eigenfunctions $\left|\Phi_m^{N-1}\right\rangle$ and energies E_m^{N-1}. Thus, equation 1.4 should be written as:

$$I_{fi} \propto \sum_{f,i} \left|M_{f,i}(\mathbf{k})\right|^2 \sum_m \left|\left\langle \Phi_m^{N-1}\middle|\Phi_i^{N-1}\right\rangle\right|^2 \delta(E_f + E_m^{N-1} - E_i^N - h\nu) \tag{1.9}$$

For strongly correlated systems, Φ_i^{N-1} will overlap with many eigenstates, deviating from the non-interacting picture by presenting satellite peaks or broadening spectra peaks in ARPES spectrum.

In the above-mentioned formulization, we approximate the removal of the electron as an instantaneous process (the sudden approximation), which can be applied to most of ARPES measurements. However, in some cases, the sudden creation of a hole can be associated with bosonic excitations such as phonons, plasmons, and

electron-hole pairs that lead to satellite peaks on the low-energy side of the main photoemission peak, detailed discussion of which can be found in Refs. [9–11].

Equation 1.9 can also be written in the Green's function formalism, in which we use the single-electron removal spectral function $A^-(\mathbf{k}, w)$:

$$A^-(\mathbf{k}, w) = \sum_m \left| \left\langle \Phi_m^{N-1} \middle| c_\mathbf{k} \middle| \Phi_i^N \right\rangle \right|^2 \delta(w - E_m^{N-1} + E_i^N) \tag{1.10}$$

where $c_\mathbf{k}$ is the annihilation operator. $A^-(\mathbf{k}, w)$ is related to the full spectral function by $A-(\mathbf{k}, w) = A(\mathbf{k}, w)f(w)$, where $f(w)$ is the Fermi-Dirac distribution. Thus, equation 1.9 can be written as:

$$I(\mathbf{k}, w) = I_0(\mathbf{k}, h\nu, \mathbf{A})f(w)A(\mathbf{k}, w) \tag{1.11}$$

This formula clearly demonstrates the physical meaning of ARPES spectrum: under the sudden approximation, the photoemission signal is proportional to the single-particle spectral function $A(\mathbf{k}, w)$, whose intensity is modified by the Fermi-Dirac distribution $f(w)$ and matrix-element-related pre-factor $I_0(\mathbf{k}, h\nu, \mathbf{A})$. This result also points out that ARPES is limited in detecting the occupied states below the Fermi level and its results are dependent on the experimental conditions, such as the polarization of incident light and measurement geometry. In this thesis, we mainly focus on the single-particle spectral function $A(\mathbf{k}, w)$ to understand the electronic structure of crystalline materials. Some qualitative analysis of the pre-factor $I_0(\mathbf{k}, h\nu, \mathbf{A})$ based on the selection rule is performed to reveal the orbital characters of electronic structure [12].

1.2 ARPES equipment

1.2.1 Light source

The light source is the core factor that determines the capabilities of an ARPES experimental setup. A summary of the key parameters of commonly used light sources is presented in table 1.1 [13].

The photon energy $h\nu$ directly determines the range and resolution of the measured crystal momentum. Light sources with low $h\nu$ are employed to exploring

Light Sources	Photon Energy	Polarisation	Photon flux	Spot size
Synchrotron	5 eV-1000 eV	Variable	10^{12}/s	0.1 mm/500 nm
Laser	6,7,11 eV	Variable	10^{15}/s	0.1 mm
Gas-discharge lamp	21.2 eV (He)	Non-polarized	10^{12}/s	1 mm

Table 1.1: Summary of light sources.

the fine structure around the Brillouin zone (BZ) center due to the high resolution. Light sources with higher $h\nu$ enable the detection of electronic structure in a larger momentum space, which is essential for the study of materials with interesting band structure near the BZ boundary, such as Dirac cones in graphene. For materials with 3D crystal structure, ARPES results at a given $h\nu$ only correspond to the electronic structure of a 2D surface in the 3D Brillouin Zone, and thus a systematic ARPES measurement requires the light source with tunable photon energies. Besides, $h\nu$ directly determines the kinetic energy E_k of the emitted electron, which is related with the mean free path λ_{MFP} via the *Universal Curve* [Fig. 1.3]. According to the universal curve [5], light sources with high photon energy (>100 eV) enables the detection of bulk states while those with middle and low photon energy (20-100 eV) are favorable for surface state measurements. Laser ARPES (<10 eV) is also favorable for the measurement of bulk states due to the large mean free path.

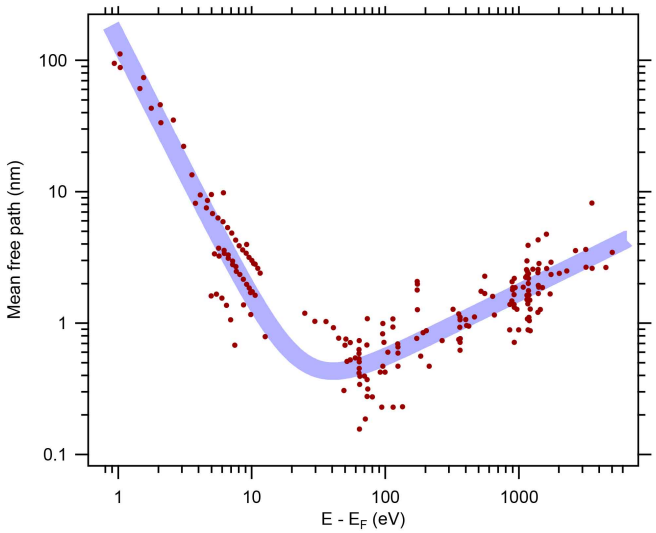

Figure 1.3: Universal curve. The relationship between mean free paths in solids and the kinetic energies of emitted electrons. This figure is adapted from [5].

The polarization of incident photon influences the photoemission intensity via the matrix element [12]. At specific measurement geometry, ARPES with linearly polarized beam can detect electrons with certain wave function due to the requirement of parity, which in principle enables the orbital-selective measurement. ARPES with circularly polarized beam is proposed to realize spin- and geometry-phase-related detection, though results from which need to be carefully interpreted.

The beam spot size sets a restriction on size of samples. To guarantee the reliability of the ARPES data, the diameter of beam spot should be at most half of the sample size. To study delicate structure such as magnetic-domain-induced modification, the beam spot should be comparable to the domain size.

The photon flux determines the efficiency of ARPES measurement, as it significantly influences the rate of electron excitation. Generally, the larger photon flux can lead to better data quality in the same measurement time due to the high statistics. However, for material systems with poor conductivity, large photon flux will lead the charging effect (instability of the work function), as the rate of electron emission is larger than that of refilling from the ground. In some cases, the large photon flux can even destroy the sample surface, as it can lead to over-heating or light-induced chemical reaction on the sample surface.

ARPES results presented in this thesis were obtained from synchrotron-based ARPES facilities, which provide tunable photo energy and polarization, large photon flux and tiny spot size to investigate various kinds of materials. The regular ARPES results were mainly obtained from the high-resolution (HR) branch of Beamline I05 in Diamond Light Source. The nano-ARPES results were obtained form Beamline Spectromicroscopy in Elettra Sincrotrone Trieste, Beamline ANTARES in Synchrotron SOLEIL, and the nano-branch of Beamline I05 in Diamond Light Source.

1.2.2 Optics

Here, we use Beamline I05 of Diamond Light Source as an example to introduce the layout of synchrotron-based ARPES optics [Fig. 1.4] [14]. The polarized and monochromatic beam is first generated in the undulator and then admitted into

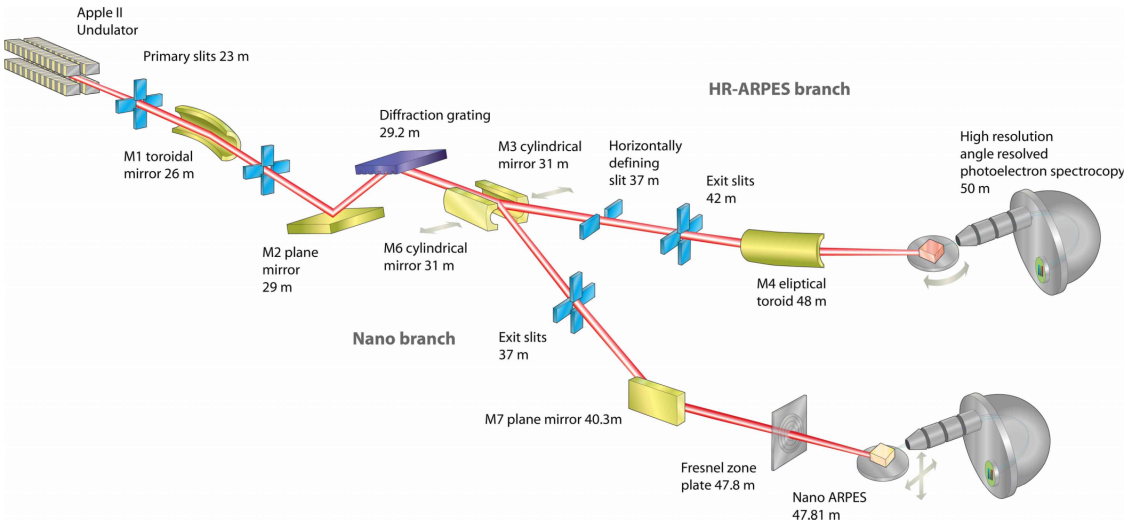

Figure 1.4: Layout of ARPES beamline. Schematic layout of the optics at beamline I05 of Diamond Light Source. This figure is adapted from [14].

the optics system through primary slits that control the illumination. The first toroidal mirror M1 functions as collimation. A set of slits just after M1 block the unaligned radiation from the edges of M1. The beam then passes the plane mirror and the grating monochromator for better energy resolution. Beamline I05 has two endstations, namely the HR branch and the nano-branch, with different optical design after the grating. For the HR branch, the beam is refocused via a cylindrical mirror M3 and a elliptical toroid to reach a spot size with diameter around 50 μm. For the nano-branch, the beam is pre-focused via the cylindrical mirror M6 and then fine-focused via Fresnel zone plate to reach a sub-micron beam spot, the minimum diameter of which can reach 200 nm in principle.

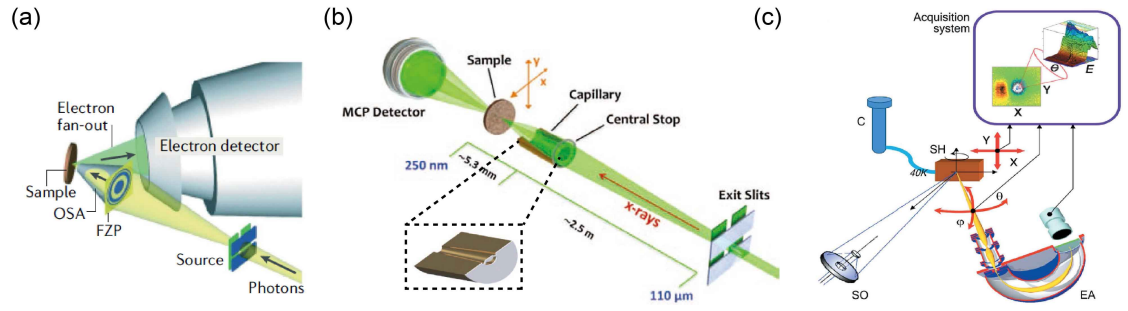

Figure 1.5: Nano-ARPES focusing optics. (a) Zone plate optics, adapted from [3]. (b) Capillary mirror optics, adapted from [15]. (c) Schwarzschild objectives optics, adapted from [16].

In addition to Fresnel zone plate [3], capillary mirrors (recently equipped in I05) [15] and Schwarzchild objectives (equipped in Spectromicroscopy) [16] can also be utilized to realize tiny beam spot [Fig. 1.5], though each of them shows some limitation. Fresnel zone plate blocks most of the incident beam and significantly suppresses the photon flux through it, which limits the efficiency of nano-ARPES measurement. Besides, the focus of Fresnel zone plate is energy-dependent, which requires delicate calibration while changing the photon energy. Capillary mirror is now a popular alternative choice to Fresnel zone plate, as it can guarantee a high beam intensity while keeping the beam size with a diameter of around 10 μm. However, capillary mirror may not be ideal for the study on fabricated devices, in which μm-sized inhomogeneity commonly exists. The average effect from large beam spot may blur the delicate structure, such as the moiré bands in twisted systems. Schwarzchild objectives are another choice for the nano-meter-size focusing, which can keep both high intensity and tiny beam spot, though special coating materials are required for good reflectivity at given photon energy.

1.2.3 Vacuum system

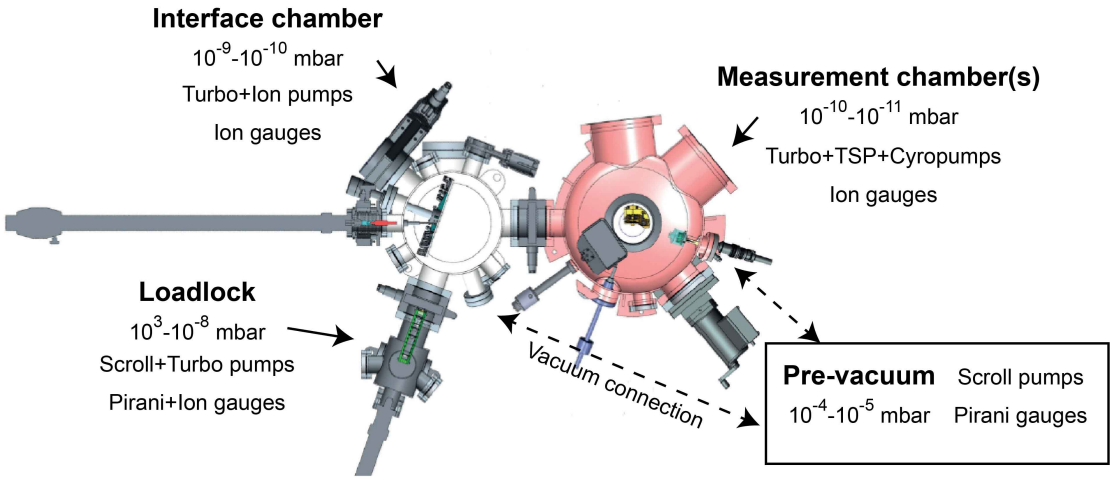

Figure 1.6: Vacuum system. Schematic layout of the vacuum system of a typical ARPES system, adapted from [14].

ARPES measurement requires a good vacuum condition for two main reasons [17]. First, for the emitted photoelectron to be able to freely travel from the sample

surface to the electron detector, a large mean free path out of the sample λ_v is required. As the typical distance between the sample surface and the detector is around 2 m, λ_v should better be larger than 10 m. According to the kinetic theory, λ_v is inversely proportional to the pressure; λ_v ~10 m roughly correspond to a vacuum around 10^{-5} mbar (10^{-3} Pa). Second, the absorption of gas atoms on the sample surface can 'kill' the intrinsic information of photoelectron by scattering, and sometimes the air-sensitive sample can even interact with the residual oxygen and water molecules. Calculation based on the Maxwell-Boltzmann distribution demonstrates that forming a single layer oxygen molecules on the sample surfaces at a temperature of 10 K and a vacuum of 10^{-9} mbar only takes 1 hour [17]. Thus, for a typical ARPES measurement that takes more than 24 hours, an ultra-high vacuum better than 10^{-10} mbar is required.

Figure 1.6 presents the schematic layout of a typical ARPES vacuum system [14], which mainly consists of three kinds of chambers, namely the loadlock, the interface chamber and the measurement chamber. Each kind of chamber is equipped with different kinds of vacuum pumps and gauges dependent on its function and working vacuum range. Here, we list the commonly used pumps [table 1.3] and gauges [table 1.2] in the ARPES setup [17].

Vacuum gauges	**Mechanism**	**Working condition**
Pirani	Heat Radiation	10^{3}-10^{-4} mbar
Penning	Cold-cathode ionization	10^{-2}-10^{-7} mbar
Hot-ion	Hot-cathode ionization	10^{-3}-10^{-10} mbar
Inverted magnetron	Cold-cathode ionization	10^{-4}-10^{-12} mbar

Table 1.2: Summary of vacuum gauges.

Pumps	**Mechanism**	**Working condition**
Scroll	Mechanical	10^{3}-10^{-5} mbar
Turbo	Mechanical	10^{-1}-10^{-9} mbar
Ion	Ionization/Absorption	10^{-2}-10^{-12} mbar
Titanium sublimation	Absorption	10^{-7}-10^{-12} mbar
Cyro	Condensation/Absorption	10^{-4}-10^{-9} mbar

Table 1.3: Summary of pumps.

The loadlock is a small chamber for transferring samples from the atmosphere into the vacuum system, which requires the pumps and gauges to cover a large vacuum range (from the atmosphere and the high vacuum). This can be realized by the combined usage of scroll and turbo pumps, Pirani and ion (Penning, hot-ion or inverted magnetron) gauges. The interface chamber is usually designed to store samples at a high vacuum environment, and sometimes it provides space for surface cleaning (e.g., sputtering and annealing). Thus, turbo and ion pumps are needed for reaching a vacuum better than 10^{-10} mbar and ion gauges are required for monitoring the vacuum. The measurement chamber is where data acquisition is performed (in some cases, there are multiple measurement chambers enabling other characterizations, such as LEED) and has the strictest requirement of vacuum (around 10^{-11} mbar), which can be realized by the combination of turbo, titanium sublimation (TSP) or cryo pumps. To avoid the overload and damage of main pumps (ion, TSP, cyro), a pre-vacuum system based on scroll pumps is designed to provide a base vacuum around 10^{-5} mbar.

1.2.4 Manipulator

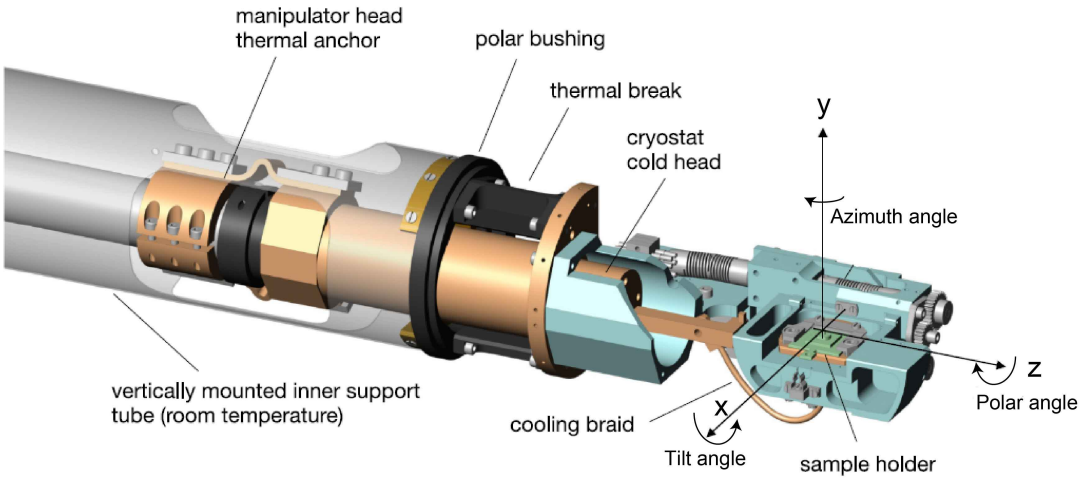

Figure 1.7: Manipulator. Rendering of a typical manipulator head, adapted from [14].

A manipulator is a composite of the sample stage, associated motion and temperature control parts [Fig. 1.7] [14]. A modern manipulator is usually equipped

with a 6-axis-freedom sample stage controlled by step or servo motors. The basic translation control (x, y, z) enables the sample positioning and defocusing. The rotation control, usually named the polar (the rotation axis is along the manipulator direction), the azimuth (the rotation axis is normal to the sample stage), and the tilt (the rotation axis is normal to the other two) control, is used for the data acquisition in a 3D space (usually k_x-k_y-E_B) or the alignment of sample orientation.

Most ARPES studies focus on examining the elementary excitation of an electronic system, which requires temperatures lower or comparable to the interesting temperature scale [17]. To obtain a low temperature environment, a helium-based cooling system through the manipulator is required. In the presented design [Fig. 1.7], the sample receptacle is cooled with a copper braid assembly and thermally insulated from the supporting mechanical system by a thin-walled polyimide cylinder. A secondary cylindrical cold-shield surrounding the entire manipulator head is installed in the measurement chamber. This shield is cooled by an independent closed cycle cryostat and reaches a base temperature. Samples can be heated up for the study of phase transition by using a heater near the cold-head of the cryostat.

1.2.5 Analyser

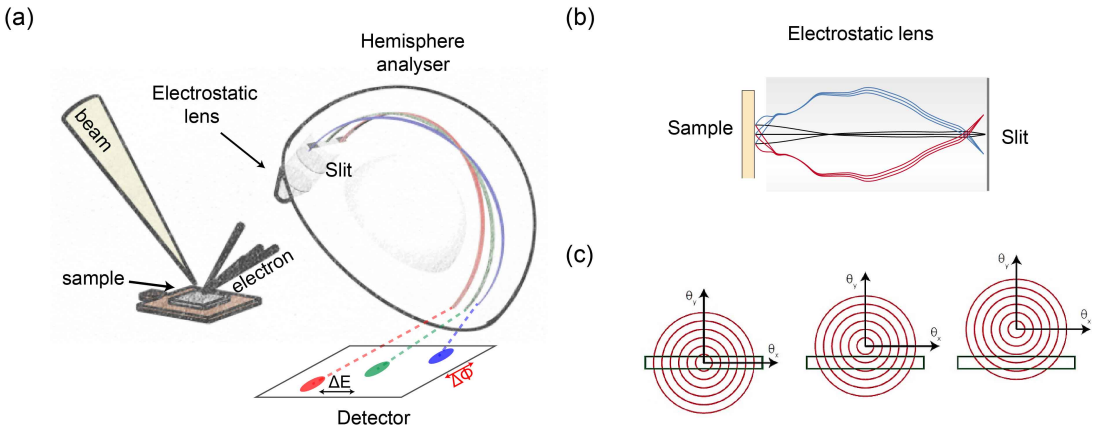

Figure 1.8: Photoelectron analyser. (a) Schematic illustration of the hemisphere analyser. (b) Illustration of the electrostatic lens. (c) Illustration of DA30 Mode. During the DA30 scanning, sample and analyser remain unmoved while a deflection voltage is applied to collect emitted electrons in different angle sets (θ_x, θ_y). (b) is adapted from [4]. (c) is adapted from [18].

A photoelectron analyser uses electrostatic elements to manipulate the trajectory and energy of electrons and impinge them onto a detector [4]. The most commonly used analyser is the hemispherical analyser as shown in Fig. 1.8. It consists of an electrostatic lens, followed by a hemispherical deflector and finally a multichannel plate (MCP) detector. The electrostatic lens aligns the electrons based on their emitted angles and project them onto the entrance slit of the hemispherical deflector. The deflector consists of two concentric hemispherical electrodes with different electrostatic potentials, leading to a radial electric field that distinguishes electrons with different energies into different elliptical orbits. After passing the exit slit, electrons with different kinetic energies and emitted angles will be impinged onto the MCP detector, which records the 2D photocurrent distribution. In most cases, there will be a phosphor screen after the MCP, from which the resulting luminescence can be read into a computer using a CCD camera for real-time imaging. For mapping the angular distribution orthogonal to the entrance slit (3D scanning in k_x-k_y-E_B space), conventionally the sample stage is rotated with respect to an axis parallel to the entrance slit. Recent developments on analyser incorporate angular deflection electrodes within the electrostatic lens, which enables the collection of photoelectron with orthogonal emitted angles without any mechanical rotation.

1.3 Experiment methods

1.3.1 Sample preparation

ARPES is a surface-sensitive technique because of the limited mean free path of the photonelectron. In this subsection, we will present how to create a clean and flat surface for ARPES measurements, in order to avoid the scattering by the disorder on sample surface.

For single crystal samples, the conventional preparation method follows a glue-cleave procedure as shown in Fig. 1.9. The sample is first mounted onto the sample holder by the conductive glue (epoxy) to ensure the electron refilling from the ground. Then a cleaving bar, usually a ceramic post, with the same kind of glue at the bottom end, will be put onto the top surface of the sample. Then

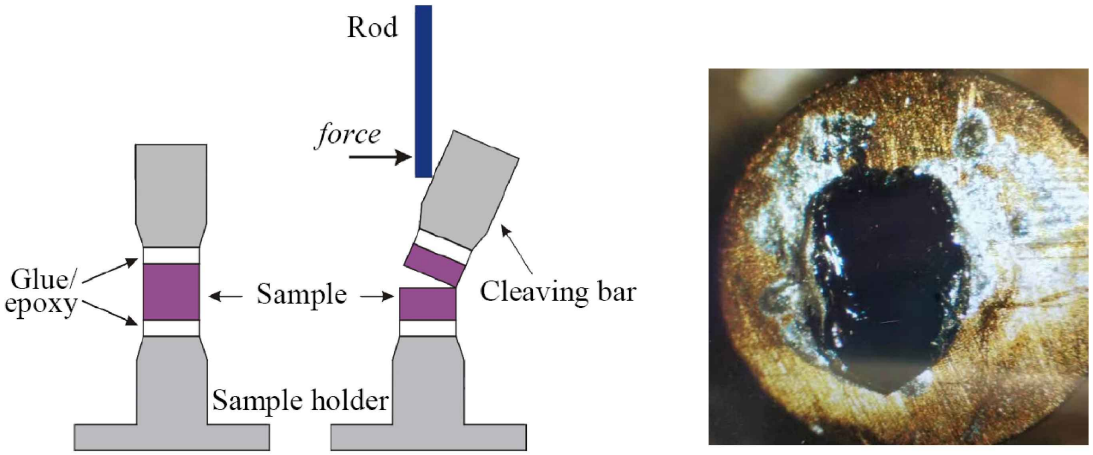

Figure 1.9: Glue-cleave method. Left panel: illustration of the glue-cleave procedure. Right panel: the cleavage suface of BiCuSeO single crystal.

the sample will be transferred in to the vacuum system and cleaved before the measurement. The glue-cleave method works well for most of the samples with quasi-2D crystal structure, resulting in the large and flat cleavage surface as shown in the right panel of Fig. 1.9. However, the glue-cleave method shows drawbacks in many aspects. First, the success rate of cleavage on hard samples (materials with 3D crystal structure) is relatively low, which requires large amounts of precious samples for trial and error. Second, though the sample is successfully cleaved, the orientation and termination of the cleavage surface is random even after careful alignment by XRD or Laue. It requires expert skills (or sometimes good luck) to get the wanted surface. Third, the glue-cleave method is a one-time method, which means measurements on the same sample surface are hardly repeatable.

One alternative way for preparing single crystal samples is the sputter-anneal method as shown in Fig. 1.10 [19, 20]. The random-shaped sample is first aligned along the orthogonal direction to the wanted surface and then polished to get a roughly flat surface. Then the sample is mounted onto the Molybdenum or Tantalum sample plate by high-temperature glue (usually carbon paste) or fixed onto the sample plate mechanically. The mounted sample is then transferred into the vacuum for sputtering and annealing cycles. The Ar ion sputtering is aimed to remove the unwanted atoms and the high temperature annealing offers energy

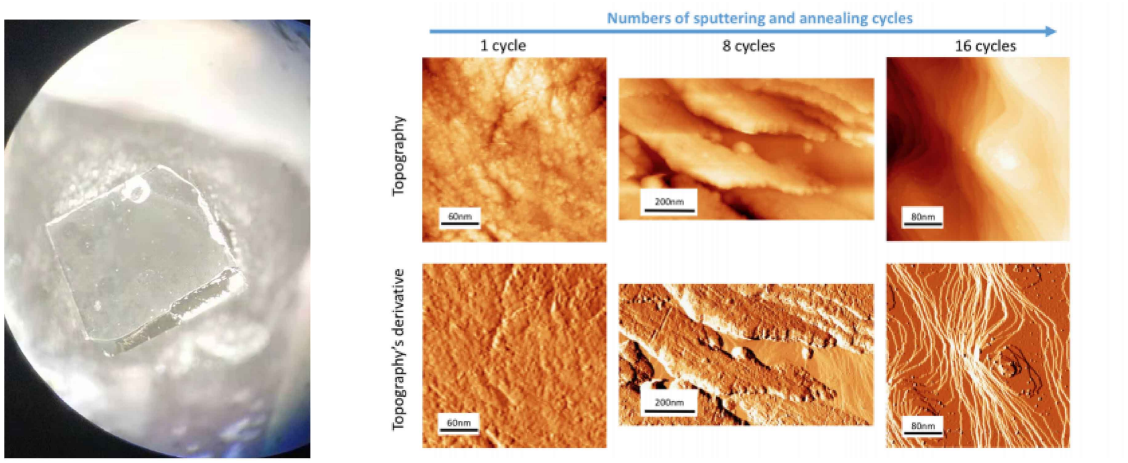

Figure 1.10: Sputter-anneal method. Left panel: the polished PtGa sample. Right panel: sputtering and annealing cycles during the preparation of PtGa samples. After 16 cycles, the surface of PtGa became nearly atomically flat. This right panel is adapted from [19].

for atomic reconstruction on the sample surface. Under the right condition, 10-20 cycles of sputtering-annealing will result in atomically flat surface for ARPES measurement. The limitation for this method is that the sputtering-annealing recipe varies in material systems due to the different thermal properties, which may take months to grope for the ideal condition.

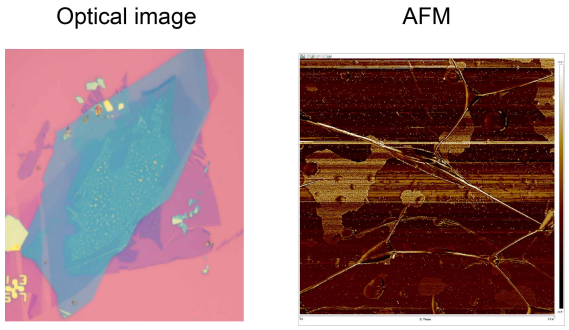

Figure 1.11: Surface of fabricated devices. Optical and AFM images of twisted WSe_2 devices. The red, purple, blue sheets in the optical image are the SiO_2/Si, graphite substrates and the twisted WSe_2 sample, respectively. The yellow sheet (on the top of sample) in the AFM image is the residual glue.

For fabricated devices or other thin film samples, the major task of sample preparation is to remove the residual macromolecular compounds on the surface, which are introduced during the exfoliation and transfer process. The contamination,

appearing as tiny yellow dots in the optical image or pieces of yellow flakes in the atomic force microscopy (AFM) image [Fig. 1.11], can result in strong broadening in ARPES spectrum. Both chemical, such as acetone immersion, and physical approaches, such AFM sweeping and high temperature annealing (beyond the decomposition temperature of the dirty compound), can contribute to a better surface condition. The sample should not be loaded into the vacuum for ARPES measurements until there is a clean and flat area lager than 3*3 μm^2 (given a beam spot size of 1 μm). Once a clean surface is obtained, repeatable measurements on the same position are feasible after annealing at around 200-300 °C for degassing (getting rid of O_2 and H_2O).

1.3.2 Measurement procedures

Though ARPES measurement procedures vary case by case depending on the aim of research project, a routine workflow for synchrotron-based ARPES beamtime can be summarized, which is useful for beginners to start a new project.

The regular ARPES measurement follows procedures as presented in Fig. 1.12. First of all, a flat, clean and homogeneous area on the cleavage surface should be located by adjusting the sample position and optical focus, the criterion for which is related with the intensity as well as the sharpness of the real-time spectrum in the CCD camera. Next, a quick 3D mapping [Fig. 1.12(a)] is performed to determine the in-plane-rotation (azimuth) angle, after which the sample is usually oriented to the high symmetry direction according to the topology of constant energy contour. Then, a series of 3D mappings with different $h\nu$ [figs. 1.12(b)(c)] are performed to determine the normal emission angles (polar and tilt) with respect to the cleavage surface (as illustrated by the red cursors). This angle set corresponds to the first Γ point in the reciprocal space and remains unchanged when $h\nu$ varies. Afterwards, $h\nu$-dependent cuts across the first Γ point will be taken to obtain the band dispersion along k_z [Fig. 1.12(d)], from which we can usually get periodic patterns to determine $h\nu$ corresponding to the high symmetry planes in the BZ (as illustrated by blue lines).

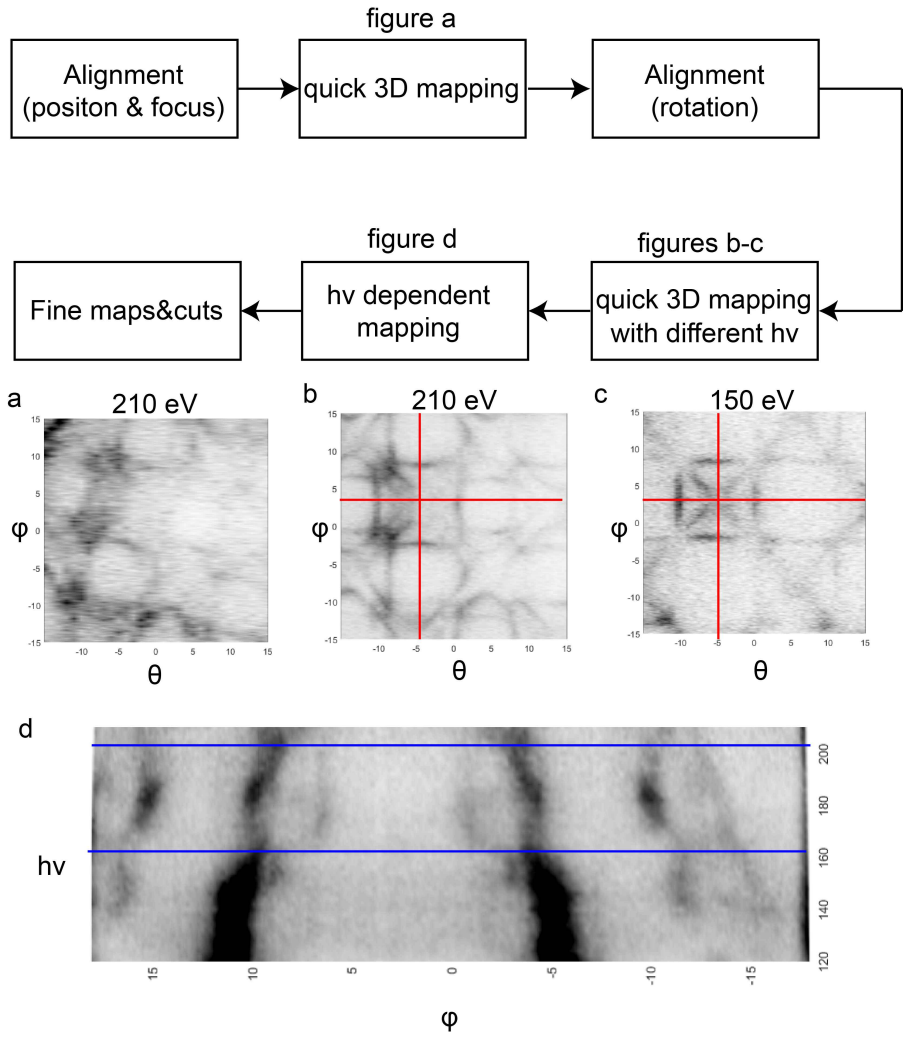

Figure 1.12: Regular ARPES experiment workflow. (a) Quick map at 210 eV before the orientation alignment. (b) Quick map at 210 eV after the orientation alignment. (c) Quick map at 150 eV after the orientation alignment. Red cursors in (b)(c) shows the poistion of the first Γ point (the normal emission angle set). (d) Photo-energy-dependent map to show the k_z periodicity. The blue lines indicate the energies that correspond to the high-symmetry planes.

When all above-mentioned steps are finished, we can start the fine measurement at specific $h\nu$ and angles according to the aim of research project.

Nano-ARPES measurement follows different procedures due to the strict requirements of the beam focus and the sample position [Fig. 1.13]. The sample is first located with the assistance of some external optical elements to get a rough location with an accuracy of 100 μm, followed by a spatial photoemission scanning with a step of 15-20 μm to determine the sample position. Usually, this rough

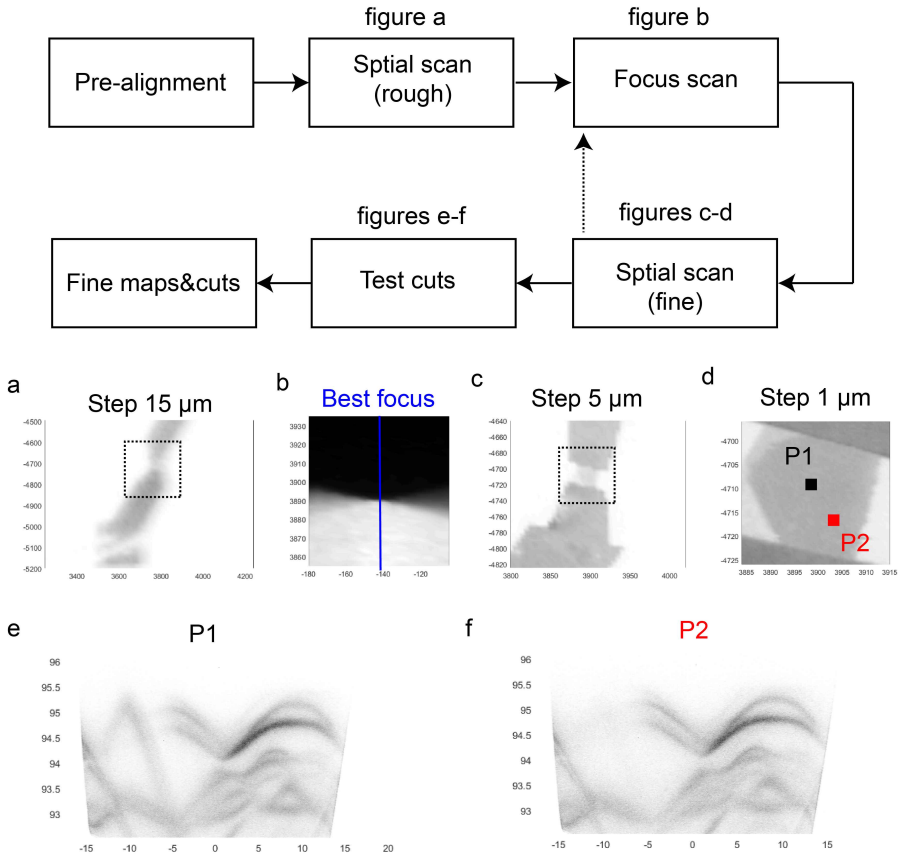

Figure 1.13: Nano-ARPES experiment workflow. (a) Spatial map with a step of 15 μm for sample locating. (b) Focus scan. The blue line indicate the best focus which presents the sharpest sample bondary. (c)(d) Spatial maps with steps of 5 μm and 1 μm, respectively. (e)(f) Energy-momentum disperisons at P1 (black) and P2 (red).

scanning should cover some preset marks (e.g., gold pad), as the beam may not be accurately focused on the sample, which leads to a blurry map [Fig. 1.13(a)] incomparable with the optical image. Next, the sample area with clear edges is chosen for focus scanning, which presents the intensity drop across the edge while changing the defocus positions. Generally, the best defocus position corresponds to the point with sharpest contrast in focus map [Fig. 1.13(b)]. Then, several cycles of spatial and focus scanning are performed until a clear photoemission image of the interesting area is obtained [figs. 1.13(c)(d)]. We notice some subtle defects in the sample may not be distinguished with the spatial resolution of nano-ARPES setup. For example, there is a strong photoemission intensity from graphene substrate at P1 [Fig. 1.13(e)], which indicates there is a crack on the sample surface. Several test cuts (or maps) are necessary before starting the fine

measurement, to avoid wasting the precious beamtime.

2

Overview of twisted 2D materials

Contents

In condensed matter physics, the concept *2D materials* refers crystalline solids consisting of a single layer or few layers of atoms [21, 22]. This concept was first experimentally realized by Novoselov, Geim and other colleagues, who successfully isolated a single layer of carbon atoms (now known as graphene) from graphite using the Scotch tape method [23]. After that, more and more family members of 2D materials (e.g., transition metal dichalcogenides (TMDs) [24], hexagonal Boron nitride (hBN) [25]) have been obtained via repeated mechanical exfoliation [23, 24], chemical vapor deposition (CVD) [26, 27], molecular-beam epitaxy (MBE) [28] and other physical or chemical methods [29, 30].

2D materials are fascinating not only because of their simple crystal structure which can be analogized to paradigmatic quantum models [31], but also because of their exotic properties (e.g., superconductivity [32, 33], charge density wave (CDW) [33, 34], and quantum Hall effects [35]), which present promising potential for industrial application. Moreover, 2D materials can serve as building blocks to artificially assemble materials (2D heterostructures) that are not naturally existent [Fig. 2.1] [21]. The engineering of 2D heterostructure is like playing Lego, which offers considerable freedoms, such as building blocks, stacking order, twist angle, number of layers, to search for intriguing quantum physics in a modular way [21].

Very recently, the interlayer twist angle has turned out to be a crucial parameter for tuning the electronic properties of 2D heterostructures [36]. The twist angle not only affects the interlayer coupling, but can a;so introduce a new periodicity known as the moiré superlattice. Twisted 2D materials with moiré superlattice can host exotic properties, such as correlated insulating states [37, 38], unconventional superconductivity [38–40], and quantized anomalous Hall effect [41]. These exotic phenomena are associated with the emergent low-energy flat moiré band [39]. In this chapter, we will review the electronic properties of the most popular building blocks for 2D heterostructures, namely graphene and TMDs, and introduce the moiré physics in twisted 2D materials.

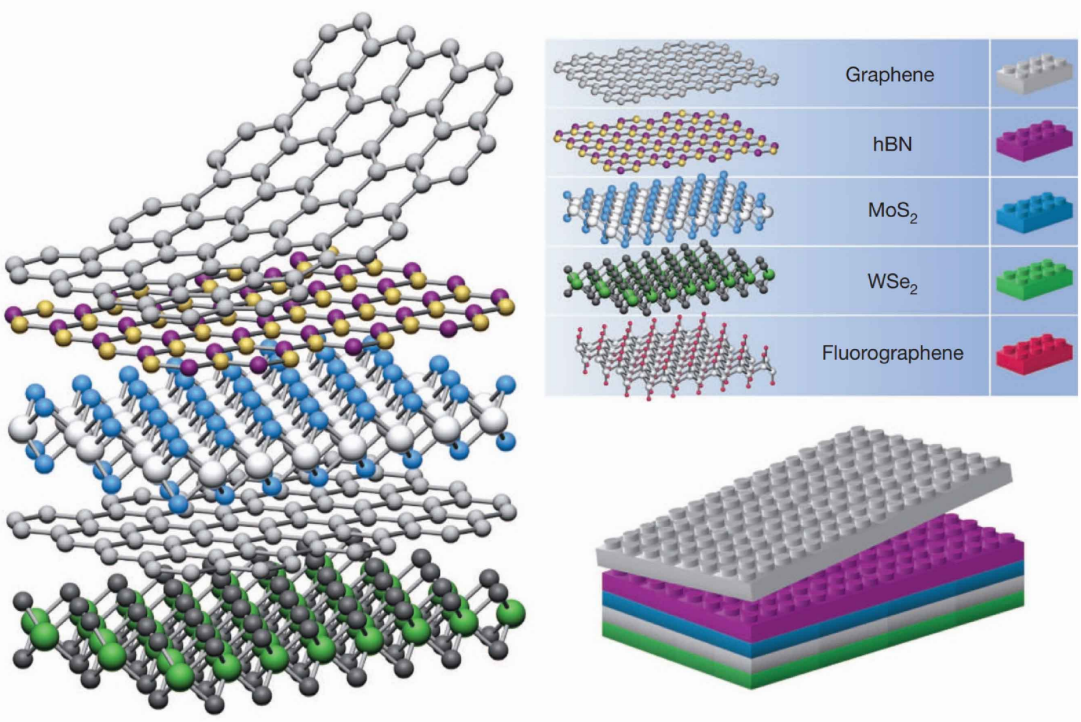

Figure 2.1: 2D heterostructures. This figure is adapted from [21].

2.1 2D materials

2.1.1 Graphene

Graphene is a single layer of carbon atoms arranged on a honeycomb structure made of hexagons [Fig. 2.2(a)], which can be viewed as benzene rings without hydrogen atoms [22, 42]. Each graphene lattice has two non-equivalent carbon atoms (A and B). The distance between neighbouring A and B carbon atoms is $\sim$1.42 Å, and the lattice constant $a \approx 2.46$ Å (the distance between the closest A-A or B-B carbon atoms). The structural stability of graphene is due to the sp^2 hybridization between one s orbital and two p orbitals (p_x and p_y, x and y refer to the in-plane direction), which leads to the formation of σ bond between A-B carbon atoms. Meanwhile, the p_z orbital (perpendicular to the x-y plane) can bind covalently among neighbouring carbon atoms, leading to the formation of a big π band and strengthening the planar structure.

The Brillouin zone (BZ) of graphene is a hexagon [Fig. 2.2(b)]. Conventionally,

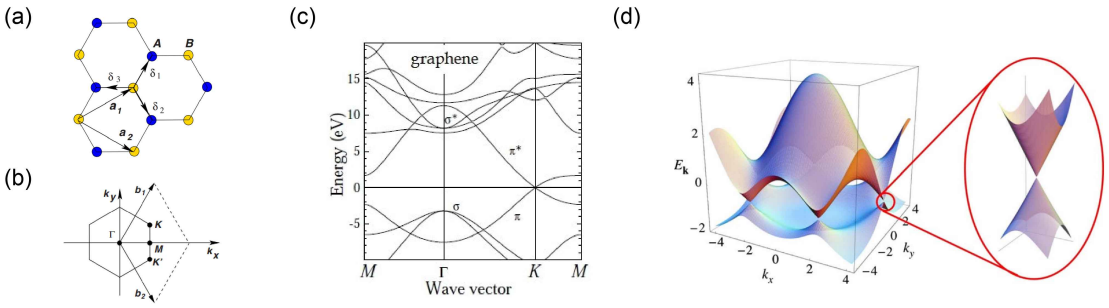

Figure 2.2: Crystal structure and electronic structure of graphene. (a) Crystal structure of graphene. Blue and yellow sites stand form the two non-equivalent carbon atoms (A,B). a_1 and a_2 are the lattice vectors. (b) Brillouin zone of graphene labelled with high symmetry points. b_1 and b_2 are the reciprocal vectors. (c) Electronic structure of graphene. The anti-bonding and bonding states of σ bands and π bands are labelled. (d) Illustration of the electronic struature of graphene in the 3D (k_x-k_y-E_k) space. The zoom-in view presents the Dirac cone at K valley. (a)(b)(d) are adapted from [42]. (b) is adapted from [43].

the neighbouring corners of the BZ are defined separately as the K and K' points due to the non-equivalence of A and B carbon atoms, and the middle point between neighbouring K and K' points is defined as the M point. As long as A and B carbon atoms are in the same chemical and physical environment, the electronic states at the K and K' points are energetically identical [42], and in this thesis, we will not distinguish the K and K' points.

The calculated electronic structure of graphene is presented in Fig. 2.2(c) [43]. The bonding and anti-bonding states of σ bonds (σ and σ^* bands) are located far away from the Fermi level (E_F), which can barely contribute to the electrical transport properties. In sharp contrast, the bonding and anti-bonding states of π bonds (π and π^* bands) form linear dispersions crossing at the K point, and the binding energy of the crossing point is exactly the E_F (in the free-standing graphene). This gapless band structure endows graphene with a semimetal nature. The double-cone-shaped shape structure formed by the π and π^* bands is clearly presented in the 3D illustration (in the k_x-k_y-E space) [Fig. 2.2(d)]. As electronic states at the crossing point can be effectively described by the massless Dirac equation, the bands structure around the K point is usually called the Dirac cone [44].

Graphene serves as an ideal building block to fabricate 2D heterostructures not only because the easy availability, but also due to the p_z dominant low-energy

electronic structure. When graphene layers are stacking with different orders or different twist angles, the change of interlayer overlapping of p_z orbitals can instantly reflect on the electroinc structure and then modify the electrical properties accordingly, which have been confirmed by various transport measurements on twisted graphene.

2.1.2 Transition metal dichalcogenides

Transition metal dichalcogenides are a group of layered materials with the same chemical formula, MX_2, where M is a transition metal element (such as W or Mo) and X is a chalcogen element (such as S, Se or Te) [45]. In contrast to the single phase of graphene, TMDs can exist in multiple structural phases as the unit layer of TMDs consists of three layers atoms (X-M-X) with different arrangements. The two common structural phases are characterized by either trigonal prismatic (2H) or octahedral (1T) coordination of metal atoms [Fig. 2.3]. The 2H phase corresponds to an ABA stacking of X-M-X layers, where chalcogen atoms in different atomic planes occupy the same position and are located on the top of each layer. The 1T phase is featured by an ABC stacking of X-M-X layers, where the chalcogen atoms in the A layer are in the center of the hexagon formed by atoms in the B and C layers. Depending on the particular combination of transition metal (group IV, V, VI, VII, IX or X) and chalcogen elements, the thermodynamically stable phase of TMDs can be either the 2H or 1T phase. In this thesis, we will focus on the group VI TMDs, such as WSe_2 and MoS_2, the stable phase of which is the 2H (except for WTe_2, whose stable phase is 1T') [45]. All TMDs discussed in the following content are in the 2H phase, if not specified.

The definition and notation of TMDs' BZ are the same as those in graphene [Fig. 2.2(b)]. K and K' points are also non-equivalent in TMDs due to the lack of inversion symmetry, which cause strong spin-orbital coupling (SOC) splitting at the K and K' valleys. The spin characters at the K and K' valleys are oppsite [46]. However, as our current experimental results are not spin-resolved, we will not distinguish the K and K' valleys in this thesis.

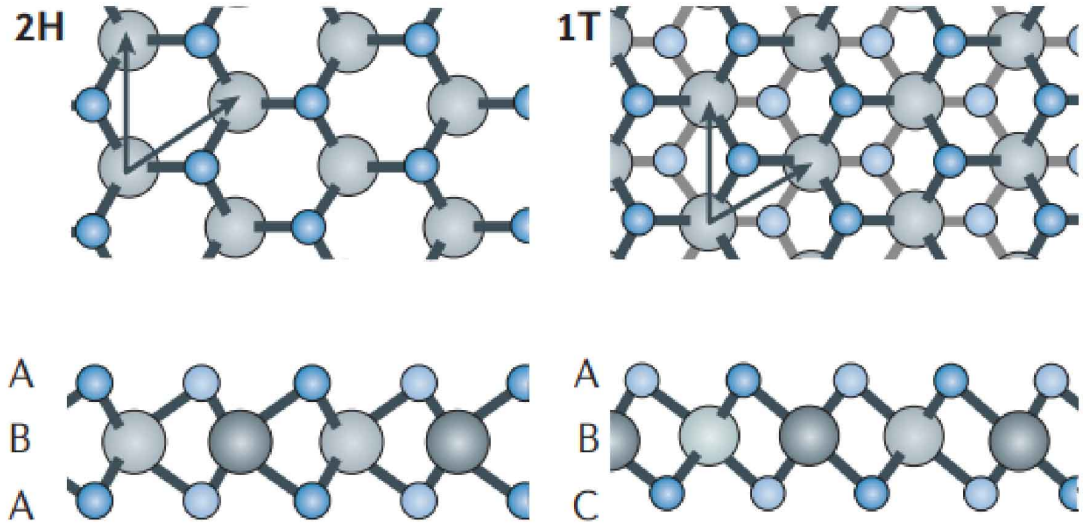

Figure 2.3: Crystal structures of TMDs. Left: 2H-phase. Right: 1T-phase. The top and bottom panels show the top-view and the side-view of TMD crystal structures, respectively. This figure is adapted from [45].

The group VI TMDs are large-gap semiconductors and share similar electronic structures [45]. As ARPES can hardly detect the unoccupied states in the conduction band, we will focus on the valence band structure of TMDs. Unlike the single-orbital-dominant (p_z) low-energy bands in graphene, TMDs present a multi-valley and multi-orbital structure [Fig. 2.4(a)]. The K valley of TMD is mainly contributed from in-plane orbitals (metal d_{xy}, $d_{x^2-y^2}$/chalcogen p_x, p_y orbitals), while the Γ valley mainly consists of out of plane orbitals (metal d_{z^2} and chalcogen p_z orbitals). As a result, the valence band maximum (VBM) and the band gap are strongly thickness-dependent due to the hybridization of Γ valley bands. For example [47], the bulk crystal of MoS_2 has a 0.88 eV indirect band gap and the VBM is located at the Γ point [Fig. 2.4(b)]. As interlayer coupling strength decreases with the number of layers, the binding energy of Γ valley top goes down and the VBM shifts to the K point in the monolayer, which results in a 1.71 eV direct band gap.

TMDs have many advantages as building blocks for 2D heterostructures. The most important one is that TMDs are semiconductors, which have promising potential for electrical and optical applications. Besides, TMDs can serve as a multi-functional platform to realize different quantum models due to the multi-valley

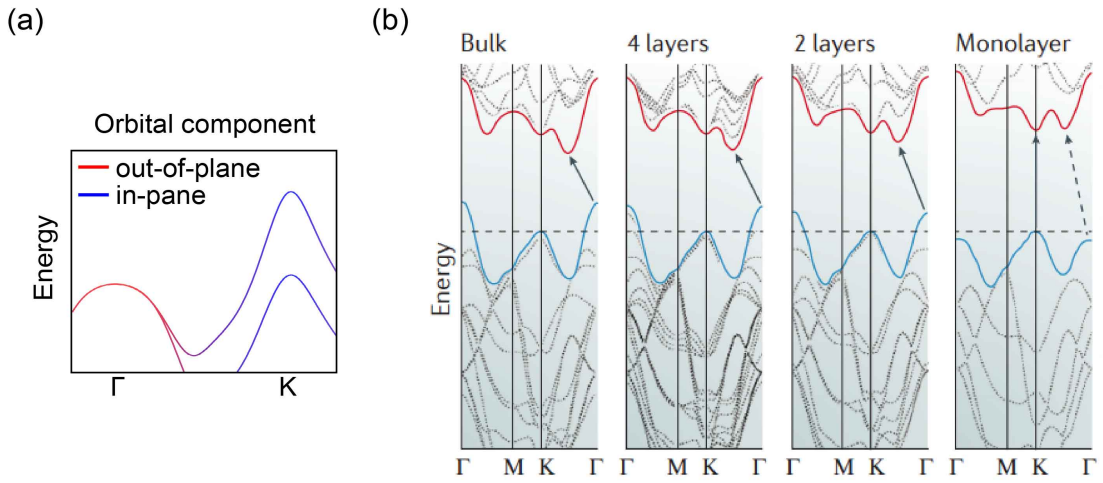

Figure 2.4: Electronic structure of TMDs. (a) Orbital components in the electronic structure of monolayer TMD. The in-plane orbitals (indicated by blue lines) include metal d_{xy}, $d_{x^2-y^2}$/chalcogen p_x, p_y orbitals; the out-of-plane orbitals (indicated by red lines) include metal d_{z^2} and chalcogen p_z orbitals. (b) Evolution of electronic structure from bulk to monolayer. The highest valence band and the lowest conduction band are highlighted in blue and red, respectively. The band gap is indicated by the arrow. (b) is adapted from [45].

electronic structure (triangular models for the K-valley and hexagonal models for the Γ valley).

2.2 Moiré in twisted 2D materials

2.2.1 Twist-modified electronic structure

Since the discovery of graphene, physicists have realized that the manipulation of rotation freedom in a crystalline material becomes a feasible idea. In 2007, Castro Neto and his colleagues suggested that pressing two misaligned graphene sheets might produce novel electrical and optical properties [48], which inspired some pioneer exploration on twisted graphene. In 2011, MacDonald and his colleagues proposed that twisted graphene at particular small angles (also known as the 'magic angles') can host extreme flat band, which can lead to strongly correlated phases [49]. This idea was first experimentally realized by Pablo's group, who found Mott insulating and unconventional superconducting states in the magic angle twisted bilayer graphene [37, 39]. Soon, various non-trivial quantum phenomena (e.g., orbital magnet, QAH insulator [50]) were also realized in twisted bilayer

[38, 41], trilayer [51], double-bilayer graphene [52, 53], twisted TMDs [54] and other 2D heterostructures [55–57].

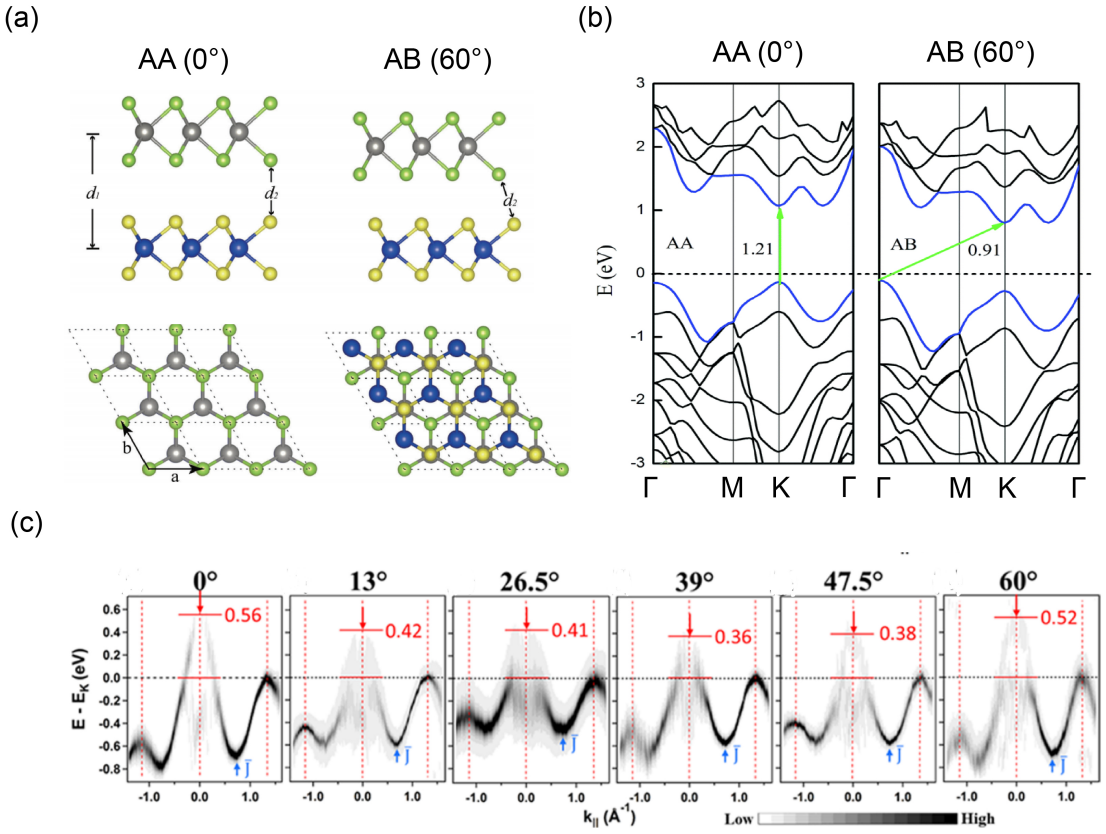

Figure 2.5: Twist-modified stacking order. (a) Illustration of AA and AB stacking bilayer TMDs. The top and bottom panels show the side-view and the top-view of TMD crystal structures. d_1 stands for the closest interlayer distance between metal atoms. d_2 stands for the closest interlayer distance between chalcogen atoms. (b) Calculated electronic structure of AA and AB bilayer TMDs. The band gap is indicated by green arrows. (c) Evolution of Γ-valley top with the twist angle in twisted bilayer MoS_2. (a) is adapted from [58]; (b) is adapted from [59]; (c) is adapted from [60].

From the perspective of real space, twist changes the stacking order of the heterostructure and alters the overlapping of orbitals oriented in the out-of-plane direction.

For example, the intrinsic bilayer TMDs are stacked in the AB order (the top layer metal atom is located in the center of the bottom layer hexagon), which can be viewed as the 60° rotated AA-stacking bilayer (the top layer metal atom is located on the top of bottom layer metal atom) [Fig. 2.5(a)]. The interlayer distance d_1 and the bond length between chalcogen atoms d_2 are significantly different in

different stacking orders, which is directly reflected on the electronic structure with out-of-plane orbital characters [58]. From the calculated electronic structure [Fig. 2.5(b)], the Γ-valley band top in AB-stacking bilayer is significantly higher than the K-valley band top, while in the AA-stacking bilayer the Γ and K valleys have similar binding energy. This difference can be attributed to the decreased d_1 that enhances the overall interlayer orbital overlapping, which increases the energy splitting between bonding and anti-bonding states in the Γ valley [59]. Twisted bilayer TMDs with a twist angle between 0° and 60° can be viewed as a system mixed of AA, AB stacking areas with different percentages, the binding energy of the Γ valley varies as the twist angle and stacking order change, as shown in the ARPES results on twisted bilayer MoS_2 [Fig. 2.5(c)] [60].

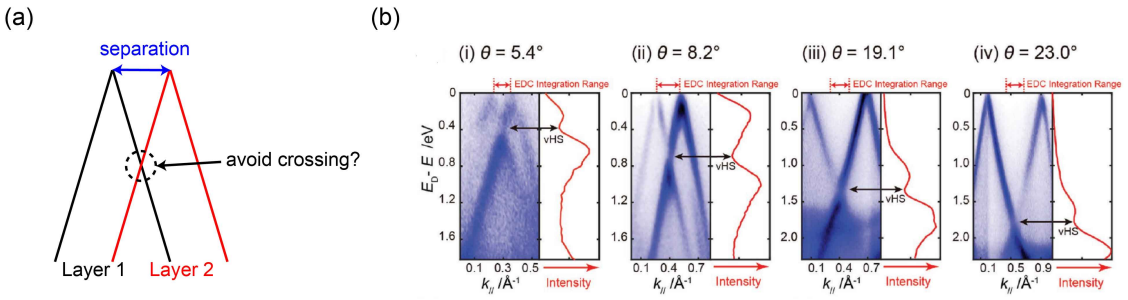

Figure 2.6: Twist-induced van Hove singularity. (a) Illustration of twist-induced momentum separation of electronic structures of different layers. (b) Evolution of the binding energy of van Hove singularity in twisted bilayer graphene. (b) is adapted from [61].

From the perspective of reciprocal space, twist can result in a momentum separation between the nominally same band in each layer and create multiple band crossing points. Eletronic structure around the crossing point will be renormalized if the band hybridization is strong.

For example, in twisted bilayer graphene [61], the Dirac cones of layer 1 and layer 2 will be separated by a distance (δk) that follows the relation, $\delta k = 2d * sin(\theta/2)$, where d is the distance between the Γ and K points and θ is the twist angle [Fig. 2.6(a)]. There is a crossing point whose binding energy is proportional to δk and the Fermi velocity, and electronic states from different layers share the same set of quantum numbers at this point. According to the Pauli exclusion

principle (Pauli rule), two identical fermions cannot exist in the same quantum system. Since the Dirac cones are contributed by p_z and the interlayer coupling in graphene is strong, electronic states in different layers should stay in the same system. Thus, band dispersions of different layers should avoid crossing, which has been experimentally observed by ARPES on twisted bilayer graphene [Fig. 2.6(b)]. Accompanied with the gap opening, the nearby band dispersion will become flattened, leading to the formation of van Hove singularity in the density of states (DOS) [61]. We should notice that the prerequisite for the Pauli rule is the same quantum system. It remains unclear if there will be a gap opening between two bands with weak interlayer coupling.

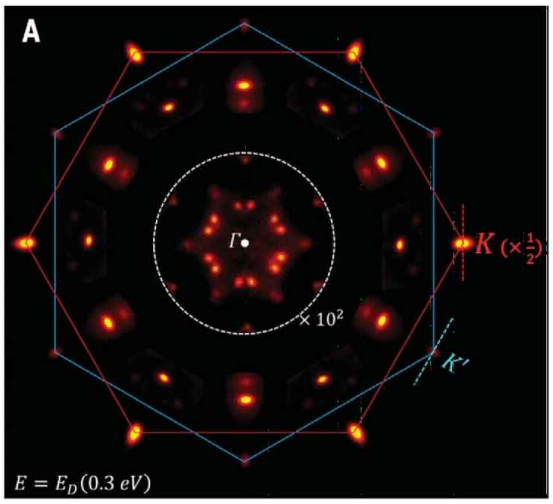

Figure 2.7: Twist-induced Umklapp scattering. Bule and red hexagons stand for BZs of 30° twisted bilayer graphene. Bright spots at BZs' corners are the orginal Dirca cones of graphene. Other additional spots are replica Dirac cones generated from Umklapp scattering. This figure is adapted from [62].

Moreover, in twisted 2D materials, each layer serves as a competing periodic potential for the other layer that moidifies the electronic structure [63–65]. For example, in graphene quasicrystal (30° twisted bilayer graphene) [Fig. 2.7] [62, 66], multiple replica Dirac cones are visible in the ARPES equal energy contour, in addition to the 12 original ones. This phenomena is related with Umklapp scattering, where the additional electronic states are the scattered states from one

layer by the potential of the other layer. The detailed interperation of Umklapp scattering is available in Chapter 4.

2.2.2 Moiré bands

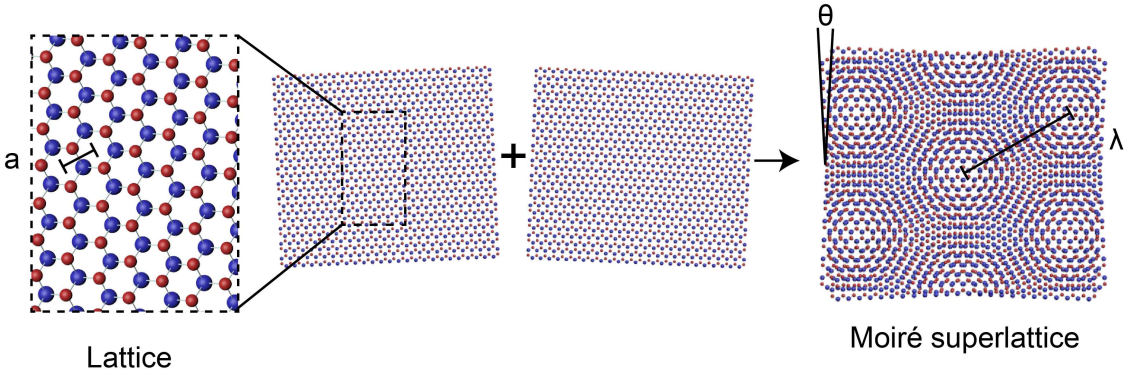

Figure 2.8: Moiré superlattice. Two layers of TMDs (lattice constant a) are stacked with a twisted angle θ to form a moiré superlattice (moiré length λ).

The term *moiré pattern* refers to a large-scale interference pattern produced by overlapping two similar patterns, which is widely used in mathematics, physics, and art. For the moiré pattern to appear, the two patterns must not be completely identical, but rather displaced, rotated, or have slightly different pitch. In condensed matter physics, the moiré pattern can be formed when two layers of 2D materials are stacked with a twist angle. (The moiré pattern can also be formed by stacking two layers of 2D materials with different lattice constants at zero twist angle.) The term *moiré superlattice* is defined as the commensurate superlattice formed by both layers. It only appears when the twist angle θ meets the commensurate condition [66], $cos\theta_{p,q} = \frac{3p^2+3pq+q^2/2}{3p^2+3pq+q^2}$, where p and q are two coprime positive integers. Strictly speaking, moiré bands are only well-defined in the moiré superlattice due to the existence of new periodicity. In realistic case, the separation between two commensurate angle is tiny enough (compared with the experimental resolution) when p is large, so that we can ignore the angle difference and assume small angle ($<2°$) twist 2D materials host moiré superlattices. For example, $\theta_{16,1} = 2.00°$, $\theta_{17,1} = 1.89°$, $\theta_{16,1}$-$\theta_{17,1} = 0.11°$. If we stack two layers of hexagonal lattices (lattice constant a) with θ to form a moiré superlattice [Fig. 2.8], the moiré length λ

follows the relation, $\lambda = \frac{a}{2sin(\theta/2)}$. Usually, λ is more than 20 times larger than a (e.g., $\theta = 5°$, $\lambda = 22.92\ a$).

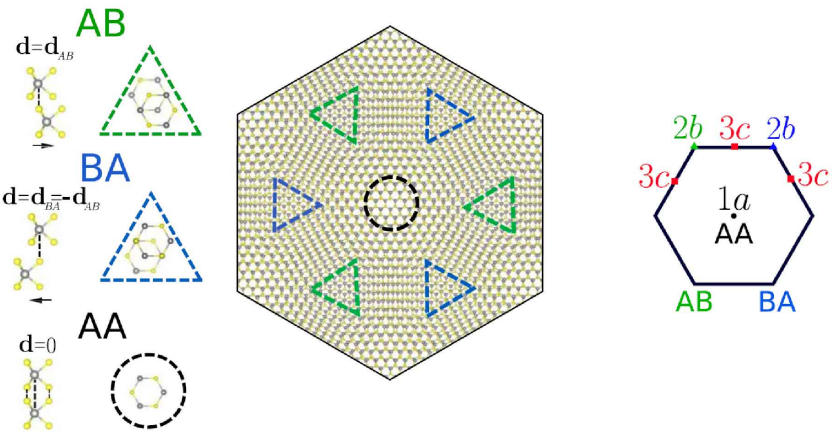

Figure 2.9: High-symmetry sites in moiré superlattice. Left: definitions of AA, BA, AB sites in the twisted TMDs moiré superlattice. Here, AA means eclipsed stacking sites with metal atom over metal atom; AB and BA stand for Bernal stacking, including two inversed configurations with metal atom over chalcogen atom or chalcogen atom over metal atom. Right: wyckoff positions in the twisted TMDs moiré superlattice. This figure is adapted from [67].

According to the stacking order, we can define high symmetry sites in the moiré superlattice [67]. Here, we use twisted TMDs as an example [Fig. 2.9]. AA site (or A site) means the eclipsed stacking with metal atom (M) over metal atom, chalcogen atom (X) over chalcogen atom. AB and BA sites (or B sites in general) mean the staggered stacking with X over M, or M over X. In some literature, the bridge that connects neighbouring AA sites is define as the BR site. In the term of Wyckoff position, the moiré superlattice follow the symmetry of the wallpaper group 17, where AA, B, and BR sites are located at 1a, 2b, 3c positions, respectively. These definitions of high symmetry sites are concise for the discussion of electron distribution in the real space.

The moiré superlattice introduces an additional periodic potential that electrons move through, giving rise to emergent electronic structure called moiré bands [36]. If the moiré potential is comparable with the original potential in a monolayer, the moiré superlattice should be viewed as a totally new structure and moiré bands can be directly calculated by the first-principle calculation and presented in the

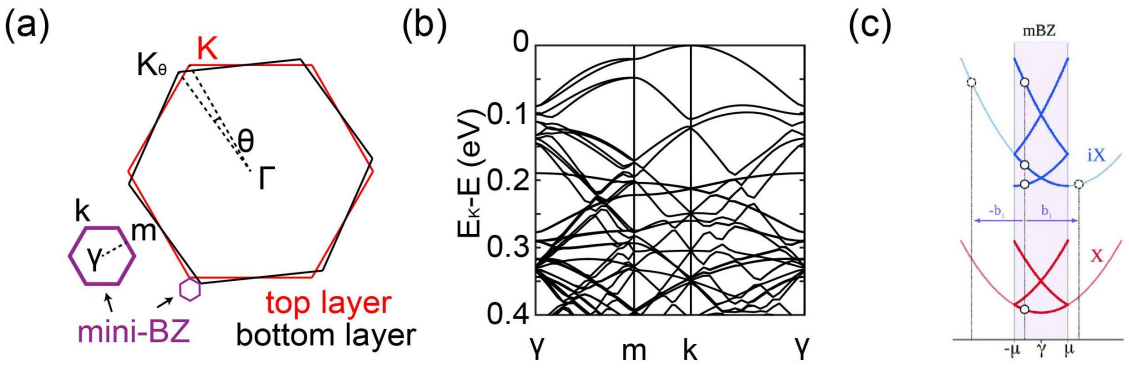

Figure 2.10: Moiré bands. (a) Original BZ of each layer and mini-BZ moiré superlattice, labelled with high symmetry points. (b) Electronic structure of 5.09° twisted WSe_2 presented in mini-BZ. (c) Illustration of folded bands (thick lines) and unfolded bands (thin lines) in the BZ and mini-BZ, respectively.

mini-BZ of moiré superlattice [Fig. 2.10(a)]. As shown in the calculation result [Fig. 2.10(b)], dozens of bands with the band width magnitude of 10 meV are compressed in a tiny energy range. This seemingly messy band structure results from the band folding and hybridization [Fig. 2.10(c)]. As the moiré superlattice is usually 20 times larger than the monolayer lattice, the original band is divided into more than 20 segments and translated (folded) into the mini-BZ, and some segments hybridize with others to create more complex structures. To some extent, the formation of moiré bands can be viewed as the band folding in a 20×20 charge density wave induced by twist, but remains stable against the temperature change. We notice the prerequisite for the above-mentioned scenario is the strong moiré potential. If the moiré potential is weak, no moiré bands but only small disturbance is expected to accompany with the original band of monolayer.

The essense of moiré-related exotic phenomena lies in the tiny width of moiré bands [36]. Thanks to the advance of electrostatic gating technique, the chemical potential of twisted 2D materials and the filling level of moiré bands can be continuously tuned. At the right filling level, the strength of electron-electron interaction in the moiré band can be larger than the band width. As a result, strongly correlated states and associated phase transition can be precisely manipulated in the moiré system. The first material realization was the 1.05° twisted bilayer graphene (MATBG) [37, 39]. The band structure of MATBG presents a moiré band with

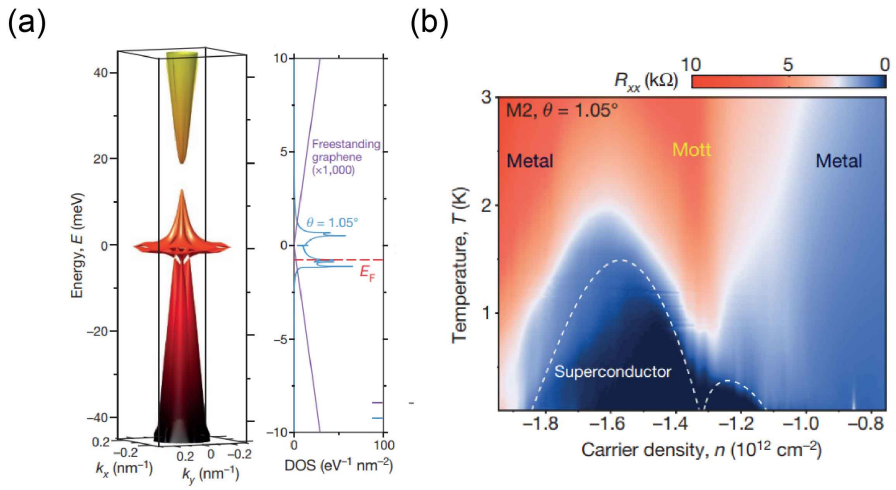

Figure 2.11: Strongly correlated states in moiré superlattice. (a) Left: illustration of isolated flat band in 1.05° twisted bilayer graphene. Right: enhanced DOS peaks around E_F. (b) Phase diagram obtained by transport measurements on 1.05° twisted bilayer graphene. This figure is adapted from [39].

∼1meV band width isolated from other band structure, leading to a sharp peak in the DOS [Fig. 2.11(a)]. By tuning the carrier density (chemical potential) in this system, Mott insulating states were found around half-filling of the moiré band and the superconducting dome was observed slightly away from half-filling [Fig. 2.11(b)]. This astonishing discovery inspired hundreds of groups to work on twisted 2D materials and rich exotic phases (orbital magnet, QAH insulator) have been revealed in various moiré systems [37–39, 41].

A complementary view of flat moiré band in real space is the electron localization on the so-called 'moiré orbital' [Fig. 2.12], which is defined on the moiré unit cell composed of hundreds of atoms. According to the geometry of moiré orbital, a low energy moiré band can be effectively described by a paradigmatic quantum model on the moiré length scale. These generated moiré bands could contribute to the transport properties by tuning the chemical potential via electrostatic gating, and the electron correlation strength as well as the band topology can be manipulated by various external parameters (e.g., strain, substrate, and displacement field). Therefore, twisted 2D materials with moiré superlattice can be regarded as a toolbox to realize controllable Hamiltonians and explore intriguing quantum phases [68].

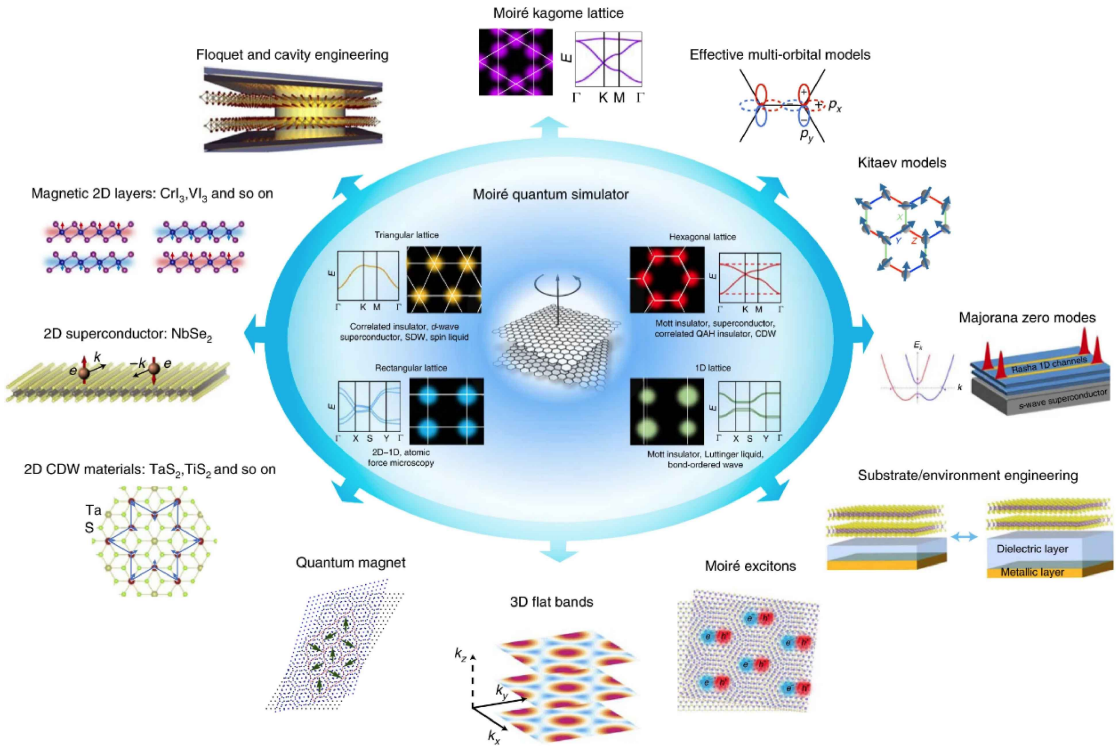

Figure 2.12: Moiré superlattice as quantum simulator. Inside the blue circle: moiré bands in the momentum space and associated charge distributions in the real space. Outside the blue circle: various quantum phases that could be found in the moiré superlattice. This figure is adapted from [68].

3

Electronic structure of twisted bilayer WSe_2

Contents

Recent transport measurements have revealed many exotic properties in twisted bilayer WSe_2 ($tbWSe_2$), such as correlated insulating and zero-resistance states, which are associated the moiré-modified electronic structure [54, 69, 70]. In this chapter, we present a systematic study on the electronic structure of 5.1° $tbWSe_2$. In the first section, background information about twisted transition metal dichalcogenides (tTMDs) is introduced. In the second section, methods used in this study are presented. In the following three sections, ARPES, scanning tunneling microscope (STM), and calculation results on $tbWSe_2$ are presented and discussed. A summary of this chapter is available in the last section.

3.1 Introduction

In the same year of the discovery of unconventional superconductivity in the magic angle twisted bilayer graphene [37, 39], M. Naik and M. Jain proposed that strongly correlated states can also be realized in tTMDs due to the existence of flat moiré bands [71]. In their density functional theory (DFT) calculation results, both 3.5° (close to AA stacking) and 56.5° (close to AB stacking) twisted bilayer MoS_2 host dispersionless moiré bands around the valence band edge, with the band widths of 23 meV and 5 meV, respectively [Fig. 3.1(a)]. Under p-type doping (via electrostatic gating), the chemical potential can be shifted down to these flat bands, and with proper filling level, the strength of electron-electron interaction in these flat bands can have the same magnitude as the band width. As a result, these flat moiré band can contribute to the electrical transport properties and possibly lead to strongly correlated states. More interestingly, according to their prediction, these flat moiré bands can survive in a large twist angle range ($0° < \theta < 7°$ or $52° < \theta < 60°$), and can emerge in all tTMDs due to the similarity of electronic structure.

Soon after the first DFT calculation, A. MacDonald and other pioneers established various analytical models to explore the intriguing physics in tTMDs [67, 72, 74]. In 2018, by studying the twisted $WSe_2/MoSe_2$ hetero-bilayer [74], they found the K-valley flat moiré bands can be described by a triangular lattice Hubbard models and proposed that when the K-valley flat moiré bands are partially filled,

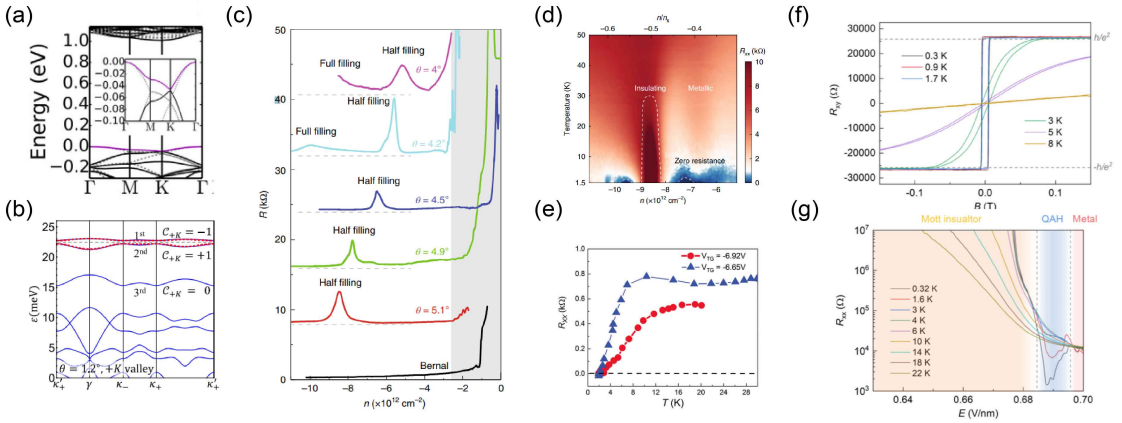

Figure 3.1: Recent advance of research on tTMDs. (a) Calculated Γ-valley flat band (twisted angle 5.1°C). (b) Calculated K-valley flat band (twisted angle 1.2°C). (c)(d) Transport measurements showing correlated insulating and zero-resistance states in tbWSe$_2$. (e) Transport measurements showing the zero-resistance states in twisted double-bilayer WSe$_2$. (f) QAH effects in the AB-stacked MoTe$_2$/WSe$_2$. (g) Electrical-field-driven topological phase transition in the AB-stacked MoTe$_2$/WSe$_2$. (a) is adapted for [71].(b) is adapted from [72]. (c)(d) are adapted from [54]. (d) is adapted from [70]; (f)(g) are adapted from [73].

many-body ground states, such as quantum anomalous Hall (QAH) insulators and chiral d-wave superconductors, can be realized. In 2019, by studying the twisted bilayer MoTe$_2$ [72], they found the K-valley flat moiré bands can be described with a two-band model with a layer-pseudospin magnetic field. By calculating the topological invariants of the K-valley flat moiré bands [Fig. 3.1(b)], they found tTMDs can be a topological insulator at a specific twist angle and under a certain electrical field, which means a continuous topological phase transition is experimentally feasible in tTMDs. In 2021, they found the Γ-valley moiré bands are qualitatively different from the K-valley counterparts due to the emergent D_6 symmetry in the moiré superlattice [67], which can realize both honeycomb and kagome models instead of the triangular model. As a result, frustrated phases, such as quantum chiral spin liquid, are also attainable in tTMDs.

Very recently, tTMDs have been proposed as a condensed-matter platform for realizing controllable quantum Hamiltonians [68]. This fancy idea starts from the complementary view of flat moiré band in real space, that is the electron localization on 'moiré orbitals' [75]. According to the geometry of moiré orbitals, a low energy

moiré band can be effectively described by a paradigmatic quantum model at the moiré length scale [67, 68, 72, 74, 76, 77]. As the lattice length, the electron correlation strength, and the band topology can be manipulated by various external parameters, such as strain, substrate and displacement field, the parameters of quantum model are highly tunable [37–39, 41, 54, 78, 79]. Besides, the same tTMDs system can host multiple types of quantum models due to the multi-valley electronic structure, and by tuning the chemical potential we can easily switch between these models [80–82]. Therefore, tTMDs can be regarded as a toolbox to realize controllable Hamiltonians and explore intriguing quantum phases.

Some of the above-mentioned scenarios have already been experimentally realized in tTMDs. C. Dean and his colleagues reveal that correlated insulating states (at the half filling) can be realized in $tbWSe_2$ with a large angle range (from 4° to 5.1°) [Fig. 3.1(c)] [54, 69], in sharp contrast with the twisted bilayer graphene in which the twist angle is limited in 1.1±0.2° [37–39]. More interestingly, zero-resistance states are found slightly away the half-filling in the 5.1° sample (close to the commensurate angle 5.09°) [Fig. 3.1(d)] [54]. However, whether these states are the superconducting states is still under debate due to the lack of magnetic evidence [54]. Similar zero-resistance states have also been observed in the 2° twisted double-bilayer WSe_2 [Fig. 3.1(e)] [70]. As the VBM of $tbWSe_2$ is the K point while the VBM of twisted double-bilayer WSe_2 is the Γ point, these transport results indicate that moiré bands from both kinds of valleys can lead to strongly correlated phases. Very recently, the QAH insulator and an electrical-field-driven topological phase transition have been observed in the transport measurements on the AB-stacked (60°) $MoTe_2/WSe_2$ [Figs. 3.1(f)(g)], which also demonstrates tTMDs as a promising platform to study topological phases [73, 83].

Though transport results have revealed non-trivial quantum phases in tTMDs [54, 69, 70], consistent with the theoretical prediction [71], the key evidence for supporting the moiré interpretation-the observation of the moiré bands and associated charge distributions, is still lacking. STM is powerful in mapping out the charge distribution in the real space and resolving tiny structure in the local density

of states (LDOS), though its lack of momentum resolution hinders the accurate interpretation of the valley dependence. This shortcoming can be compensated by the combined usage of nano-ARPES [84–88], which can directly visualize the electronic structure in the momentum space. In this study, using both kinds of state-of-the-art techniques [Fig. 3.2], we systematically investigated the electronic structure of 5.1° $tbWSe_2$. First-principles and tight-binding calculations were also performed to understand the experimental results.

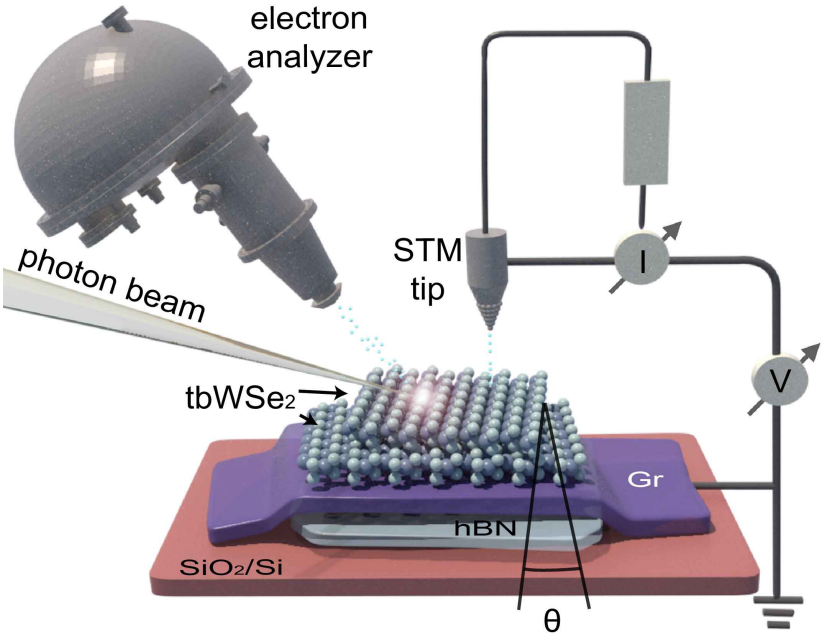

Figure 3.2: Device design and experiment layout. Schematic illustration of the device design and the experiment layout. From bottom to top, the red, light-blue, purple sheets stand for SiO_2/Si, hBN and graphite substrates, respectively; the atomic model stands for a bilayer WSe_2 with a twist angle (θ); for ARPES measurements, photoelectrons are collected by a hemisphere analyzer; for STM measurements, tunnelling electrons are tuned by the current (I) and voltage (V) sources and collected by the STM tip.

3.2 Methods

Sample fabrication

In this study, we used two $tbWSe_2$ devices that are slightly different in the substrate. The first device, in which the $tbWSe_2$ sample was directly transferred onto the highly oriented pyrolytic graphite (HOPG), is named as '$sample_{HOPG}$'

; the second device is named as '$sample_{hBN}$', where the $tbWSe_2$ sample was transferred onto a substrate composed of multilayer-graphene, hBN and SiO_2/Si (in the sequence from top to bottom).

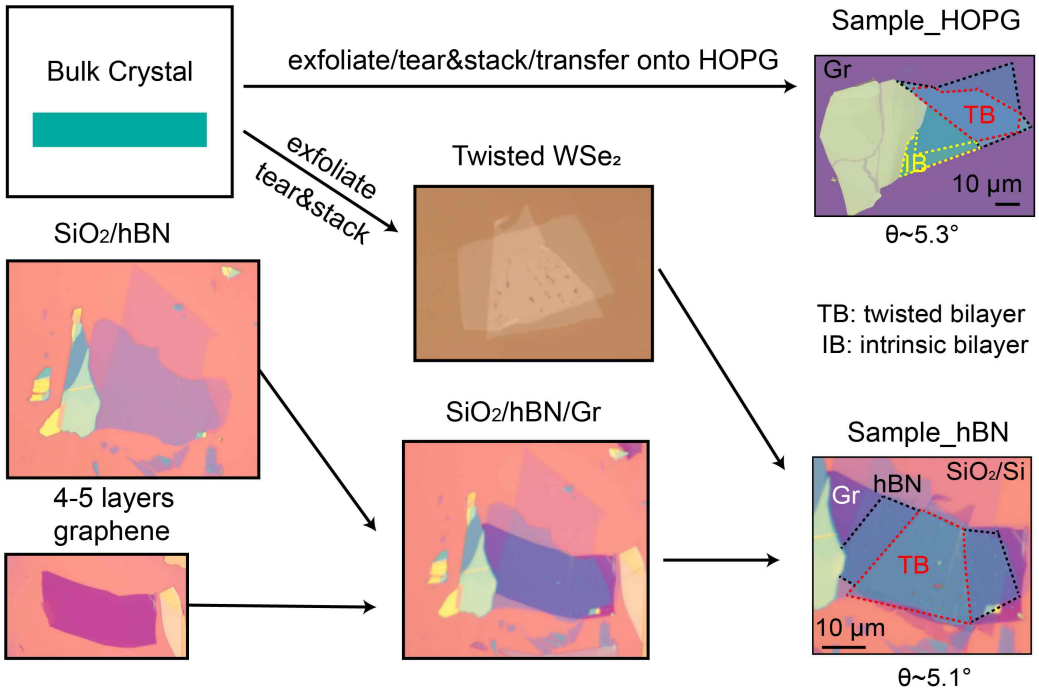

Figure 3.3: Device fabrication procedures.

Here, detailed procedures for the fabrication of $sample_{hBN}$ are presented. The $tbWSe_2$ sample was fabricated by using a dry-transfer technique [Fig. 3.3]. The monolayer and few layers WSe_2 flakes were mechanically exfoliated from bulk crystal onto the SiO_2 wafer. Polycarbonate film was used to tear part of the target monolayer WSe_2 at around 80°C to 100°C The left part of WSe_2 was rotated manually by a twist angle (θ) of around 5.1° (±0.1°) and stacked together. For the substrate part, few layers boron nitride films with a thickness of 10 nm to 20 nm were exfoliated on the silicon wafer. Then 4-5 layers graphite thin films were picked up by polycarbonate film and transferred onto the prepared boron nitride. Then the $tbWSe_2$ was transferred onto the graphite thin film. In the final step, Cr/Au 5 nm/7 nm was deposited on part of the sample and graphite to form the contact.

STM measurement

Table 3.1: Table of tight-binding parameters.

E_{p_z}	E_{p_x}, E_{p_y}	$E_{d_{Z^2}}$	$E_{d_{xz}}, E_{d_{yz}}$	$E_{d_{xy}}, E_{d_{x^2-y^2}}$	$V_{pp\sigma}^{intra}$	$V_{pp\pi}^{intra}$	$V_{pp\sigma}^{inter}$	$V_{pp\pi}^{inter}$
-4.328	-3.778	-2.066	-1.075	-2.153	0.713	-0.214	1.344	-0.294
$V_{pd\sigma}^{1NN}$	$V_{pd\pi}^{1NN}$	$V_{pd\sigma}^{2NN}$	$V_{pd\pi}^{2NN}$	$V_{dd\sigma}$	$V_{dd\pi}$	$V_{dd\delta}$		
-2.258	1.263	-0.505	-0.050	-0.869	1.311	-0.045		

The STM measurements on sample$_{hBN}$ were performed under ultrahigh vacuum (pressure better than 10^{-11} mbar) and liquid-helium temperature with an Omicron low-temperature STM. The etched tungsten wires were used as the STM tip. The constant-height dI/dV spectroscopy was acquired by turning off the feedback loop and using the standard lock-in techniques (f = 991.7 Hz, V_{Ampl} = 4 mV). The constant-current dI/dV spectroscopy was acquired by leaving on the feedback loop. The tip-sample distance Z changed to keep the constant tunneling current, while the bias voltage was scanned. The tip was calibrated on Ag (111) before measurements on the samples. STM data were analyzed using SPIP 6.7.3 and MATLAB.

ARPES measurement

ARPES measurements were performed in ANTARES beamline of Synchrotron Soleil and SpectroMicroscopy beamline of Elettra Sincrotrone Trieste. Samples were annealed at 300°C for 4 hours before ARPES measurements. All experiments were performed with a base vacuum better than 3×10^{-10} mbar. Experiments in Elettra were performed at 94 K with photon energies of 27 and 74 eV. The estimated energetic and angular resolutions were around 50 meV and 0.3°, respectively. Experiments in Soleil were performed at 75 K with a photon energy of 100 eV. The estimated energetic and angular resolutions were around 30 meV and 0.5°, respectively. All ARPES results presented in this chapter were obtained with photon beam in linear horizontal (LH) polarisation.

Calculation method

The first-principle calculations are performed by using the Vienna ab initio simulation package (VASP) with the projector-augmented wave potential method [89]. The exchange-correlation potential is described using the generalized gradient approximation (GGA) in the Perdew-Burke-Ernzerhof (PBE). The energy cutoff of

the plane-wave basis set is 300 eV. A vacuum region larger than 15 Å is applied to ensure no interaction between the slab and its image. In our optimization, all structures are relaxed until the force on each atom is less than 0.01 eV/Å. The Van der Waals interactions between the adjacent layers are considered by using zero damping DFT-D3 method of Grimme.

We unfold the bands of twisted bilayer to the primitive-cell Brillouin zone of a monolayer. The tight-binding method is adopted to calculate the unfolded bands of $tbWSe_2$. The band structure of monolayer WSe_2 can be described by a tight-binding Hamiltonian consisting of 11 atomic orbitals, the d orbitals for W and the p orbitals for Se. Here, we consider the first-neighbor W-W, Se-Se, W-Se hopping terms, and the second-neighbor W-Se hopping term to improve the accuracy. The tight-binding parameters are obtained by fitting the low energy conduction and valence bands, which are given in table [3.1]. The effect of SOC is included by adding an on-site term $\sum_\alpha \lambda_\alpha \vec{L} \cdot \vec{S}$ in the Hamiltonian, where α stands W or Se atom. The parameters of SOC terms are taken from ref. [90].

For bilayer WSe_2, the interlayer hopping Hamiltonian includes the interaction between the Se atoms at the interface of the bilayer, i.e., p-p interlayer coupling. The bonding integrals $V_{pp\sigma}$ and $V_{pp\pi}$ are taken from ref. [90], the expression is $V_{pp,b}(r) = \nu_b exp[-(r/R_b)^{\eta_b}]$ where $b = \sigma$, π, and the constant values ν_σ, R_σ, η_σ, ν_π, R_π, η_π are 2.559 eV, 3.337 Å, 4.114, -1.006 eV, 2.927 Å, 5.185, respectively. To improve the accuracy of the highest valence bands at Γ, the interlayer coupling between d_{z^2} and p_z are included in the interlayer hopping Hamiltonian. Similar to the process in ref.[90], we obtain the empirical expressions for the bonding integrals $V_{pd\sigma}$ and $V_{pd\pi}$, $V_{pd\sigma}(r) = A + Br$, $V_{pd\pi}(r)) = \nu exp[-(r/R_0)^\eta]$, where A, B, ν, R_0, η are 0.376 eV, -0.051 eV/Å, -0.274 eV, 4.247 Å, 5.025, respectively. In our calculations, the cut-off distance of the interlayer hopping terms is 8 Å.

3.3 ARPES study on twisted bilayer WSe_2

Figure 3.4 presents an overview of ARPES results. In the nano-ARPES measurement on $tbWSe_2$, we usually map out the photoemission intensity from the valence band

edge (sometimes we use the core level of W or Se) to obtain the topography of sample, as presented in Figs. 3.4(a)(ii) and (b)(ii). This method is called the scanning photoemission microscopy (SPEM). By choosing proper energy range in SPEM, we can get highly consistent pictures with the optical images [Figs. 3.4(a)(i) and (b)(i)], which enables us to accurately focus on the wanted area. In tTMDs, the number of Γ-valley bands is related with the number of layer [80–82], so that we can use the SPEM intensity to tell the thickness of different areas. The constant energy contours (CECs) [Figs. 3.4(a)(iii) and (b)(iii)] present the multi-valley valence band structure of tbWSe$_2$, where the Γ valley appears as the round pocket located in the center of Brillouin zone (BZ), while the K valley appears as triangular pocket located at the conner. The K_2 valley is defined as the K valley located in the second BZ. In the following subsections, we will discuss the electronic structure around K, K_2 and Γ-valleys in detail.

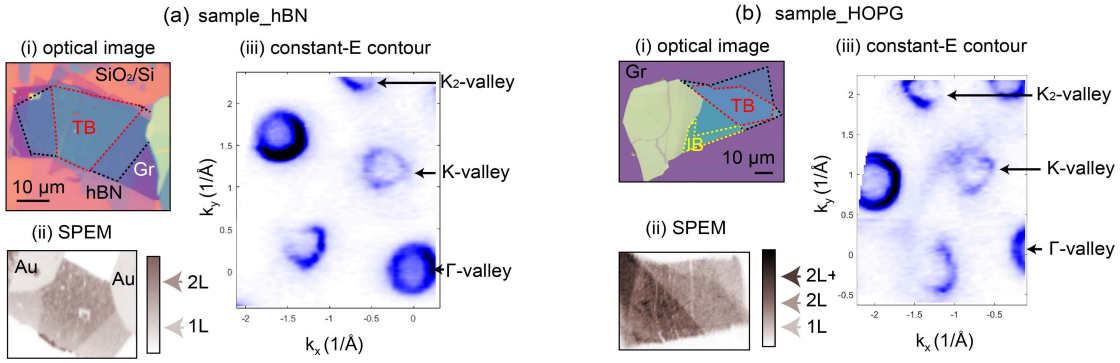

Figure 3.4: Overview of ARPES results on tbWSe$_2$. (a)(b) show the ARPES results on sample$_{hBN}$ and sample$_{HOPG}$, respectively. In both (a) and (b): (i) presents the optical image, the twisted bilayer (TB) and bottom monolayer regions are outlined by red and black dashed lines, respectively; in (b)(i), the intrinsic bilayer region is outlined by the yellow dashed lines; (ii) presents the SPEM image generated from mapping out the valence band top of Γ-valley, the intensity of which can be used to tell the number of layers in different regions. (iii) presents the broad range CEC (E$_B$ = 1.1 eV), in which Γ, K and K_2-valleys are indicated by black arrows.

3.3.1 Electronic structure around the K valley

The initial aim of this study was to search for the proposed flat band around the K-valley top [Fig. 3.5] [54]. According to the proposal, K-valleys of top and

bottom monolayer WSe_2 are separated in the momentum space due to the twist, which creates a crossing point in the middle. If the interlayer coupling of the K valley is strong, there should be a hybridization gap at the crossing point due to the Pauli exclusion principle [Fig. 3.5(a)]. The upper part of the overlapping bands will be shifted up due to the gap, and as a result, the K-valley top will be flattened. In this proposal, first-principles calculation shows an isolated and flat band in the mini-BZ [Fig. 3.5(b)]. This flat band can contribute to a sharp peak in the density of states (DOS) around the valence band edge, which is believed as the origin of correlated phases in tTMDs.

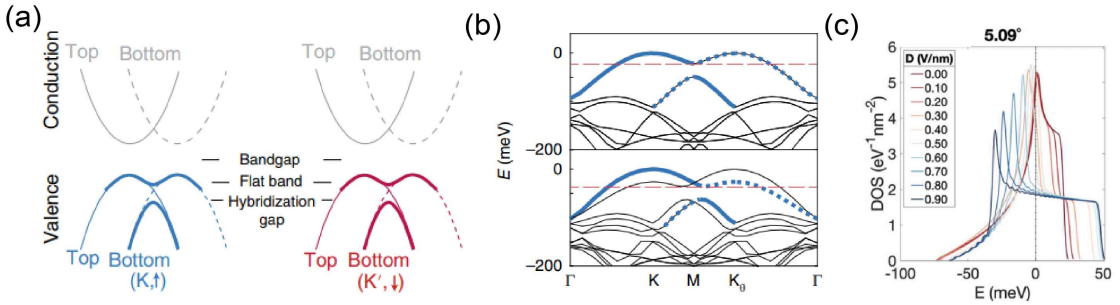

Figure 3.5: Proposed K-valley flat bands. (a) Illustration of the twist-induced band hybridization around K-valleys. The flat band are highlighted by thick lines. (b) First-principles calculation showing the isolated and flat band at the valence band edge. (c) The evolution of calculated DOS with the displacement field. This figure is adapted from [54].

However, within the resolution of equipment, no obvious sign of the K-valley flat band has been observed in our ARPES measurements. Despite the peculiar features around the Γ-valley pocket (will be discussed later), the CEC of sample$_{hBN}$ [Fig. 3.6(a)] presents diminishing intensity at the left-upper side of the top layer K-valley , which can be attributed to photon-electrons from the bottom layer K-valley (noted at K_θ). In the energy-momentum dispersion across the K point [Fig. 3.6(b)], no flat band is observed at the K valley top, but the shadow band of K_θ valley is observed on the right side. To rule out the possible suppression of matrix element [12], the electronic structure around the K_2 valley was also examined. Consistently, the top layer K_2 valley is much more intensive than the bottom layer $K_{2\theta}$ valley

[Figs. 3.6(c)]. In the band dispersion along K_2-$K_{2\theta}$ direction [Figs. 3.6(d)], no signature of flat band is observed, either.

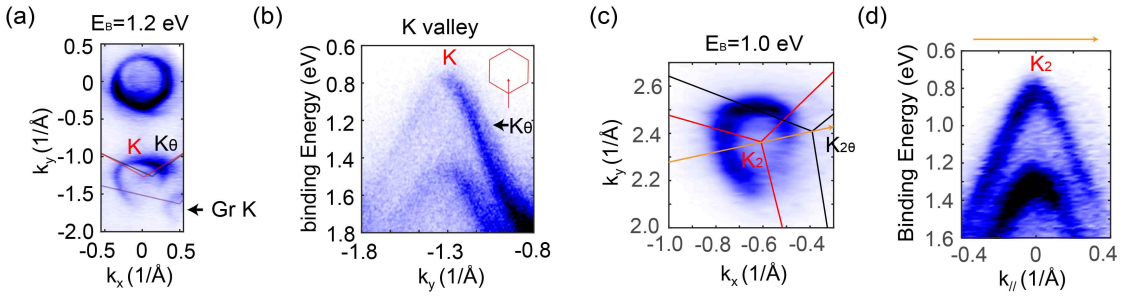

Figure 3.6: K-valley bands of sample$_{hBN}$. (a) CEC at E_B = 1.2 eV measured at 100 eV. (b) Band dispersion across the K point. (c) CEC at E_B = 1.0 eV around the K_2 valley measured at 74 eV. (d) band dispersion along K_2-$K_{2\theta}$ direction. In (a) and (c), red and black lines stand for BZs of the top and bottom layer WSe_2, respectively. The purple line in (a) stands for the BZ of graphite substrate. In (b), the red hexagon and arrow show the cut direction. In (c) and (d), the cut direction is indicated by the orange arrow.

The ARPES measurements on sample$_{HOPG}$ reveal similar results. The CEC at E_B = 1.0 eV presents intensive K_2 valley and weak $K_{2\theta}$ valley [Figs. 3.7(a)]. In the cut along K_2-$K_{2\theta}$ direction [Figs. 3.7(b)], neither the flat band nor the hybridization gap is observed. Interestingly, the CEC near the valence band edge (E_B = 0.85 eV) presents additional features apart from the K_2 and $K_{2\theta}$ valleys [Figs. 3.7(c)]. In the dispersion across such features [Figs. 3.7(d)], a mysterious K-valley-like band is immediately observed. Such additional band can be either the moiré-induced replica band or substrate-scattered band [85, 87]. Detailed study will be conducted in the future to clarify the origin of this mysterious band.

Our current ARPES results are not supportive for the scenario that K-valley flat bands are formed due to the opening of hybridization gap [54]. Especially, our observation challenges the base of band hybridization, that is the K and K_θ valleys belong to the same electronic system. In all ARPES results, photoemission intensity from the bottom layer is significantly lower than that of top layer, which means electrons of the bottom layer K-valley experience more complicated scattering process before escaping from the sample. It indicates the K-valley electrons are largely restricted in their resident monolayer and the interlayer hopping between K and K_θ valleys is too weak to form a unified system. The weak coupling at

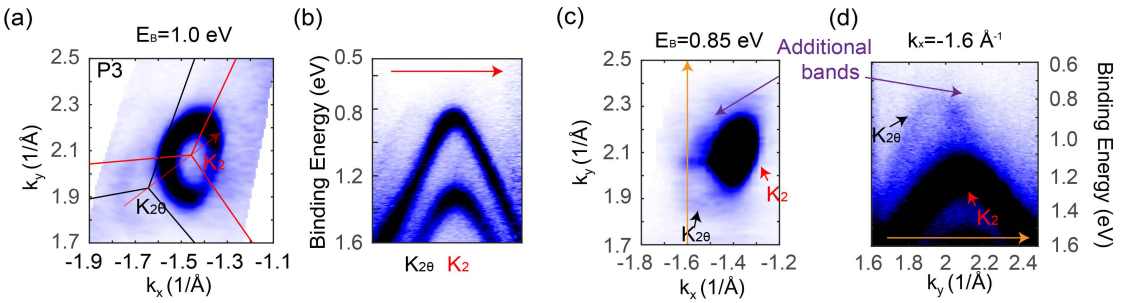

Figure 3.7: K-valley bands of sample$_{HOPG}$. (a) CEC at E_B = 1.0 eV around the K_2 valley measured at 74 eV. (b) Band dispersion along K_2-$K_{2\theta}$ direction. (c) CEC at E_B = 0.85 eV around the K_2 valley measured at 74 eV. (d) band dispersion along k_y direction at k_x = -1.6 Å^{-1}. In (a), red and black lines stand for BZs of the top and bottom layer WSe_2, respectively. In (a) and (b), the cut direction is indicated by the red arrow. In (c) and (d), the cut direction is indicated by the orange arrow; additional bands (than the top and bottom layer K-valleys) are highlighted by the purple arrows.

K-valley can be expected, as the K-valley is contributed from orbits with in-plane orientation (metal d_{xy}, $d_{x^2-y^2}$/chalcogen p_x, p_y orbitals) [Fig. 2.4(a)]. Previous layer dependent studies on TMDs also demonstrate that the K-valley is barely changed by the interlayer coupling [80–82].

Our ARPES measurements were performed without the displacement field (formed by the top and bottom gating voltages), which always accompanies the observation of strongly correlated phases in twisted TMDs, as it could be used tune the Fermi level as well as the strength of correlation. This discrepancy in experimental conditions may account for the absence of K-valley flat bands, as the displacement field could be the key factor to enhance the interlayer hopping [54, 69, 70]. However, we should notice other conditions, such as 3D lattice reconstruction that alters the overlapping of in-plane orbitals (recently observed in STM measurements on WSe_2/WS_2 bilayer), could also affect the K-valley electronic structure [91]. To find the very condition that indispensable for the formation of K-valley flat band, gating ARPES measurements should be performed in the future. (However, we cannot exclude the possibility that K-valley flat band does not exist under all conditions and correlated states originate from other features.)

3.3.2 Electronic structure around the Γ valley

In sharp contrast, the electronic structure around the Γ-valley presents prominent moiré bands. The CEC of sample$_{hBN}$ [Fig. 3.8(a)] shows inside ring-shaped and outside petal-like features, in addition to the intensive main band pocket. The momentum distribution curve (MDC) at $k_x = 0$ presents prominent main band peaks (indicated by the blue arrows) and weak peaks of additional features (indicated by the red arrows). Within the resolution of equipment, the momentum separation (δk) between the main and additional peaks can be regarded as a constant δk = 0.19±0.03 Å^{-1}. Consistent results have been observed in sample$_{HOPG}$, where δk is around 0.19 Å^{-1} [Fig. 3.8(b)]. These results are consistent with the moiré vector of 5.1° tbWSe$_2$ superlattice ($\mathbf{G_{moiré}}$, defined as the vector from the center of the first mini-BZ to that of the second mini-BZ), which has a length of 0.196 Å^{-1}. Based on these facts, we propose that these additional features are formed by the first order moiré replica bands. As illustrated in Fig. 3.8(d), the inner ring (highlighted in red) is formed by the replica of the main band (highlighted in blue) in all-six directions. The petal-like features are the edge of the replica bands. Further fine measurement with laser-based nano-ARPES (with higher energy and momentum resolution) is needed to search for other fine structures.

The symmetric replica-like bands are immediately observed in the energy-momentum dispersions along the k_y direction [Fig. 3.9]. In the cuts away from the BZ center, clear dispersions outside the main bands are observed, which form the petal-like features. Interestingly, the maxima of these bands are similar as that of the main bands, indicating the existence of fine structure near the Γ-valley edge that enhances the DOS. In the cuts near the BZ center, additional bands both inside and outside the main bands are observed, which form the ring-shaped and petal-like features.

To further validate the moiré origin, we discuss and exclude two common reasons for additional features in ARPES measurement on thin films. We first consider the substrate effect. The twist angle (θ_{Gr}) between graphite substrate and bottom layer WSe_2 was determined as around 11° [Fig. 3.10(a)], by overlapping BZs of WSe_2

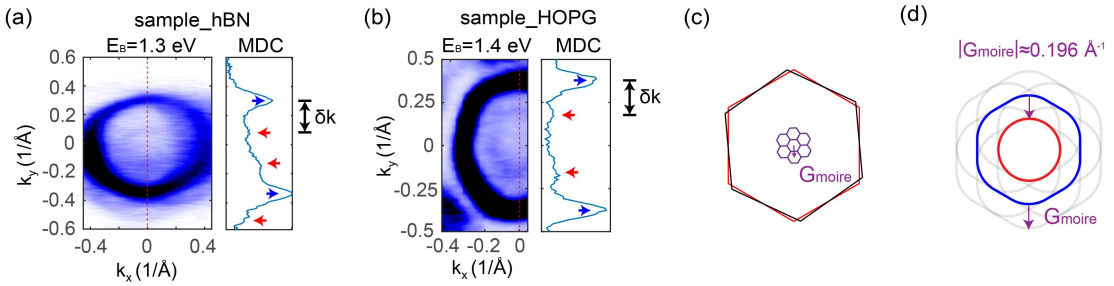

Figure 3.8: Constant energy contours of Γ valley. (a) CEC at $E_B = 1.3$ eV around the Γ valley of sample$_{hBN}$. (b) CEC at $E_B = 1.4$ eV around the Γ valley of sample$_{HOPG}$. In (a) and (b), the MDC across the Γ point (indicated by the red dashed line) is presented in the right part. Blue and red arrows indicate the MDC peak positions of the main band and the moiré bands. δk is the momentum spacing between the main bands and the moiré bands. (c) Illustration of the orientation of mini-BZs in (a); G_{moire} is the moiré vector defined as the vector between the closest two mini-BZs' centers. (d) Illustration of the CEC when the first order replica bands are considered. The main band is highlighted in blue; the inner circle formed by the moiré bands is highlighted in red. The purple arrows illustrate how the first order replica bands are generated.

and graphene onto CEC. The resulting BZ of WSe_2/Gr heterostructure (blue) has a reciprocal vector length of around 0.89 Å^{-1}, significantly larger than the BZs of tbWSe$_2$ superlattice (purple). Thus, we conclude additional features around the Γ valley unlikely result from substrate effects. Next, we consider the Umklapp scattering effect of the bottom layer electronic states. We find the Γ-valley top of monolayer WSe_2 is significantly lower than the additional bands [Fig. 3.10(b)] [82]. As Umklapp scattering only changes the momentum of the scattered states [85, 87], these additional bands cannot be the scattered Γ-valley states from the bottom monolayer. Therefore, we can safely conclude that our observation demonstrates the intrinsic moiré bands of tbWSe$_2$ superlattice.

The absence of K-valley flat band but strong evidence for Γ-valley moiré bands in ARPES measurements on the same samples seems rather anomalous. However, our observation is logically consistent with the orbital components of the band structure. The K valleys are contributed by orbitals with in-plane orientation (metal d_{xy}, $d_{x^2-y^2}$/chalcogen p_x, p_y orbitals) and weakly interacted with each other due to the small overlap of wavefunction and interlayer hopping (compared with Γ valley, which consists of metal d_{z^2} and chalcogen p_z orbitals). Indeed, the

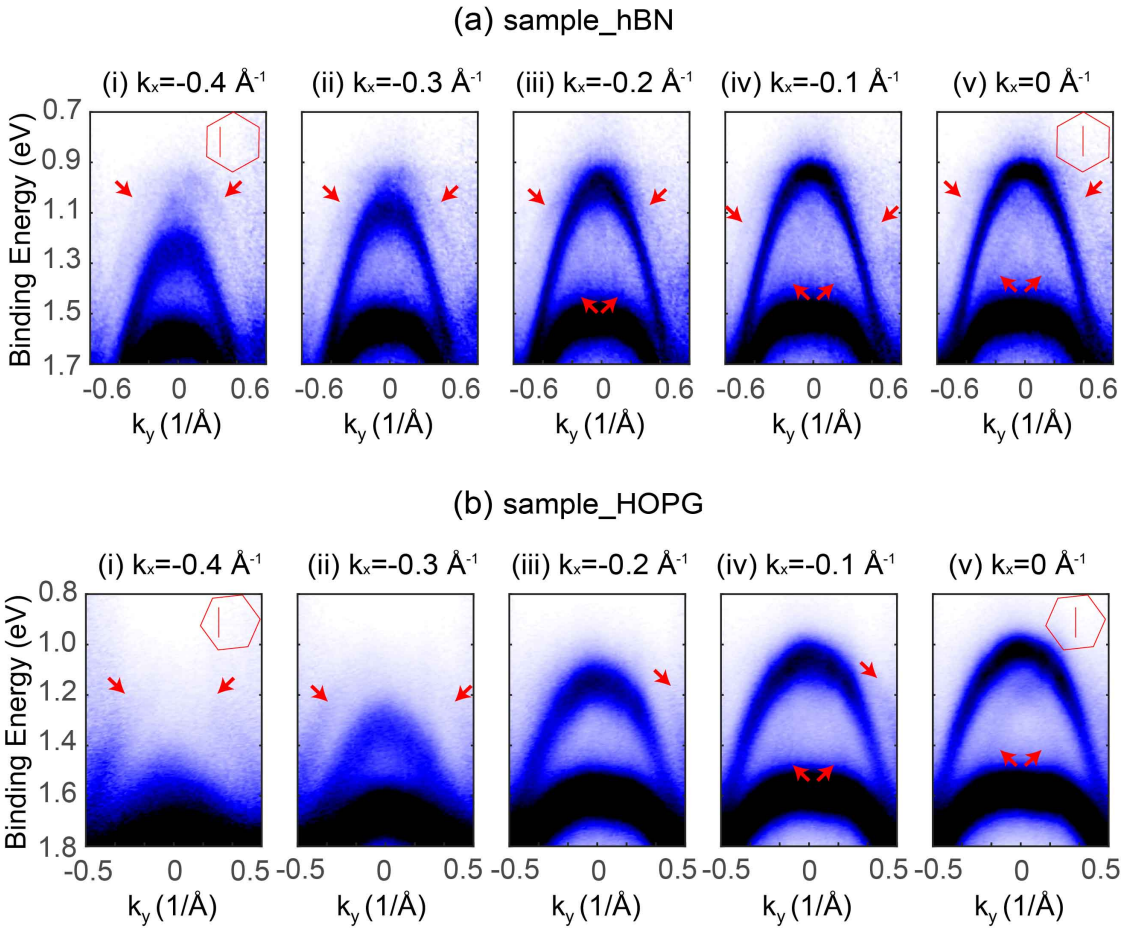

Figure 3.9: Energy-momentum dispersion around Γ valley. (a) Band dispersions of sample$_{hBN}$ along k_y (Γ-K direction) measured at (i)-(v) from k_x = -0.4 Å^{-1} to $k_x = 0$, respectively. (b) Band dispersions of sample$_{HOPG}$ along k_y measured at (i)-(v) from k_x = -0.4 Å^{-1} to $k_x = 0$, respectively. The inset red hexagons and lines show the orientation of BZs and the direction of cuts. Moiré bands are indicated by red arrows.

continuum theory predicts the moiré potential in K-valley model is less than one-fifth of that in Γ-valley model [67, 72, 74]. Such weak interaction may explain the disappearing of the K-valley moiré bands. On the other hand, the Γ-valley moiré bands, which originate from the variation of out-of-plane orbitals in moiré superlattice, are straightforwardly attainable.

Though our ARPES results point out the valley-dependent modification in twisted TMDs, strictly speaking, these results cannot lead to a conclusive understanding about the correlated states in transport measurements but raise more questions: 1. If the K-valley flat band exist, what is the formation condition? 2. If the K-valley flat band does not exist, is Γ-valley the origin for these correlated

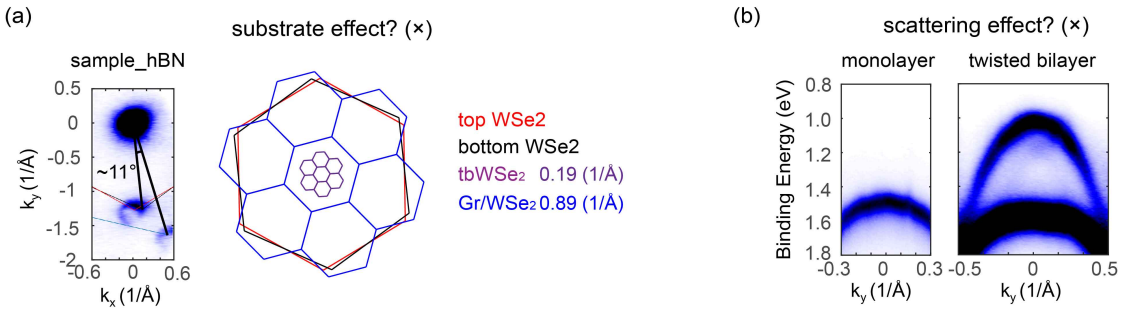

Figure 3.10: Discussion on substrate effects. (a) Left: Equal energy contour at E_B = 0.9 eV, overlapped with BZs of WSe_2 (red for top layer, black for bottom layer) and graphene (blue). The twist angle between BZs of bottom layer WSe_2 and graphene is around 11°. Right: BZs of top layer (red), bottom layer (black), the moiré superlattice (purple) of 5.09° $tbWSe_2$, and the Gr/WSe_2 superlattice (blue), respectively. (b) Band dispersion of monolayer and twisted bilayer WSe_2 across the Γ point.

states? To solve these questions, both gating ARPES measurements and a revisit to the transport results are needed.

3.3.3 Comparison between intrinsic and twisted bilayer WSe_2

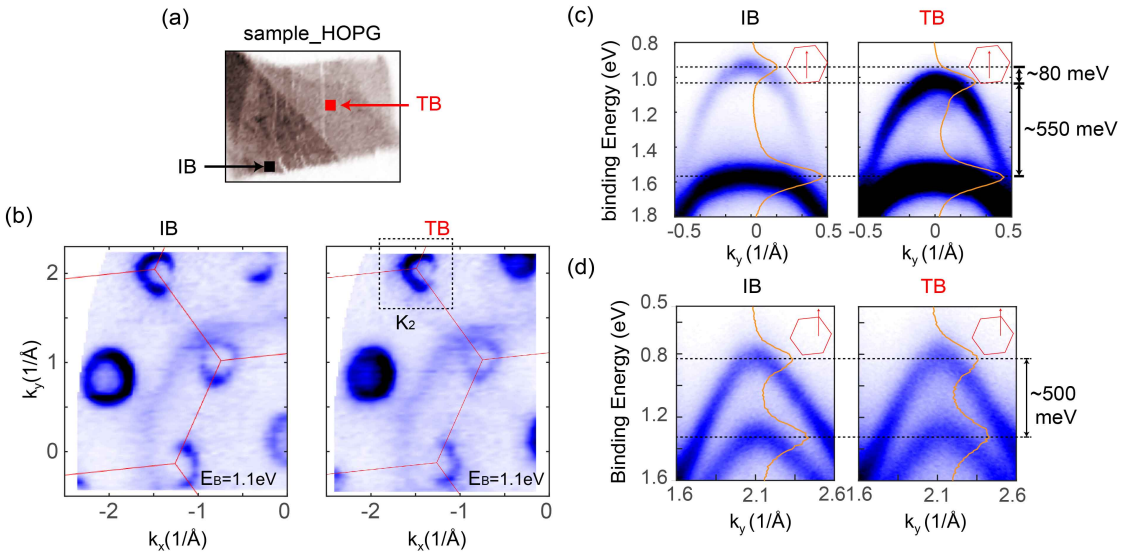

Figure 3.11: Comparison between intrinsic and twisted bilayer WSe_2. (a) SPEM image of sample$_{HOPG}$. The positions of IB and TB are indicated in red and black, respectively. (b) CECs at E_B = 1.1 eV of IB and TB; the BZ of top layer WSe_2 are indicated by the red lines. (c) Band dispersions across the Γ point of IB and TB. (c) Band dispersions across the K point of IB and TB. In (c) and (d), the inset red hexagons and arrows show the orientation of BZs and the direction of cuts; orange lines show the EDCs at the Γ and K points, respectively; black dashed lines show the peak positions of EDCs.

For a better understanding of the moiré-induced modification, we make a comparison of the electronic structures of intrinsic bilayer (IB, AB-stacked) and twisted bilayer (TB) WSe_2. $Sample_{HOPG}$ that contains multiple types of areas provides an ideal platform for studying IB and TB WSe_2 under the same experimental condition [Fig. 3.11(a)].

Despite the similarity between broad range CECs, an additional pocket aside the K_2 valley in TB is clearly observed while no such feature is found in IB, which is a direct evidence for the existence of twist angle [Fig. 3.11(b)]. The band dispersions of the Γ valley of IB and TB show significantly differences in three aspects [Fig. 3.11(c)]:1. TB shows distinguishable moiré bands inside the two main bands while IB shows no such feature, which reflects that the moiré superlattice can influence the electronic structure by introducing a competing periodicity. 2. The Γ-valley top of TB is around 80 meV lower than that of IB, which reflects that the moiré superlattice can influence the size of band gap by changing the stacking order. 3. The Γ-valley top of TB shows higher photoemission intensity than that of IB, indicating the DOS at Γ-valley edge can be enhanced by the moiré-induced band folding. However, no obvious divergence around the K-valley between IB and TB is observed [Fig. 3.11(d)], consistent with ARPES results on $sample_{hBN}$.

3.4 STM study on twisted bilayer WSe_2

To uncover the delicate structure of the moiré bands in $tbWSe_2$, STS measurement with milli-electron-volt energy resolution was performed on $sample_{hBN}$. High-symmetry sites in real space are defined as follows [Fig. 3.12(a)]: AA (marked in red) means eclipsed stacking sites with W atom over W atom; BR (marked in green) means the bridge that connects neighboring AA sites; B stands for Bernal stacking, including two inversed configurations with W atom over Se atom ($B^{W/Se}$) and Se atom over W atom ($B^{Se/W}$). The dI/dV spectra from the constant-height scanning tunneling spectroscopy (CH-STS) along high-symmetry directions AA-B-BR-B-AA are illustrated in Fig. 3.12(b). The most striking features are multiple sharp peaks around bias voltage V_{bias} = -1.15 V on B and BR sites [Fig. 3.12(b)]. As the dI/dV

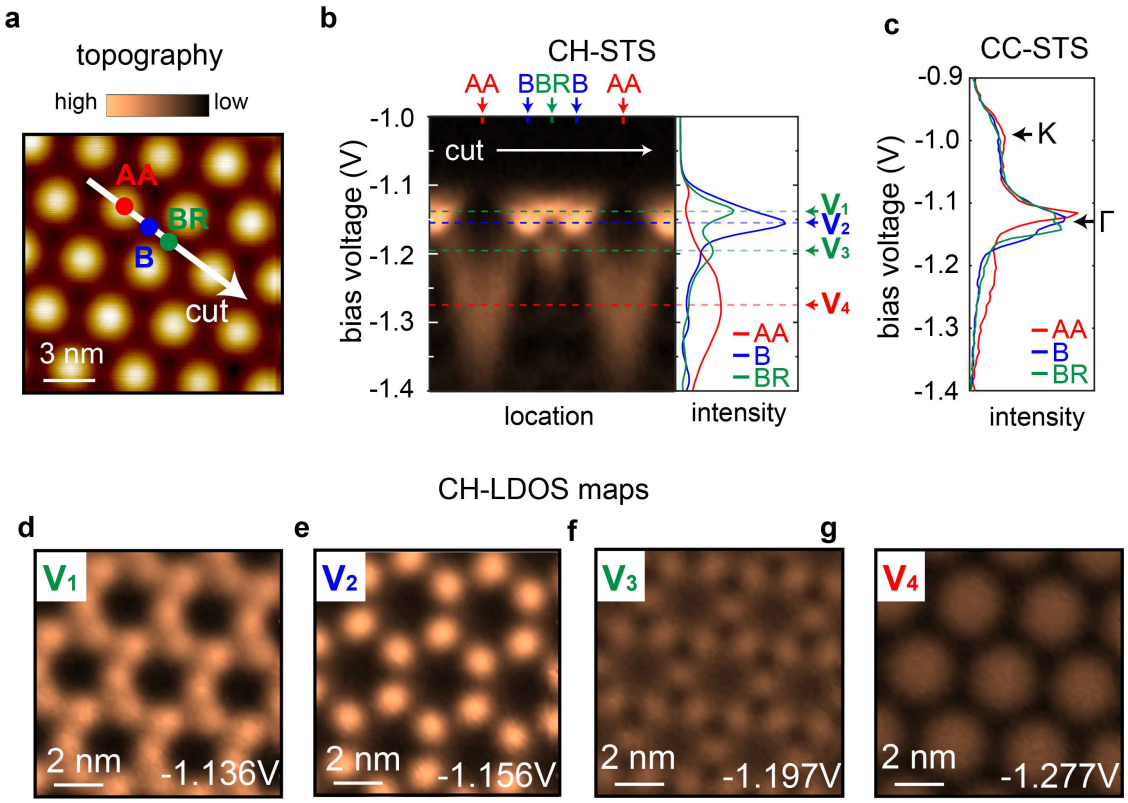

Figure 3.12: STM results on tbWSe$_2$. (a) Definition of high symmetry sites in tbWSe$_2$ superlattice. Here, AA (indicated by the red point) means eclipsed stacking sites with W atom over W atom; BR (indicated by the green point) means the bridge that connects neighboring AA sites; B (indicated by the blue point) stands for Bernal stacking, including two inversed configurations with W atom over Se atom ($B_{W/Se}$) or Se atom over W atom ($B_{Se/W}$). The white arrow indicates the direction of dI/dV spectra shown in (b). (b) Left: dI/dV spectra measured in constant height mode (CH-STS) along AA-B-BR-B-AA direction. The positions of AA, B, BR sites are indicated by arrows of corresponding colors. Right: representative dI/dV curves on AA (red), B (blue) and BR (green) sites. The peak positions in AA (V_4), B (V_2) and BR (V_1, V_3) curves are marked by dashed lines of corresponding colors. (c) dI/dV curves measured in constant current mode (CC-STS) on AA, B and BR sites. Black arrows indicate dI/dV signal contributed by Γ- and K-valleys, respectively. (d)-(g) LDOS maps (in CH mode) corresponding to the peak positions in the AA (V_4), B (V_2) and BR (V_1, V_3) curves, respectively. During the LDOS mapping, the tip height was adjusted at V_{bias}= -1.6 V with I = 170 pA.

signal decays exponentially with the increase of in-plane momentum of the tunneling electrons, the observation of such sharp peaks in CH-STS indicates the existence of flat moiré bands in the vicinity of the BZ center [92]. To further check the result, STS measurement in constant-current mode (CC-STS) was performed, which is more sensitive to tunneling electrons from the K valleys [92, 93]. Prominent dI/dV peaks, with same range of the V_{bias} as CH-STS [Fig. 3.12(b)], are observed on all

high-symmetry sites in CC-STS [Fig. 3.12(c)]. On the other hand, no obvious sign of flat band is observed around V_{bias} = -1.0 V, which is equivalent to the binding energy of the K-valley top. Therefore, we conclude the dI/dV peaks in CH-STS presents the fine structure of the Γ-valley moiré bands.

Next, the charge distribution corresponding to the dI/dV peaks were further investigated by mapping out local density of states (LDOS) in the real space from CH-STS. LDOS maps at the V_{bias} of peaks in AA (V4, Fig. 3.12(g)) and B (V2, Fig. 3.12(e)) sites both present honeycomb patterns, complying with a D6 symmetry at the moiré length scale instead of the D_3 symmetry of the tbWSe_2 moiré superlattice. It is a result of the emergent D_6 symmetry of moiré potential, as the z to -z (the out-of-plane direction) reflection in lattice structure does not affect the overall moiré potential of a bilayer system [67], supported by the qualitatively identical dI/dV spectra on the neighboring B sites with inversed configurations [Fig. 3.12(b)]. More interestingly, LDOS maps at the V_{bias} of peaks in BR site (V_1, Fig. 3.12(d) and V_3, Fig. 3.12(f)) present kagome patterns. According to the continuum theory [67], the emergence of kagome lattice in twisted TMDs is related with the sd_2 hybridization of moiré orbitals on Bernal stacking regions, which move the Wannier centers from neighboring B sites to the middle point (BR site), and effectively turn the honeycomb model into the kagome model.

The full evolution of LDOS maps is presented in Fig. 3.13. The charge distribution first evolves (∼30 mV below the Γ-valley edge) into the kagome pattern and keeps for ∼10 mV. Then it quickly changes (within 10 mV) into the honeycomb pattern and keeps for ∼20 mV. After ∼10 mV transition, the second kagome pattern appears and keeps for ∼15 mV. Then the charge distribution experiences a complex evolution and finally evolves into another honeycomb pattern. The sharp dI/dV peaks and the drastic change of LDOS patterns in millivolt scale indicate the tiny band width that is favorable for hosting strongly correlated phases. Besides, these peaks are associated with honeycomb- and kagome-shaped charge distribution in the moiré superlattice, which indicate the Γ-valley moiré bands can be effectively described with a honeycomb or kagome model at the moiré length scale. As the

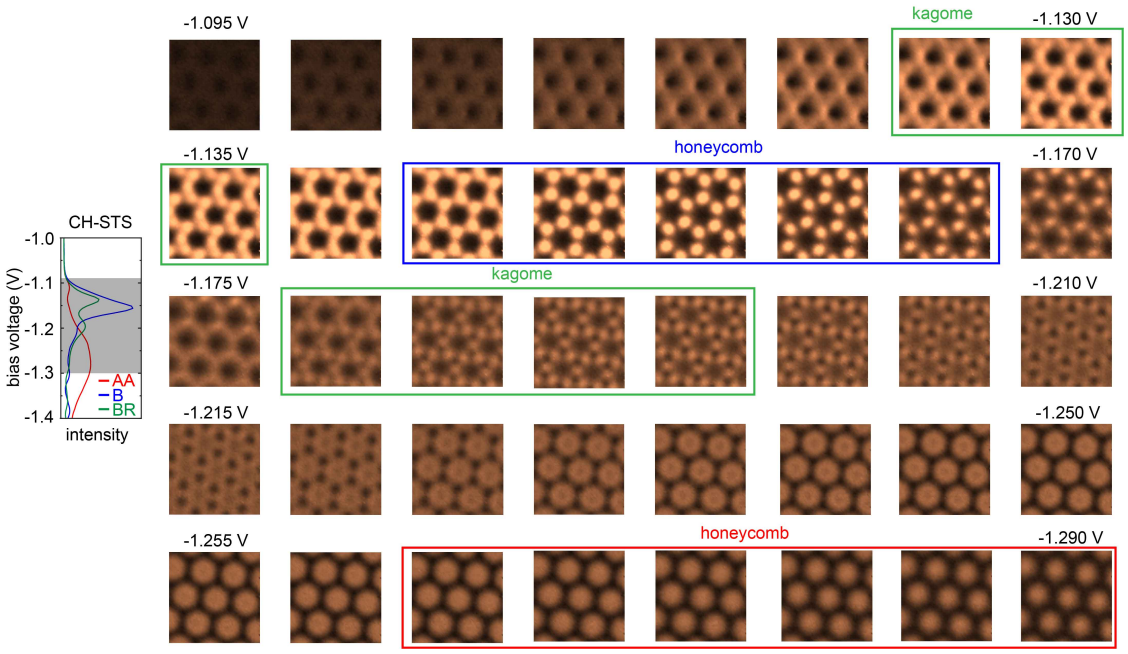

Figure 3.13: Evolution of LDOS maps. Left: CH-STS measured at AA (red), B (blue) and BR (green) sites. The gray area shows the bias voltage range shown in the right panel. Right: from top-left to bottom-right, the evolution of LDOS maps as V_{bias} changes from -1.095 V to -1.290 V with a step size of 5 mV. LDOS maps around the peaks in CH-STS are highlighted by the squares of corresponding colors.

size of the emergent lattice and the interaction strength can be tuned by external conditions (e.g., twist angle and gate voltage), the Γ-valley moiré bands can serve as a platform to realize highly controllable honeycomb and kagome models.

3.5 Calculation on twisted bilayer WSe_2

To further understand the intriguing moiré bands, tight-binding and first-principles calculation on 5.09° tbWSe_2 were performed [Fig. 3.14]. Notations of high symmetry points in the mini-BZ of tbWSe_2 superlattice are demonstrated in Fig. 3.14(a). Figures 3.14(c) and (e) show the band structures of intrinsic and twisted bilayer WSe_2 calculated by this tight-binding model, respectively, which are qualitatively consistent with the DFT results [Figs. 3.14(b) and (d)].

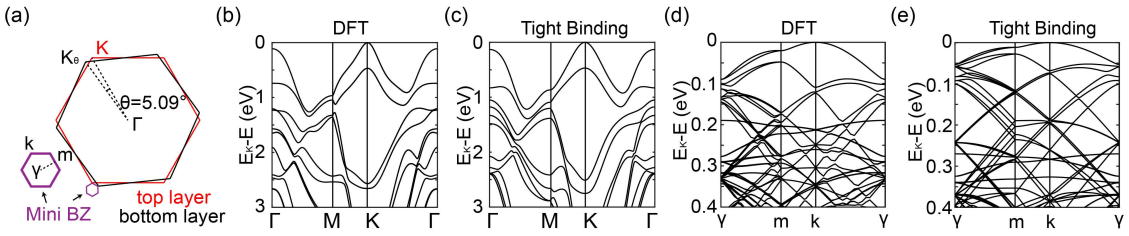

Figure 3.14: Calculation results on tbWSe$_2$. (a) Definitions of high-symmetry points used in calculation. (b)-(c), The band structure of intrinsic bilayer WSe_2 calculated by DFT and tight binding, respectively. (d)-(e), The band structure of tbWSe$_2$ ($\theta = 5.09°$) calculated by DFT and tight binding, respectively. The effect of SOC is included in all calculations.

3.5.1 Comparison between tight-binding calculation with ARPES results

Unfolding method based on the tight-binding model was performed to simulate the ARPES results [Fig. 3.15]. Unfolding process can be simply understood as the projection of calculated moiré wave functions onto the monolayer WSe_2 wave functions, which can simulate the weighted (based on the projection) moiré bands in the original BZ [90, 94]. According to the geometric relationship between the mini-BZ and original BZ, the equivalence path in both reference systems can be determined [Fig. 3.15(a)]. For example, the band dispersion along Γ-M direction in the original BZ is equivalent to that of γ-k-m-k-γ direction in the mini-BZ. In the folded band structure [Fig. 3.15(b), left part], a group of flat bands around binding energy 0.25 eV (highlighted in red) seemingly entangles with other moiré bands; while in the unfolded band structure [Fig. 3.15(b), right part], we can immediately find these flat bands are the top-most Γ-valley moiré bands.

The comparison between ARPES and simulation results on the Γ valley is presented in Fig. 3.16. In the simulated band dispersion [Fig. 3.16(c)], the most prominent features are three pairs of mini-bands converge at the Γ point $\sim$ 0.1 eV below the band top. ARPES results along K-Γ-K and M-Γ-M directions [Figs. 3.16(a)(b)] both catch these features, though only two bands crossing at the Γ point can be distinguished. The simulation result predict a band gap opening along Γ-M direction around the band top, the size of which is $\sim$20 meV, though

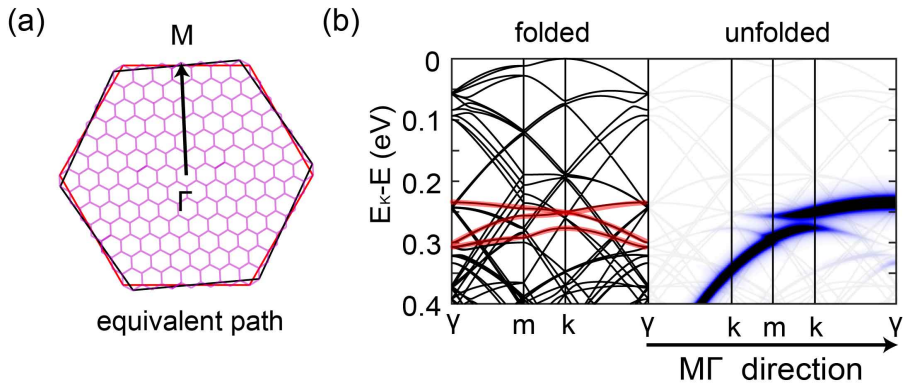

Figure 3.15: Unfolding process. (a) Illustration of the geometric relationship between original BZs and mini-BZ. (b) Folded (presented in the mini-BZ) and unfolded (presented in the original BZ) calculation results based on the tight binding model. The top-three Γ-valley moiré bands are highted in red. The black semi-transparent backgroud in the unfolded result shows the moiré bands in the equivalent path in the mini-BZ.

this feature is not resolved in our result as the energy resolution of nano-ARPES (usually > 50 meV) is insufficient. The simulation result shows diminished intensity of moiré bands between 0.5-0.8 eV, though ARPES results present distinguishable moiré bands in the corresponding energy range.

The ARPES and calculation results on $tbWSe_2$ are barely consistent. Here we list some possible reasons: 1. The interlayer hybridization of $tbWSe_2$ is largely related to the degree of lattice relaxation, which depends on the sample temperature, though all calculation is based on the 0 K model while nano-ARPES is usually performed around 100 K. 2. The current nano-ARPES technique makes compromise in the temperature control and the energy resolution to guarantee a stable sample position during the measurement, which can hardly resolve fine features of moiré bands. In the future work, we will establish the thermal dynamic models on $tbWSe_2$ to compare with laser-based nano-ARPES result, aiming to get a quantitative correspondence between ARPES and calculation.

3.5.2 Comparison between first-principles calculation with STM results

Figure 3.17 presents the calculated charge distribution from the Γ-valley edge to the third Γ-valley moiré band. Here, e_1, e_3 and e_4 are the binding energies of the top-

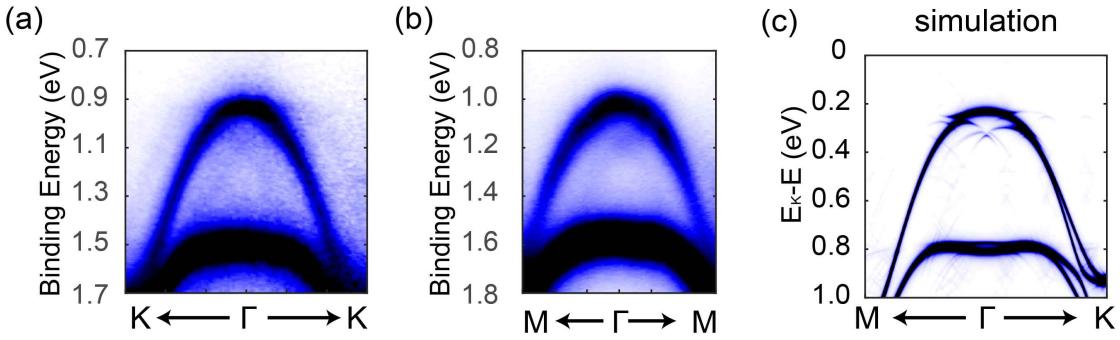

Figure 3.16: ARPES vs calculation. (a) Band dispersion along K-Γ-K direction. (b) Band dispersion along M-Γ-M direction. (c) Simulated band dispersion along M-Γ-K direction.

three Γ-valley moiré bands at the γ point. e_2 is the binding energy of the crossing point of the top-two Γ-valley moiré bands. The evolution of calculated charge distribution is qualitatively consistent with that of LDOS maps, which confirms that the honeycomb and kagome quantum models are intrinsic properties of the Γ-valley moiré bands. Quantitatively speaking, the DFT calculation overestimates the energy difference between e_1 and e_2, which suggests that the crossing formed by the top-two Γ-valley moiré bands have symmetric upper and lower branches and can be analogized to the Dirac cone in the mini-BZ. On the other hand, the DFT calculation underestimates the energy difference between e_3 and e_4, which suggests honeycomb and kagome models in $tbWSe_2$ can be well-distinguished by tuning the chemical potential.

3.6 Summary

In this work, we performed a systematic investigation on the electronic structure of 5.1° $tbWSe_2$. By using angle-resolved photoemission spectroscopy with sub-micron spatial resolution (μ-ARPES), electronic structures of both the Γ and K valleys were directly visualized. While no obvious sign of flat bands around K valley is observed, replica-like moiré bands around the Γ valley are clearly presented. Further scanning tunneling microscopy/spectroscopy (STM/STS) measurement revealed the corresponding real space charge distribution of the Γ-valley moiré bands, which

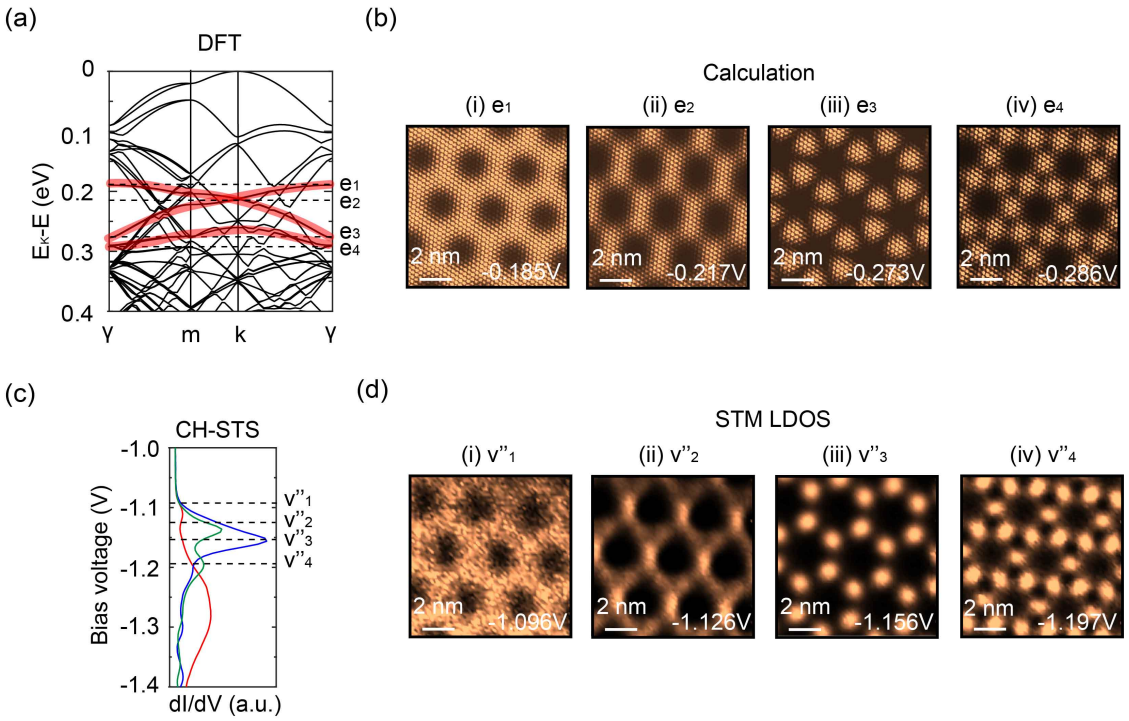

Figure 3.17: STM vs calculation. (a) The band structure of tbWSe$_2$ ($\theta = 5.09°$) calculated by DFT. The top-most three Γ-valley moiré bands are highted in red (b) Calculated charge distributions corresponding to (i)-(v) e$_1$-e$_4$. (c) CH-STS. (d) LODS maps at V_{bias} (i)-(v) v"$_1$-v"$_4$. The intensity in the calculated charge distributions and the LDOS maps has been normalized for the better comparison.

reflects the honeycomb and kagome shape in the moiré superlattice. The essence of physics is well captured by our first-principles and tight-binding model calculations.

The absence of the K valley flat bands in both our ARPES and STM/STS results, seems rather anomalous, especially when the Γ valley moiré bands are clearly observed. One possible explanation is the different orbital components of different valleys. The K valleys are contributed by orbitals with in-plane orientation (metal d_{xy}, $d_{x^2-y^2}$/chalcogen p_x, p_y orbitals) and weakly interacted with each other due to the small overlap of wavefunction and interlayer hopping (compared with Γ valley, which consists of metal d_{z^2} and chalcogen p_z orbitals). Indeed, the continuum theory predicts the moiré potential in K-valley model is less than one-fifth of that in Γ-valley model [67, 72, 74]. Such weak interaction may explain the disappearance of the K-valley moiré bands. Displacement field, which always accompanies the observation of strongly correlated phases in twisted TMDs, could be the key factor

for the formation of K-valley moiré bands due to the enhanced interlayer hopping [54, 69, 70]. 3D lattice reconstruction observed in recent STM measurements on WSe_2/WS_2 bilayer, which alters the overlapping of in-plane orbitals, could also affect the K-valley electronic structure [91].

On the other hand, the Γ-valley moiré bands, which originate from the variation of out-of-plane orbitals in moiré superlattice, are straightforwardly attainable. The sharp dI/dV peaks and the drastic change of LDOS patterns in millivolt scale indicate the tiny band width that is favorable for hosting strongly correlated phases. Besides, these peaks are associated with honeycomb- and kagome-shaped charge distribution in the moiré superlattice, which indicate the Γ-valley moiré bands can be effectively described with a honeycomb or kagome model at the moiré length scale [68]. As the size of the emergent lattice and the interaction strength can be tuned by external conditions (e.g., twist angle and gate voltage), the Γ-valley moiré bands can serve as a platform to realize highly controllable honeycomb and kagome models [67, 95, 96]. This idea is feasible, as the majority of 2H-phase TMD homo-multilayers (e.g., WS_2, MoS_2 and $MoSe_2$)[80–82] and hetero-multilayers (e.g., MoS_2/WS_2 bilayer)[88] host the Γ point as the VBM, suggesting the Γ-valley moiré bands would contribute to the transport via electrostatic gating. Indeed, recent transport measurements on twisted double-bilayer WSe_2 whose VBM is at the Γ point, have already revealed the Γ-valley moiré bands can lead to strongly correlated phases [70].

In conclusion, our results reveal moiré potential in twisted TMDs has significant modification on the Γ-valley and demonstrate the Γ-valley moiré bands host the potential for simulating honeycomb and kagome models.

4

Umklapp sacttering in graphene-based heterostructures

Contents

In crystalline materials, Umklapp scattering describes the scattering process of electron or other quasiparticles, in which the total crystal momentum is not conserved [97]. This non-conservation results from the momentum exchange with the lattice. In this chapter, we will present ARPES study on graphene-based heterostructures, including twisted multilayer graphene and graphene/transition metal dichalcogenide (TMD) heterostructures, which presents multiple replica Dirac cones (rDCs) generated from Umklapp scattering [62, 66, 98–100]. More interestingly, we found 11° could be a 'magic angle' in graphene/TMD heterostructures, which can possibly lead to the formation of flat bands via the hybridization of second order rDCs.

4.1 Umklapp scattering

4.1.1 General description

A scattering process follows the conservation of total momentum ($\mathbf{p}$). As shown in a simple model [Fig. 4.1(a)], the scattering of two initial states with wave vectors pointing to the right must result in a final state with the wave vector pointing to the right. In crystalline materials, we usually use the crystal momentum ($\mathbf{k}$) instead of the real momentum to describe the states of electrons and other quasiparticles [97]. The scattering of quasiparticles in crystal usually involves the momentum exchange with the lattice. As a result, the conservation of total momentum should be described as

$$\mathbf{k_f} = \mathbf{k_i} + \mathbf{G} \tag{4.1}$$

where $\mathbf{k_f}$ and $\mathbf{k_i}$ are the total crystal momentums of initial and final states of quasiparticles, $\mathbf{G}$ is an arbitrary reciprocal lattice vector. When $\mathbf{G}$ is $\mathbf{0}$, the scattering of quasiparticles appears as the normal scattering process [Fig. 4.1(a)]; when $\mathbf{G}$ is non-zero, the scattering of quasiparticles appears as the Umklapp scattering process [Fig. 4.1(b)], in which, due to the equivalence of the first Brillouin zone (BZ) and other BZs, the final state $\mathbf{k_f}$ in other BZs can be mathematically transformed to a point inside the first BZ. This transformation has been confirmed as a real scattering process, which is the dominant contributor to the thermal

resistivity at high temperatures and the electrical resistivity at low temperatures for low defect crystals [97].

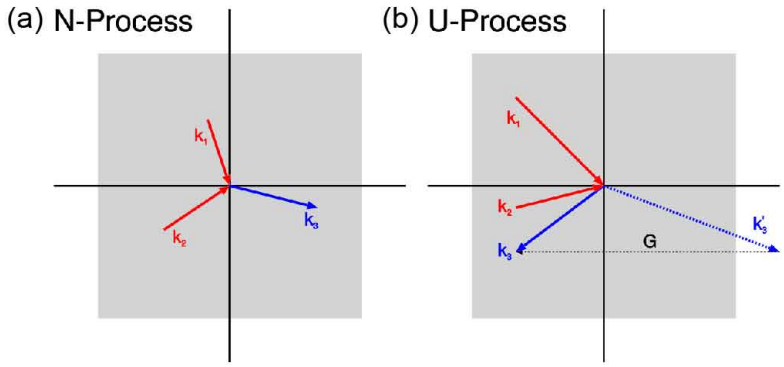

Figure 4.1: Normal and Umklapp scattering. (a) Illustration of normal scattering process (N-process). (b) Illustration of Umklapp scattering process (U-process). In (a) and (b), red and blue arrows stand for the wave vectors of initial and final states, respectively. This figure is adapted from [97].

4.1.2 Umklapp scattering in competing periodicities

The electronic band theory is based on the periodicity of crystal structure, where electronic states can be described by two well-defined quantum numbers, the binding energy E and the crystal momentum $\mathbf{k}$. However, in systems with two competing periodicities, such as 2D heterostructures, the crystal momentum $\mathbf{k}$ of a single layer is no longer a good quantum number due to the lack of overall translation symmetry [63–65, 101, 102]. In a commensurate heterostructure, the periodicity can be re-defined in the moiré superlattice, which gives rise to a new E-$\mathbf{k}$ relation in the mini-BZ [49]. In an incommensurate heterostructure, though the band structure cannot be defined due to the invalidity of crystal momentum, the quasi-band-structure can be obtained by considering the interlayer coupling [63–65].

Here, we consider a two-layer heterostructure [63, 64]. The lattice positions of the top layer (L) and the bottom layer (L') are given by

$$\mathbf{R}_X = n_1\mathbf{a}_1 + n_2\mathbf{a}_2 + \mathbf{X} \tag{4.2}$$

$$\mathbf{R}_{X'} = n_1'\mathbf{a}'_1 + n_2'\mathbf{a}'_2 + \mathbf{X}' \tag{4.3}$$

where n_1,n_2,n'_1,n'_2 are integers, $\mathbf{a}_1$,$\mathbf{a}_2$ are lattice vectors for the top layer, $\mathbf{a'}_1$,$\mathbf{a'}_2$ are lattice vectors for the bottom layer, $\mathbf{X}$ and $\mathbf{X'}$ are the sublattice positions inside the unit cell, which can have both in-plane and out-of-plane components. Thus, the reciprocal lattice vector of both layers can be defined as:

$$\mathbf{a}_i \cdot \mathbf{G}_j = \mathbf{a'}_i \cdot \mathbf{G'}_j = 2\pi\delta_{ij} \tag{4.4}$$

Define $|\mathbf{R}_X\rangle$=$\Phi_x(\mathbf{r} - \mathbf{R}_X)$ as the atomic state of the sublattice X localized at $\mathbf{R}_X$. The atomic orbital Φ_x may be different depending on X. Assume that the transfer integral from the site $\mathbf{R}_X$ to $\mathbf{R'}_X$ can be written as $-T_{X'X}(\mathbf{R'}_X - \mathbf{R}_X)$. The interlayer Hamiltonian to couple the top and bottom layers is then written as:

$$U = -\sum_{X,X'} -T_{X'X}(\mathbf{R'}_X - \mathbf{R}_X)\,|\mathbf{R'}_X\rangle\,\langle\mathbf{R}_X| + h.c. \tag{4.5}$$

Constructing such Hamiltonian in the real space is nearly impossible due to the large size of superlattice, as it requires the relative inter-atom position for every single combination of the atomic sites in both layers. On the other hand, the interlayer coupling can be described in a simpler manner in the reciprocal space, if we use the Bloch basis to define the electronic states in each layer:

$$|\mathbf{k}, X\rangle = \frac{1}{\sqrt{N}}\sum_{\mathbf{R}_X} e^{i\mathbf{k}\cdot\mathbf{R}_X}\,|\mathbf{R}_X\rangle \tag{4.6}$$

$$|\mathbf{k'}, X'\rangle = \frac{1}{\sqrt{N'}}\sum_{\mathbf{R'}_X} e^{i\mathbf{k'}\cdot\mathbf{R'}_X}\,|\mathbf{R'}_X\rangle \tag{4.7}$$

where $\mathbf{k}$ and $\mathbf{k'}$ are the 2D Bloch wave vectors parallel to the layer, N and N' are the numbers of unit cells of the top and bottom layers. Here, we assume that N=N' in the same area though the top and bottom layers are incommensurate. Then the interlayer Hamiltonian is written as:

$$\begin{aligned} U_{X,X'}(\mathbf{k'}, \mathbf{k}) &= \langle\mathbf{k'}, X'|U|\mathbf{k}, X\rangle \\ &= -\sum_{\mathbf{G},\mathbf{G'}} t_{X'X}(\mathbf{k}+\mathbf{G})e^{-i\mathbf{G}\cdot\mathbf{X}+i\mathbf{G'}\cdot\mathbf{X'}}\delta_{\mathbf{k}+\mathbf{G},\mathbf{k'}+\mathbf{G'}} \end{aligned} \tag{4.8}$$

Here, $t_{X'X}(\mathbf{k}+\mathbf{G})$ is the in-plane Fourier transform of the transfer integral $T_{X'X}$. According to the equation (4.8), the interlayer coupling term is non-zero only when the generalized Umklapp condition is satisfied.

$$\mathbf{k} + \mathbf{G} = \mathbf{k'} + \mathbf{G'} \tag{4.9}$$

From the perspective of scattering, the equation (4.8) and the generalized Umklapp condition indicate that the initial state $\mathbf{k_i}$ can be scattered to the final state $\mathbf{k_f} = \mathbf{k_i}+\mathbf{G}\text{-}\mathbf{G}'$ with a possibility related with $t_{X'X}$. This scattering process has been observed in graphene-based heterostructures with competing periodicities [62, 66], which presents multiple rDCs inside the first BZ (as shown in Fig. 2.7). Here, we illustrate how these rDCs are generated.

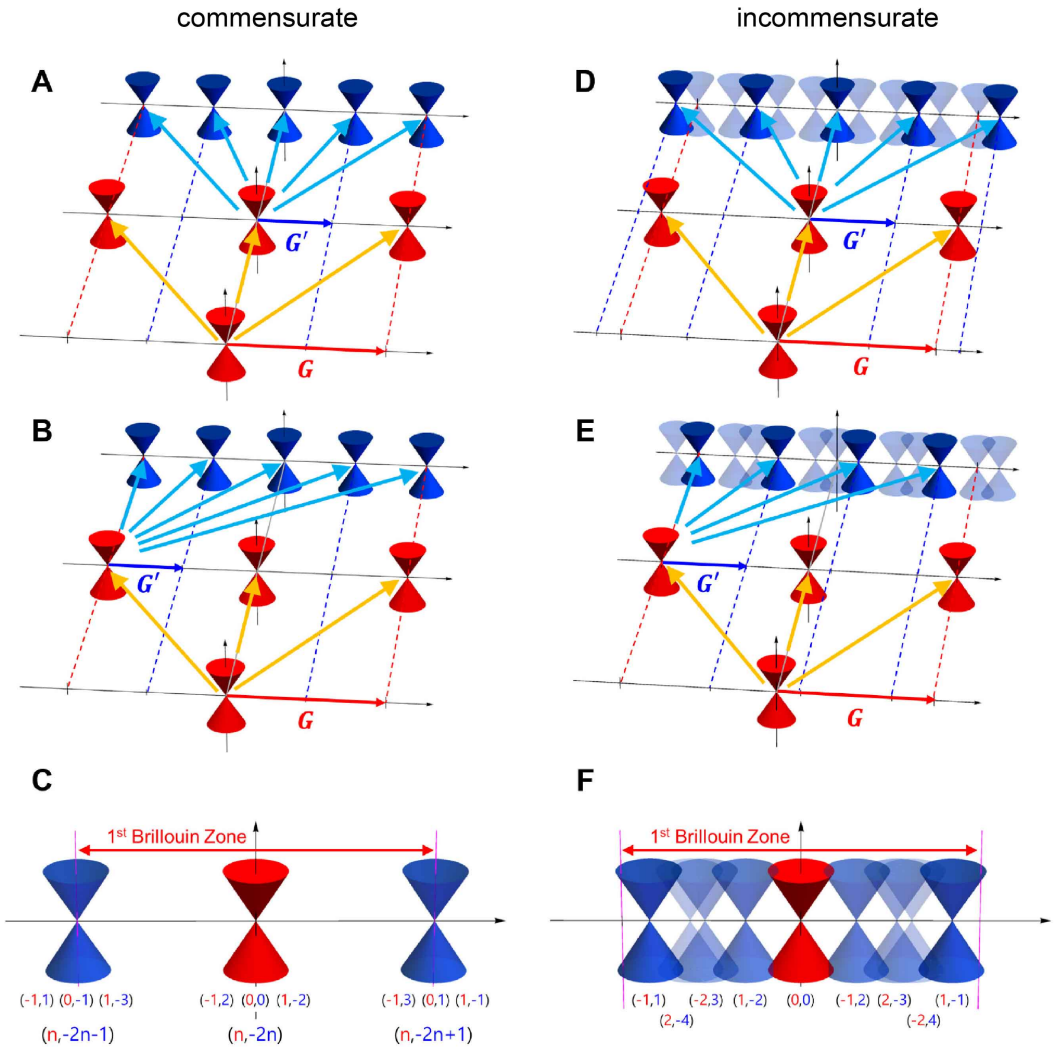

Figure 4.2: Umklapp scattering in 1D periodic order.(a)-(c) Umklapp scattering in 1D commensurate order. In this case, the original reciprocal vector **G** is twice as the competing reciprocal vector **G′**. (d)-(e) Umklapp scattering in 1D quasiperiodic order, where **G** and **G′** are incommensurate to each other. (a) and (c) present Umklapp scattering of the DC in the first BZ. (b) and (d) present Umklapp scattering of the DC in the second BZ. (c) and (e) present of the resulting rDCs in the first BZ, including high order Umklapp scattering. This figure is adapted from [62].

We first consider a 1D periodic hetero-chain [Figs. 4.2(a)-(c)] composed of two commensurate chains (L and L') [62], whose reciprocal vectors are $\mathbf{G_1} = 2\mathbf{G'_1}$. If there is a DC at the center of the 1D BZ of chain L, the original periodicity of chain L will result in the DCs in the centers of other BZs. The competing periodicity from chain L' will further scatter the DCs by $\mathbf{G'} = n\mathbf{G'_1}$, leading to the rDCs at the boundary of the BZ of chain L. Therefore, in the first BZ of chain L, we can observe 3 DCs in total, though all these DCs are actually contributed by multiple scattering process. In the incommensurate cases [Figs. 4.2(d)-(f)], the scattering by the competing periodicity is much more complicated as the scattering from different BZs of chain L will lead to different positions of rDCs. In principle, we should observe numerous rDCs in the first BZ. However, the interlayer transfer integral $t_{X'X}$ for high order scattering is exponentially low, so that high order rDCs are barely observed.

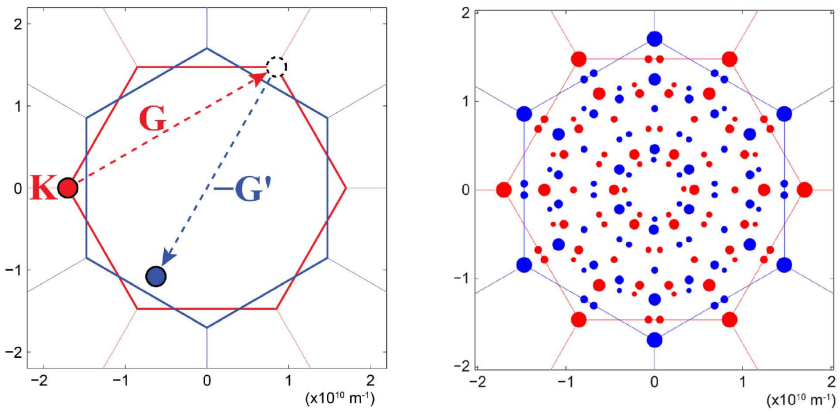

Figure 4.3: Umklapp scattering in graphene quasicrystal. Left: an example of the first order Umklapp scattering. The orginal DC (red spot) is first scattered by the orginal vector G (red dashed arrow) to another K point of the same layer, then scattered by the competing vector -G (blue dashed arrow) to the position inside the first BZ (blue spot). Right: Illustration of rDCs from the high order Umklapp scattering. This figure is adapted from [62].

Then we consider Umklapp scattering in twisted bilayer graphene [Figs. 4.3] [62]. The 30° bilayer graphene (also known as the graphene quasicrystal) is an incommensurate system where the electronic structure cannot be defined on the moiré basis. According to the generalized Umklapp condition, the first order Umklapp scattering, $\mathbf{k'}$ - $\mathbf{k}$ = $\mathbf{G_1}$ - $\mathbf{G'_1}$, will bring the electronic states at the K point of layer 1 (red) to K + $\mathbf{G_1}$ - $\mathbf{G'_1}$, which is the mirror position (with respect

to the M point of layer 2 (blue)) of the K' point of layer 1. Thus, if the Umklapp scattering exists, we expect to observe mirrored rDCs inside the first BZ. If we take the high order Umklapp scattering into consideration, the rDCs can form a dodecagonal pattern from the boundary to the center of the first BZ.

We should notice, the interlayer coupling described in term of Umklapp condition, and the moiré potential have the same physical nature. Under the commensurate condition, the moiré vector of mini-BZ can be defined as $\mathbf{G_1}$ - $\mathbf{G'_1}$, so that the 'moiré picture' can always be translated into the 'Umklapp picture'. However, under the incommensurate condition, the moiré periodicity is not well-defined, and we must use the Umklapp scattering to describe the additional electronic structures resulted from interlayer coupling. In other word, the rDCs from Umklapp scattering, and the rDCs from the moiré periodicity are the same electronic states modified by the same competing order in the heterostructure. In following subsections, we will not distinguish these two concepts.

4.2 ARPES study on twisted graphene with large twist angles

Previous ARPES studies on 30° bilayer graphene on SiC (0001) and Pt (111) surfaces have demonstrated the existence of Umklapp-scattering-induced rDCs [62, 66]. Here, we present the ARPES study on twisted multilayer graphene with different large twist angles (30° trilayer and 33° bilayer). In both cases the first order Umklapp scattering (mirrored rDCs) has been observed, which indicate Umklapp scattering can happen regardless of the twist angle and the number of layers.

The twisted graphene samples were chemically grown on the (111) surface of Cu single crystals, details about which are available in ref. [103]. The nano-ARPES measurements were performed at the SpectroMicroscopy beamline of Elettra with 74 eV photons. The simulation results were generated based on the generalized Umklapp condition.

Figure 4.4 presents the ARPES results on 30° trilayer graphene. The twist angle can be directly determined in the constant energy contour (CEC) at E_B =

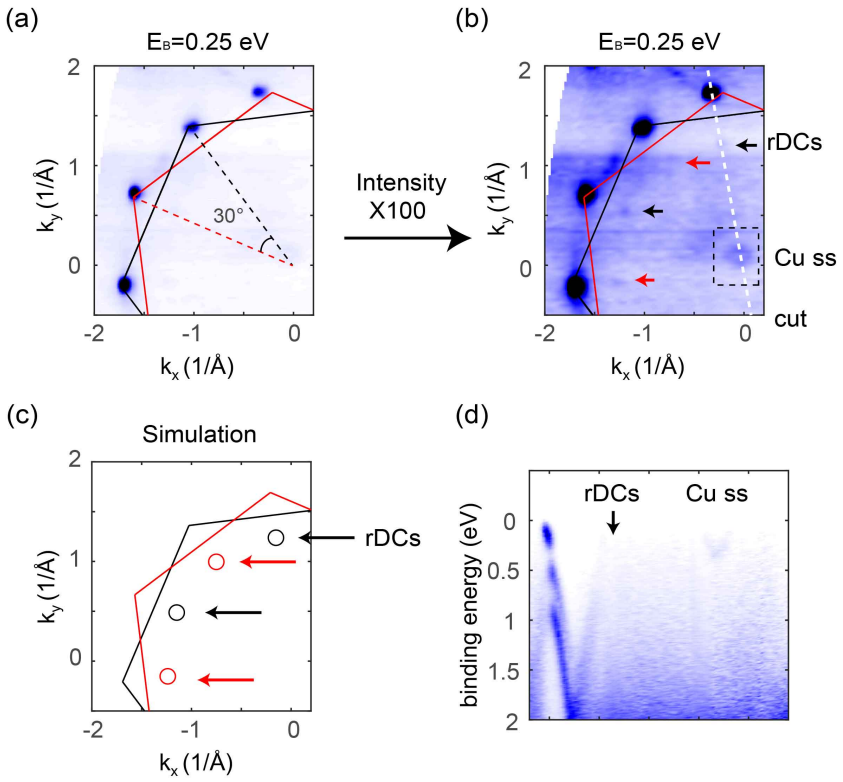

Figure 4.4: Replica Dirac cones in 30° twisted trilayer graphene. (a)(b) CECs at $E_B = 0.25$ eV to show the rDCs. Red and black lines stand for BZs of different layers. The twist angle between BZs is 30°. White dashed line shows the cut direction in (d). The surface states of Cu (111) are highlighted by the black dashed rectangle. (c) Simulation results of the first order Umklapp scattering in 30° twisted bilayer graphene. (d) Cut to show the original, replica bands of graphene, and the surface states of Cu (111). In (b) and (c), rDCs from different layers are indicated by red and black arrows, respectively.

0.25 eV [Fig. 4.4(a)], which presents two sets of nodes with an angle separation of 30°. With the intensity multiplied by 100 [Fig. 4.4(b)], the CEC presents more details. A pocket with weak intensity is observed around the BZ center, which can be attributed to the surface states of Cu (111). Signatures of the Cu bulk states are observed around the original electronic structure of twisted trilayer graphene. Prominently, weak nodal-like features are found inside the first BZ, the positions of which are the same as simulation results on the first order Umklapp scattering [Fig. 4.4(c)]. In the band dispersion along Γ-K [Fig. 4.4(d)], we can observe a K valley of a bilayer graphene, a rDC of monolayer graphene, and the surface states of Cu(111) in the sequence from K to Γ. The fact that rDC at the mirror position (with respect to the M point) differs from the original bilayer band structure confirms

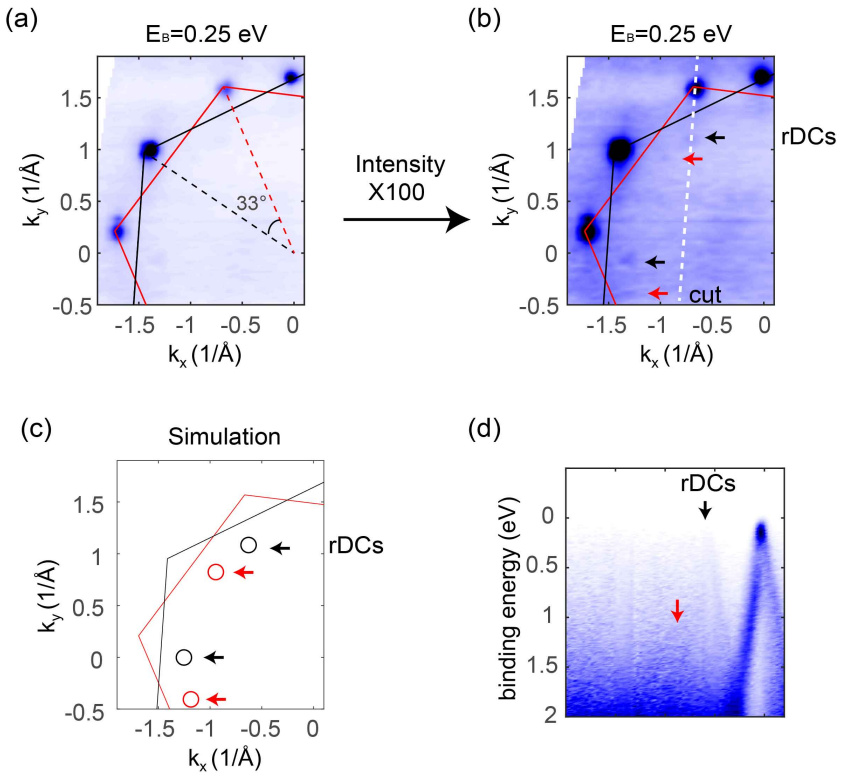

Figure 4.5: Replica Dirac cones in 33° twisted bilayer graphene. (a)(b) CECs at $E_B = 0.25$ eV to show the rDCs. Red and black lines stand for BZs of different layers. The twist angle between BZs is 33°. White dashed line shows the cut direction in (d). (c) Simulation results of the first order Umklapp scattering in 33° twisted bilayer graphene. (d) Cut to show the original and replica bands. In (b)-(d), rDCs from different layers are indicated by red and black arrows, respectively.

the origin of Umklapp scattering. The observation of two sets of replica nodes demonstrates that electronic states in both monolayer and bilayer graphene can be Umklapp scattered. Moreover, the 33° bilayer graphene also hosts rDCs in the first BZ [Fig. 4.5], indicating Umklapp scattering is a universal process in large angle twisted graphene regardless of the twist angle.

4.3 ARPES study on graphene/TMD heterostructures

4.3.1 Magic angle in graphene/TMD heterostructures

Umklapp scattering can also happen in heterostructures of graphene and TMDs [100]. As the reciprocal vectors of graphene and TMDs are different in the magnitude

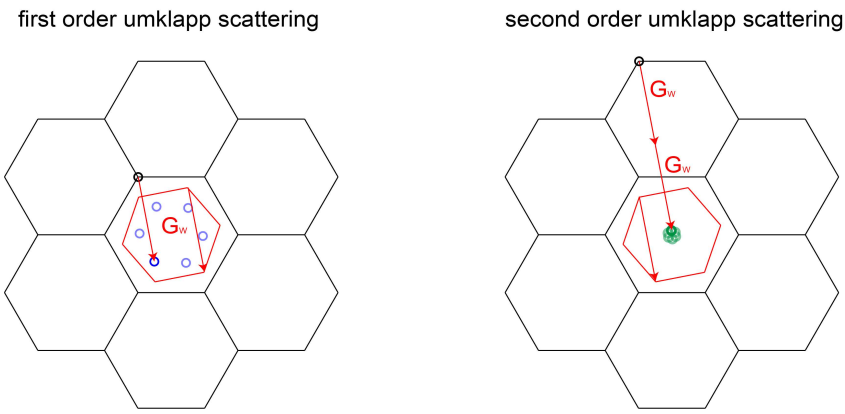

Figure 4.6: Umklapp process in graphene/WSe_2 heterostructures. Red and black hexagons stand for the BZ of WSe_2 and graphene, respectively. Black, blue, green circles stand for the orginal DCs, the first order rDCs, the second order rDCs, respectively. Red arrows stand for the reciprocal vectors of WSe_2, by which the orginal DCs can be scattered into the first BZ of WSe_2.

(graphene, 2.95 $Å^{-1}$; TMD, e.g., WSe_2, 2.20$Å^{-1}$), the low order (the first or the second order) Umklapp scattering could result in rDCs near the BZ center. Considering the graphene/WSe_2 heterostructure [Fig. 4.6, here the twist angle is 11°], the competing periodicity can bring the DCs of the first BZ of graphene (black circle) into the first BZ of WSe_2 (blue circles) via a reciprocal vector of WSe_2 ($\mathbf{G_W}$, red arrows), which is known as the first order Umklapp scattering. It can further generate rDCs near the BZ center (green circles), by scattering the DCs of the second BZ of graphene with $2{\cdot}\mathbf{G_W}$, which is known as the second order Umklapp scattering.

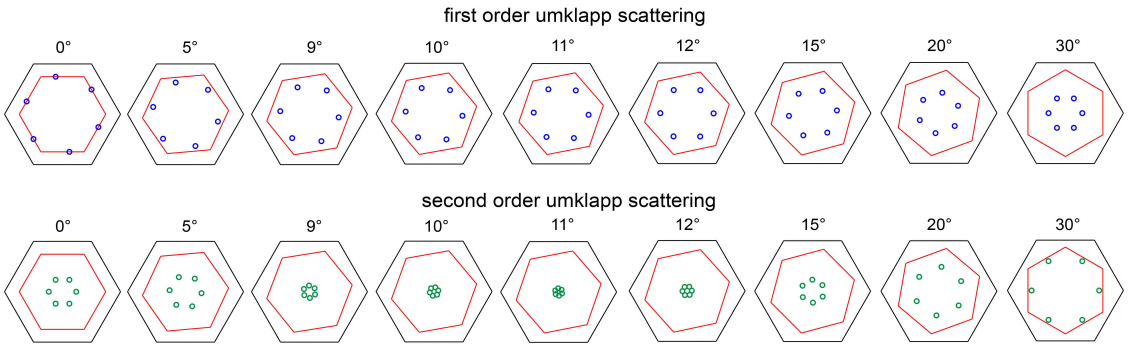

Figure 4.7: Evolution of positions of replica Dirac cones in graphene/WSe_2 heterostructures. The top row shows the evolution of rDCs from the first order Umklapp scattering with the twist angles. The bottom row shows the evolution of rDCs from the first order Umklapp scattering with the twist angles.

Consider the momentum separation between rDCs that are closest to the BZ

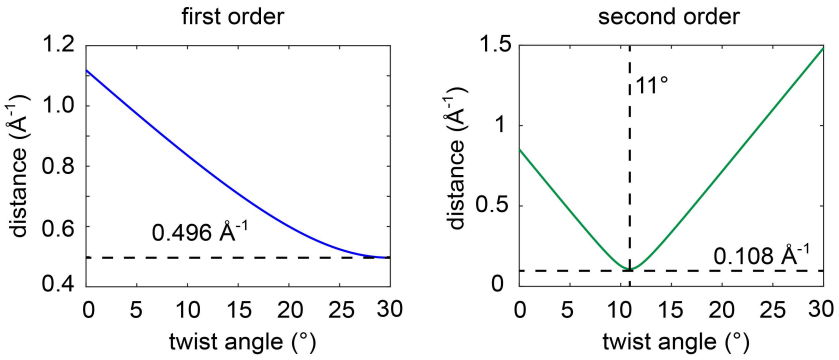

Figure 4.8: Momentum spacing between replica Dirac cones.

center. The first order Umklapp scattering monotonically 'compresses' rDCs into a smaller momentum area as the twist angle increases [Fig. 4.7]. The minimum momentum separation between two neighboring first order rDCs is 0.496 $Å^{-1}$ at 30° [Fig. 4.8] . On the other hand, the second order Umklapp scattering leads to a minimum momentum separation of 0.108 $Å^{-1}$ between the nearest second order rDCs at 11°, which I would call a 'magic angle' in the graphene/TMD heterostructure.

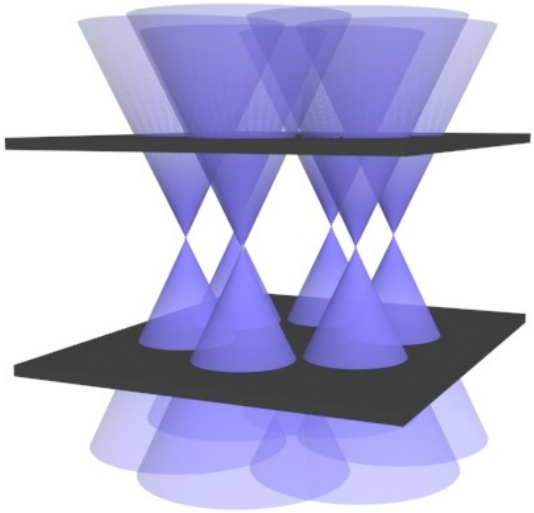

Figure 4.9: Umklapp scattering induced flat band. The blue cones stand for the rDCs. The balck sheets stand for the possiple flat bands formed by the hybridization of rDCs.

11° is a magic angle for ARPES experiment, as the resulting small momentum of rDCs (< 0.15 $Å^{-1}$) enables the laser ARPES measurement, whose measurable momentum range is limited in 0.2 $Å^{-1}$ (for 7 eV laser). Currently, all ARPES results

on graphene-based system are obtained from the helium-lamp-based or synchrotron-based ARPES setup [62, 66, 98–100], limited in the energy and momentum resolution. Laser ARPES measurements on rDCs are expected to present delicate structures of the original DCs, and can be used to investigate the moiré flat band in the magic angle twisted bilayer graphene, by studying the electronic structure of a trilayer heterostructure composed of a bilayer graphene and a monolayer TMD.

11° is non-trivial also because rDCs are artificially squeezed into a tiny hexagon, which is comparable to the mini-BZ of a moiré superlattice (the momentum separation 0.108 $Å^{-1}$ is equivalent to a moiré length of 3.8 nm). The flat band in twisted bilayer graphene results from the hybridization of two DCs with little momentum separation [49]. Similarly, if there is a strong hybridization among the rDCs, flat bands may emerge in the graphene/TMD heterostructure [Fig. 4.9].

4.3.2 Umklapp scattering in the graphene/monolayer WSe_2 heterostructure

To verify the above-mentioned scenario, we performed nano-ARPES measurements on graphene/WSe_2 heterostructures with 14° and 11° twist angles. The samples were fabricated by transferring monolayer WSe_2 onto monolayer graphene with a given twist angle. The nano-ARPES measurements were performed at ANTARES in SOLEIL and I05 in Diamond Light Source.

Figure 4.10 presents ARPES results on the 14° graphene/WSe_2 heterostructure. The good consistence between the optical image [Fig. 4.10(a)] and the ARPES spatial map [Fig. 4.10(b)] enables us to focus on the heterostructure area. The CEC at $E_B = 0.9$ eV [Fig. 4.10(c)] presents both K valleys of WSe_2 (marked by the red BZ) and graphene (marked by the black BZ), according to which a twist angle of around 14° can be determined. Prominently, pockets with weak intensity are observed inside the first BZ of WSe_2, indicating the existence of rDCs. (Currently, it is not clear what material parameters determine the photoemission intensity of rDCs.) The CEC at $E_B = 0.25$ eV [Fig. 4.10(d)] confirms that these additional pockets are the first order replica bands from graphene, as WSe_2 has no electronic

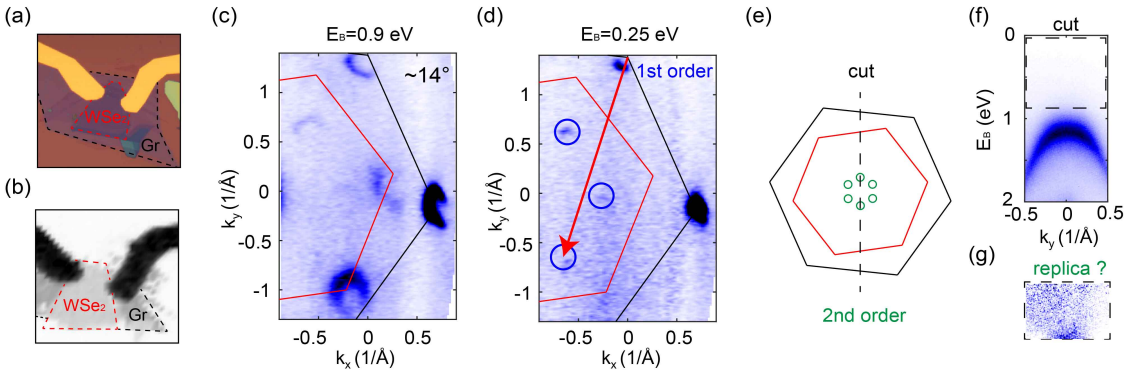

Figure 4.10: Replica Dirac cones in 14° graphene/WSe_2 heterostructure. (a) Optical image. (b) Spatial map. In (a) and (b), the WSe_2 and graphene regions are outlined by red and black dashed lines, respectively. (c) CEC at E_B=0.9 eV. (d) CEC at E_B=0.25 eV. (e) Simulation of the second order Umklapp scattering. (f) Cut across Γ, the direction of which is indicated by the black dashed line in (e). (g) Zoom-in view to show the signature of the second order rDCs. In (c)-(d) red and black lines stand for BZs of WSe_2 and graphene, respectively; blue and green circles stand for the first and the second order rDCs, respectively; the red arrow is the reciprocal vector of WSe_2.

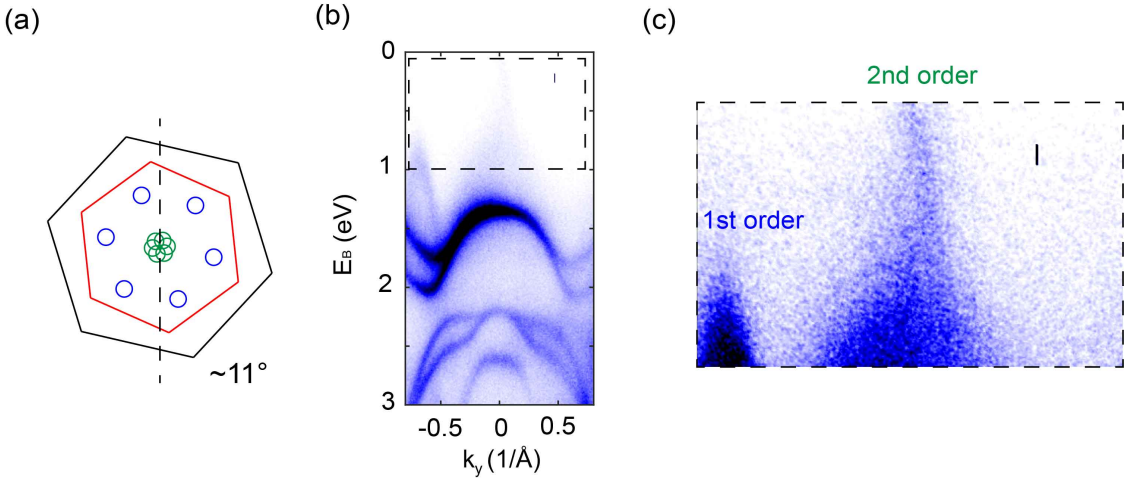

Figure 4.11: Replica Dirac cones in 11° graphene/WSe_2 heterostructure. (a) Simulation of the second order Umklapp scattering; red and black lines stand for BZs of WSe_2 and graphene, respectively; blue and green circles stand for the first and the second order rDCs, respectively. (b) Cut across Γ, the direction of which is indicated by the black dashed line in (a). (c) Zoom-in view to show the signature of the second order rDCs.

state at such binding energy. Figure 4.10(e) presents the simulation results of the second order Umklapp scattering, according to which two rDCs are expected to be observed in the cut across Γ point. Indeed, weak but distinguished photoemission intensity with line-shaped dispersion has been found above the Γ valley top of WSe_2

[Figs. 4.10(f)(e)], supporting the existence of second order Umklapp scattering. However, no sign of flat band has been found.

We further study the electronic structure of the 11° graphene/WSe_2 heterostructure. This data was obtained from the monolayer area of the sample$_{hBN}$ presented in the previous chapter. Figure 4.11(a) shows the simulation results of both the first and the second order Umklapp scattering, according to which multiple rDCs in the BZ center are expected to be observed. Indeed, we observe strong in-gap dispersion and intensity above both K and Γ valleys, respectively [Figs. 4.11(b)(c)]. The additional linear dispersion above the K valley can be attributed to the valence branch of the first order rDC. The additional intensity above the Γ valley with line-shaped dispersion confirms the existence of the second order Umklapp scattering. However, no sign of flat band has been observed, either.

4.3.3 Umklapp scattering in the graphene/twisted bilayer WSe_2 heterostructure

The absence of flat band in the graphene/monolayer WSe_2 heterostructures indicates the weak interaction between the second order rDCs, which seemingly denies the idea that flat band can be created by Umklapp scattering. However, ARPES measurements on the graphene/twisted bilayer WSe_2 heterostructure present the signature of flat band.

The graphene/twisted bilayer WSe_2 heterostructure used in this study is the sample$_{hBN}$ in the previous chapter. If we use the graphene substrate as reference (0°), the rotation angles of bottom and top layers WSe_2 are 11° and 16.1°, respectively [Fig. 4.12(a)]. The simulation result of the first order Umklapp scattering shows a propeller-like pattern formed by pairs of rDCs [Fig. 4.12(b)], which is directly observed in the CEC [Fig. 4.12(c)]. The simulation result of the second order Umklapp scattering shows a dozen of rDCs in the BZ center [Fig. 4.12(b)], which appear as the weak intensity in the BZ center [Fig. 4.12(c)]. In the cut along Γ-K direction [Fig. 4.12(d)], moiré bands are observed in between the two main bands of Γ-valley. If we zoom into the in-gap area, the first order and the second order rDCs

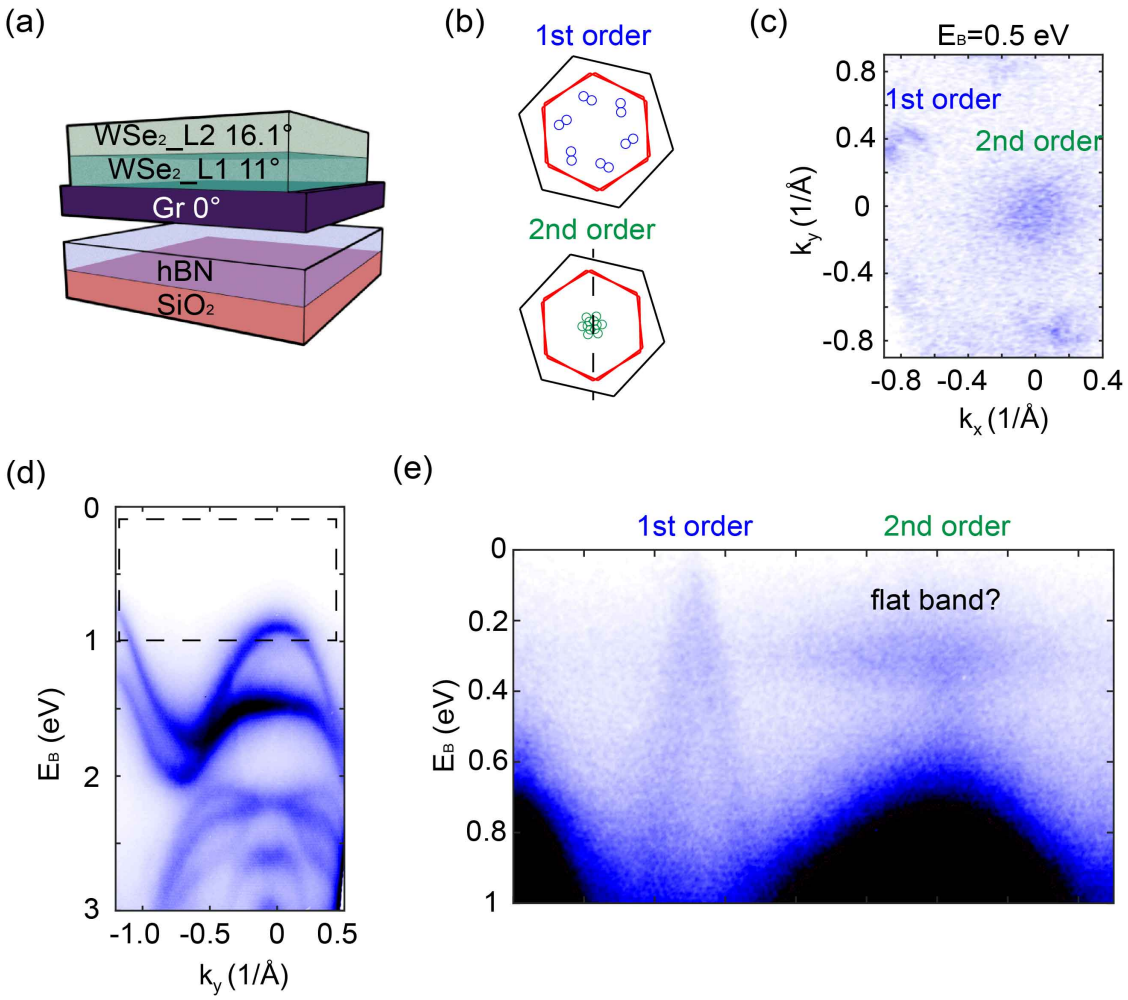

Figure 4.12: Replica Dirac cones in graphene/tbWSe$_2$ heterostructure. (a) Sample geometry. From bottom to top, the red, light-blue, purple, green sheets stand for SiO_2, hBN, graphite substrates and twisted bilayer WSe_2 sample. If we use graphite as reference (twist angle 0°), the bottom and top layer WSe_2 have twist angles of 11° and 16.1°, respectively. (b) Simulation results: red and black lines stand for BZs of WSe_2 and graphene, respectively; blue and green circles stand for the first and the second order rDCs, respectively. (c) CEC at $E_B = 0.5$ eV showing the first and the second order rDCs. (d) Cut across Γ, the direction of which is indicated by the black dashed line in (b). (e) Zoom-in view to show the signature of rDCs and possible flat bands

can be immediately observed. Prominently, flat-band-like features are observed at around $E_B = 0.3$ eV. This flat band turns out to be the intrinsic electronic structure instead of artifact, as it can be constantly observed at different sample positions and different emission angles [Fig. 4.13].

Currently, we don't have a solid explanation why the band hybridization of rDCs is enhanced in the graphene/twisted bilayer WSe_2. One clue could be that

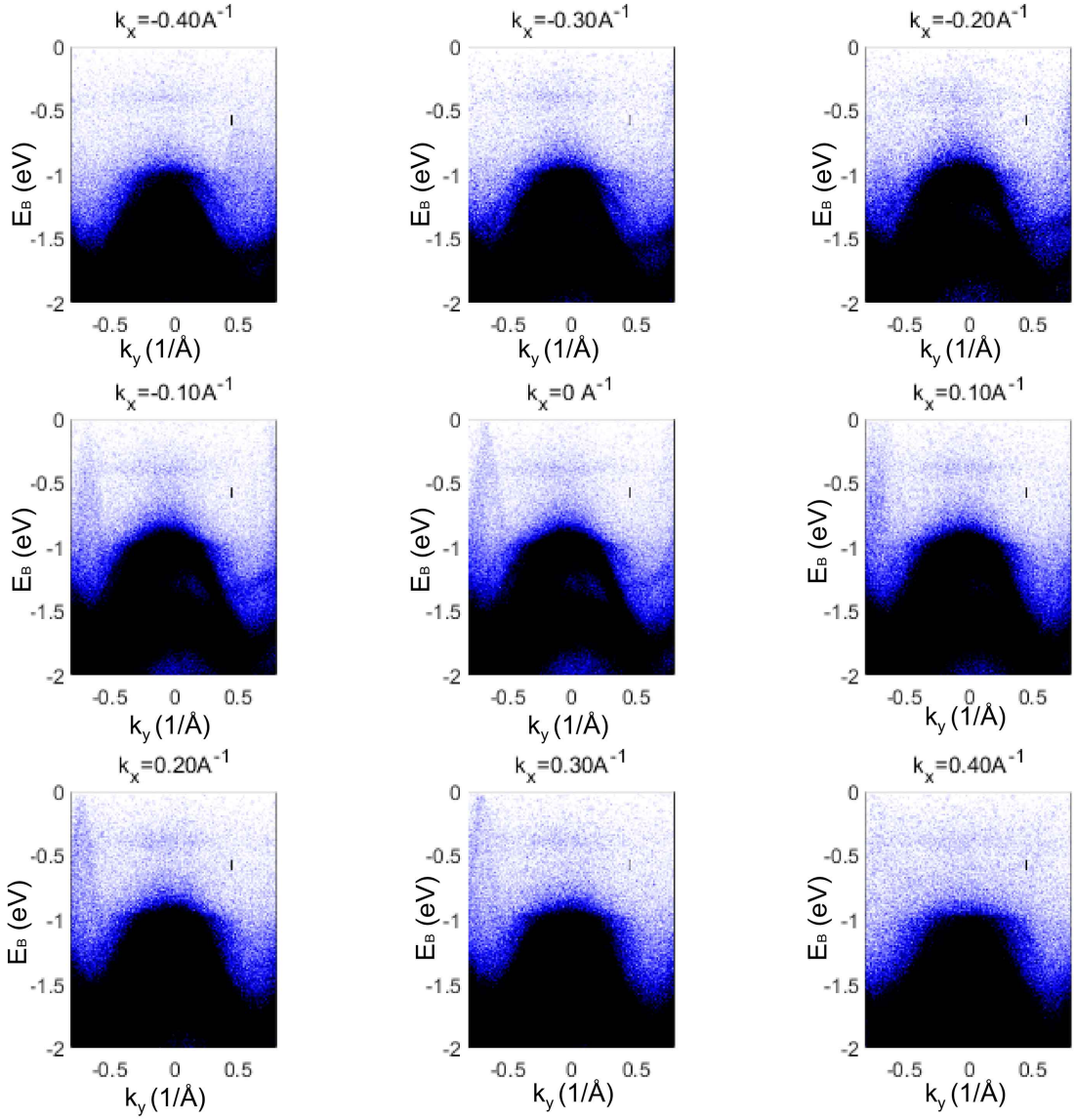

Figure 4.13: Flat band in graphene/tbWSe$_2$ heterostructure. Band dispersions along k_y direction at k_x = -0.4 Å^{-1} to 0.4 Å^{-1}.

the moiré superlattice of 5.1° twisted WSe_2 has a similar lattice constant (3.7 nm) with the effective moiré length (3.8 nm) of the BZ formed by rDCs, which could lead to the formation of an effective trilayer moiré system, and the flat band presents the electronic states in this trilayer system. Related transport phenomena in trilayer moiré systems have been reported in the twisted bilayer graphene and monolayer WSe_2 heterostructure, in which the superconductivity of twisted bilayer graphene is stablized by WSe_2 [79].

4.4 Summary

To summarize, we have studied the electronic structure of 30° trilayer and 33° bilayer twisted graphene, both of which present rDCs inside the first BZ. This observation indicates that Umklapp scattering is universal process in the large angle twisted graphene regardless of the twist angle and the number of layers. The rDCs from the first and the second order Umklapp scattering have been observed in graphene/TMD heterostructures. More interestingly, we observed a mysterious flat band in the graphene/twisted bilayer WSe_2 heterostructure, indicating a possible route to design flat bands by Umklapp scattering.

5 Other projects

Contents

Apart from the study on the twisted two-dimensional materials, I have also conducted and participated in several projects on other material systems during my DPhil in Oxford. In this chapter, we will present two of them: 1. ARPES study on thermoelectric materials BiCuChO (Ch = S, Se) family [104]. In this project, we reveal the coexistence of dispersionless and dispersive bands at the valence band top, which accounts for the excellent thermoelectric performance of BiCuChO. 2. ARPES study on the topological chiral semimetals PtGa family [20, 105]. In this project, we reveal the multi-fold band crossing with a Chern number larger than 1 and associated chiral arc surface states in PtGa, PdGa and PtAl.

5.1 ARPES study on thermoelectric materials BiCuChO (Ch=S, Se) family

5.1.1 Introduction

The thermoelectric (TE) effects arise because the charge carriers moving in solid-state materials carry both charge and heat [106]. When a temperature gradient is applied to a material, the mobile charge carriers at the hot end are inclined to diffuse to the cold end. After the equilibrium is reached, the accumulated charge carriers result in an electrostatic potential (voltage) between the hot and cold ends. This property, known as the Seebeck effect, is the basis of TE power generation. TE materials with prominent Seebeck effect can be fabricated into the TE generator for converting waste heat to electricity [Fig. 5.1]. The n-type (electrons as charge carrier) and p-type (holes as charge carrier) TE materials are combined to form a TE unit, which can double the electrical potential generated in the same temperature gradient. The TE units are wired electrically in series and thermally in parallel to amplify the TE power and provide direct current to external appliances.

According to the laws of thermodynamics, the maximum efficiency (η) of a TE generator is related with the figure of merit (ZT):

$$\eta = \frac{T_h - T_c}{T_h} \cdot \frac{\sqrt{1+ZT}-1}{\sqrt{1+ZT}+\frac{T_c}{T_h}} \tag{5.1}$$

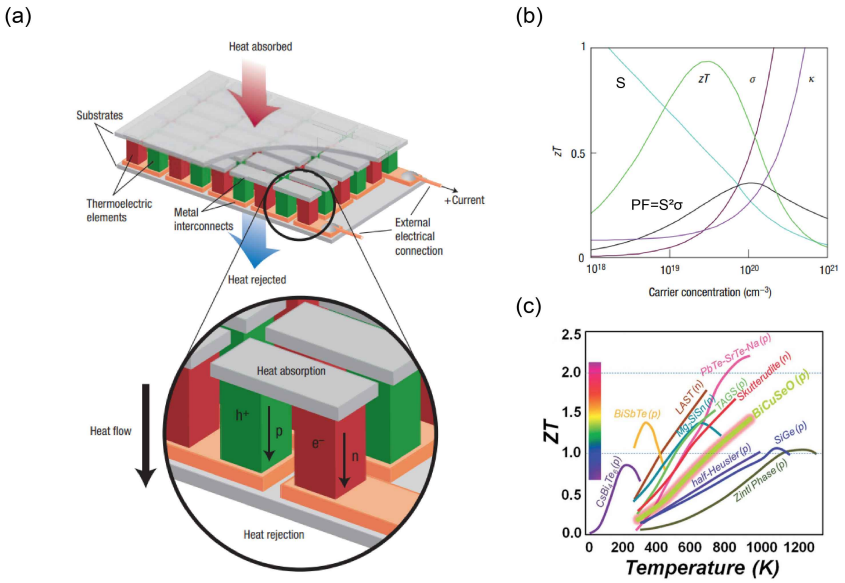

Figure 5.1: Thermoelectric materials. (a) Illustration of the thermoelectric devices. (b) Optimization of the value of ZT. (c) Working temperature range for different thermoelectric materials. (a)-(b) are adapted from [106].(c) is adapted from [107]

where T_c, T_h are the temperatures of the cool and hot ends, respectively,

$$ZT = \frac{S^2\delta}{\kappa}T \tag{5.2}$$

where S is the Seebeck coefficient ($\frac{\delta V}{\delta T}$), σ is the electrical conductivity, κ is the thermal conductivity. It is obvious that the high efficiency η requires large ZT, which then requires large S, σ but small κ. However, as illustrated in Fig. 5.1 (b), it is impossible to optimize all these parameters to get a perfect ZT value due to the conflicting trends against the carrier concentration (n). To ensure that the Seebeck coefficient is large, there should only be a single type of carrier. Mixed n-type and p-type conduction will lead to both charge carriers moving to the cold end, cancelling out the induced Seebeck voltages. Materials with low carrier concentration, such as semiconductors and insulators, can host large Seebeck coefficient, as described by the Pisarenko formula (parabolic band, energy-independent scattering approximation) [106]:

$$S = \frac{2{k_B}^2 T}{3e\hbar^2} m^* (\frac{\pi}{3n})^{2/3} \tag{5.3}$$

where k_B is the Boltzmann constant, e is the electron charge, m^* is the density-of-states (DOS) effective mass at the Fermi level (E_F). However, low carrier

concentration can result in low electric conductivity through the carrier mobility μ:

$$\sigma = ne\mu \tag{5.4}$$

As a result, the maximum of ZT usually appears at a certain doping level for the compromise between S and σ.

The effective mass of the charge carrier provides another conflict. The large effective mass, originates from the flat, narrow bands with high DOS, is favorable for the large Seebeck coefficient. However, the large effective mass is associated with heavy carriers with low velocities and therefore small mobilities. To obtain a small effective mass, the electronic band structure near E_F should be sharp and dispersive. This controversy indicates that good materials host complex electronic structure near E_F, which can provide both heavy and light charge carriers [106].

Recently, BiCuSO and its sister compound BiCuSeO have emerged as promising TE materials due to their intrinsically low lattice thermal conductivity [107–109]. By p-type doping, such as introducing Cu deficiency [110] or replacing Bi^{3+} with A^{2+} (A=Sr, Pb, Mg...) [111–117], the TE performance of BiCuChO can be dramatically enhanced while the lattice structure is barely influenced, which suggests the excellent TE performance in BiCuChO is likely rooted in their electronic structures, as is also supported by the first-principles calculation [114, 118]. On the other hand, BiCuSO has attracted research interest due to its potential for hosting unconventional superconductivity [119–124]: Ubaldini et al. reported a superconducting transition at 5.8 K in polycrystalline $BiCu_{0.9}SO$ [119]; and Mazin et al. proposed that the superconductivity in $BiCu_{0.9}SO$ may be mediated by spin-fluctuation induced by Cu deficiency [120, 122], despite the controversial experimental observation of semiconductor-like behaviour in subsequent transport measurements [123–129]. With these motivations, a systematic investigation on the electronic structure of BiCuSO is of timely need.

In this work, millimeter-sized high-quality BiCuSO single crystals (p-doped due to Bi and/or Cu deficiencies) were synthesized for electrical, magnetic property measurements and ARPES study. In transport measurements, the sample remains

metallic down to 2 K; and no magnetic order but an increase of saturated moment at low temperature ($\sim$ 4 K) is observed from the magnetic susceptibility measurement. From ARPES measurements, comprehensive band structures are acquired, including the flat band predicted by first-principles calculation [118, 120–122], whose large carrier density can enhance the TE performance at high temperatures. Using polarization dependent ARPES measurements, we find that the topmost valance bands mainly consist of the Cu d_{xz}/d_{yz} and S p_x/p_y orbitals. By providing a comprehensive reference of the electronic structure and related physical properties of BiCuSO, our study will assist the search for superconductivity, and promote the advancement of the TE performance in BiCuChO single crystals.

5.1.2 Methods

BiCuSO and BiCuSeO single crystals were grown by the chemical vapor transport method [130, 131]. First, the polycrystalline samples were synthesized using a solid-state reaction method by heating the powders of Bi (Alfa Aesar, 99.999%), Bi2O3 (Sinopharm Chemical Reagent 99.99%),Cu (Sinopharm Chemical Reagent 99.99%), and S (Alfa Aesar 99.5%), or Se (Alfa Aesar 99.999%) in a sealed evacuated quartz tube at about 700 °C for seven days. Second, a certain amount of BiCuSO or BiCuSeO powder and transport agent I_2 were mixed, loaded into the evacuated quartz ampoule, and then placed in a two-zone furnace with the temperature profile of 500–600 °C to grow the crystals. After over ten days, millimeter-sized single crystals with metallic luster and flake shape were obtained. The crystal structure of the as-grown crystals was determined by single-crystal x-ray-diffraction (XRD) measurement (Supernova, Oxford Instrument). The electrical transport measurements were performed with a 9 T physical properties measurement system (PPMS-9T, Quantum Design) by a standard fourprobe configuration. The characterizations of the magnetic properties were carried out in a magnetic property measurement system (MPMS3-SQUID, Quantum Design). The energy-dispersive x-ray spectroscopy (EDS) measurements were carried out with a scanning electron microscope (SEM, FEI-Quantum).

ARPES measurements on BiCuSO were performed at beamline I05 of Diamond Light Source and measurements on BiCuSeO were performed at beamline SIS of Swiss Light Source. The overall energy and angular resolutions are ∼10 meV and $\sim 0.2°$, respectively. The samples were cleaved in situ along the [001] direction and the ARPES measurements were carried out under ultrahigh vacuum of better than 1.3×10^{-10} mbar at the temperature of 6 K. The photon energies used in ARPES experiments on BiCuSO ranged from 120 to 210 eV: fine maps and high symmetry cuts at the ΓMX plane (Γ plane) and ZAR plane (Z plane) were measured at 182 and 164 eV, respectively. The E_F of BiCuSO was determined by the E_F of gold measured in the same beamtime. For BiCuSeO, the photon energy used in ARPES experiments was 186 eV (Γ plane) and 154 eV (Z plane).

The *ab initio* calculations were performed within the framework of density functional theory as implemented in the Vienna Ab-Initio Simulation Package [89]. The HeydScuseria-Ernzerhof hybrid exchange-correlation function [132] and a k mesh of 9×9×4 were taken. Calculations without spin-orbit coupling are presented in this paper due to better consistency. Due to the stoichiometric structure used in the calculation, in BiCuSO, the calculated E_F locates 0.23 eV higher than the valence band maximum (VBM); in BiCuSeO, the calculated E_F locates 0.19 eV higher than the VBM. In this paper, the calculated band structure of BiCuSO is shifted by +0.20 eV and renormalized by a factor of 1.01; that of BiCuSeO is shifted by +0.19 eV. The calculation was performed with a non-magnetic assumption.

5.1.3 Results and discussion

Characterization of BiCuSO single crystals

BiCuSO has the same crystal structure as LaFeAsO (space group $P4/nmm$) [133], formed by the alternative stacking of insulating BiO_4 layers and conductive CuS_4 tetrahedral layers (highlighted by blue tetrahedra) [Fig. 5.2]. Our singlecrystal samples appear as millimeter-sized thin flakes with black metallic luster [Fig. 5.2]. The single-crystal XRD patterns confirm the high quality of our samples, where we extract the lattice constants of a = 3.87 Å and c = 8.57 Å [Fig. 5.2(b)]. The

EDS measurement [Fig. 5.2(d)] presents characteristic peaks of all four elements, from which we find the Bi/Cu/S atomic ratio to be 0.83/0.9/1.0. The established literature shows that Bi deficiency can function as hole doping which rigidly shifts the electronic structure, and Cu deficiency is predicted to induce magnetic order and superconductivity [120–122]. We notice that our samples have the same proportion of Cu deficiency as the previously reported BiCuSO samples that demonstrate superconductivity [119]. Figure 5.2(c) illustrates the Brillouin zone (BZ) of BiCuSO, and the notation of high symmetry points when orbital characters are not considered. In the following content, we focus on the electronic structure in high symmetry planes, the Γ plane (marked by green) and Z plane (marked by blue).

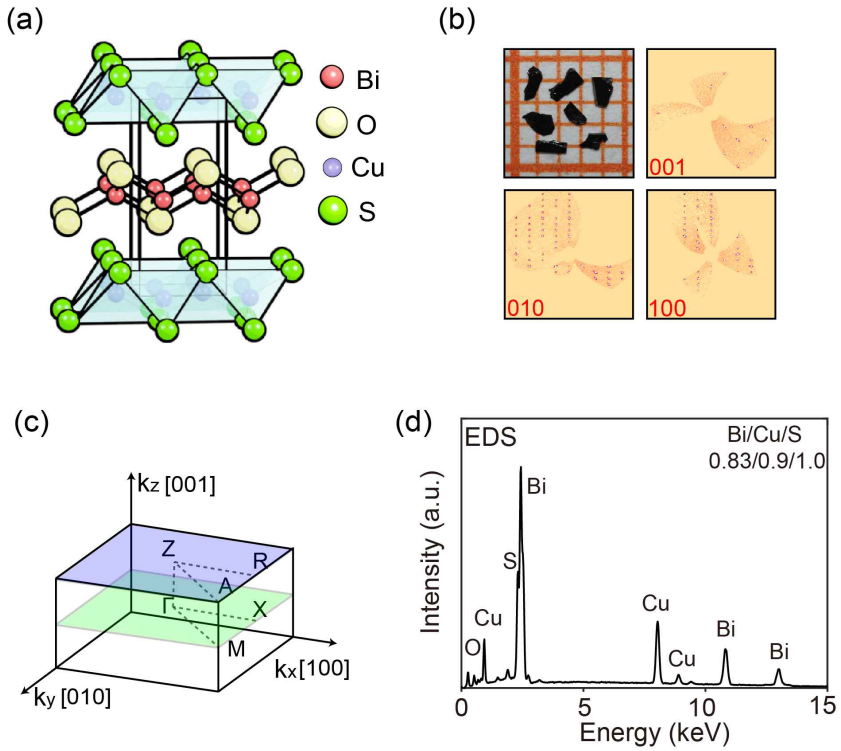

Figure 5.2: Characterization of BiCuSO single crystals. (a) Schematic illustration of crystal structure, with CuS_4 tetrahedral layers highlighted in light blue. (b) Photography and XRD patterns along different directions. (c) EDS results. (d) Brillouin zone labeled with high symmetry points. The ZAR (Z) plane and $MX\Gamma$ (Γ) plane are marked in blue and green, respectively.

Electrical properties of BiCuSO single crystals

Electrical and magnetic properties of BiCuSO single crystals are presented in Fig. 5.3. Our samples exhibit the typical metallic behavior, showing a monotonically

increasing resistivity (ρ_{xx}) against temperature (T) from 2 to 300 K [Fig. 5.3(a)]. The zoom-in view at low temperature confirms there is no superconducting transition down to 2 K. The Hall measurements [Fig. 5.3(b)] show a linear increase of Hall resistivity (ρ_{xy}) against magnetic field (B) at all temperatures, indicating only a single type of charge carrier in BiCuSO crystals and that the dominant carriers are holes. Carrier densities [Fig. 5.3(c)] extracted from Hall coefficients have values around 10^{19} cm^{-3}, an order of magnitude larger than that reported in polycrystalline samples [124–127, 129], and show an increase of ≈40% from 200 to 2 K. The magnetoresistance (MR) measurements [Fig. 5.3(d)] show negative MR below 10 K and no apparent variation above 100 K. The metallic behavior in BiCuSO single crystals can be attributed to the Bi and Cu deficiencies, which introduce sufficient carriers to the degenerate phase and, meanwhile, result in weak localization at low temperature [131, 134].

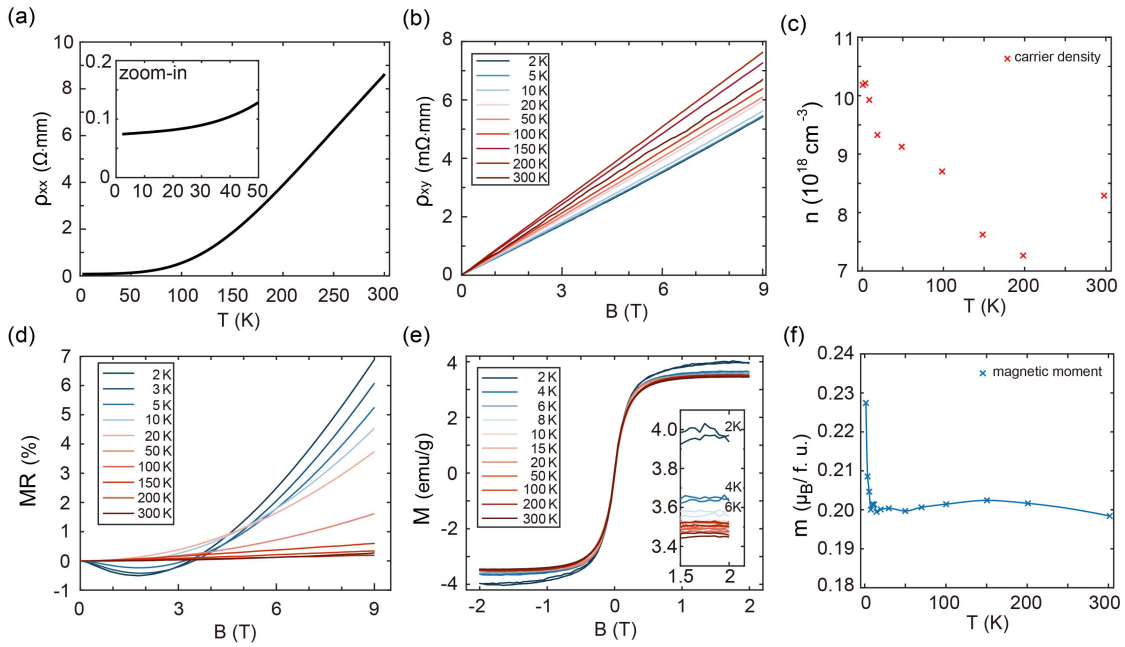

Figure 5.3: Electrical and magnetic properties of BiCuSO. (a) Temperature-dependent resistivity curve, with a zoom-in at low temperature shown as the inset. (b) Hall resistivity curves at different temperatures. (c) Temperature-dependent carrier density extracted from (b). (d) Magnetoresistance (MR) curves at different temperatures. (e) Field-dependent magnetization at different temperatures, with zoom-in around 2 T shown as an inset. (f) Magnetic moments per formula unit (f.u.) at different temperatures extracted from the data in (e).

Magnetic properties of BiCuSO single crystals

Cu in stoichiometric BiCuSO has an electronic configuration of $3d^{10}$, which contributes zero magnetic moment according to Hund's rules [135]. Calculation shows that 10% Cu deficiency in BiCuSO is favorable for a ferromagnetic order, where Cu can contribute ≈0.12 μ_B per formula unit (f.u.) [120, 122]. Karna et al. observed a saturated moment of 0.61 μ_B/f.u. at 3.7 K in $BiCu_{0.94}SO$ polycrystalline samples and claimed a canted ferromagnetic order, which evolves from an in plane antiferromagnetic order at 180 K [125, 126]. However, the magnetization loops in our samples indicate no long-range ferromagnetic order down to 2 K (current results cannot exclude the existence of short-range ferromagnetic order [136]). Curiously, the zoom-in view around 2 T shows an increase of the saturated magnetization at low temperature. The saturated magnetic moment [Fig. 5.3(f)] extracted from Fig. 5.3(e) shows little variation (≈0.20 μ_B/f.u.) when the temperature decreases from 300 to 8 K, while it jumps to ≈0.23 μ_B/f.u. (+14%) when temperature further decreases to 2 K. As our samples are flakelike and all the magnetic measurements were performed normal to the ab plane, this sharp increase may result from the reorientation of the magnetic easy axis from in-plane to out-of-plane direction [125]. Another possible mechanism is the change of Cu $3d$ electronic configuration (chemical valence), which can also lead to the increase of the saturated moment [137]. Detailed investigation on the magnetic order of the BiCuSO single crystal is needed for clarifying this phenomenon.

Electronic structure of BiCuSO

Figure 5.4 offers an overview of the electronic structure by presenting the band dispersion along Γ-X-M-Γ-Z-R-A-Z. We observe dispersive bands along Γ-M and Z-A, which form multiple hole pockets near the VBM, in good consistency with the calculation. We also observe broad features along Γ-X and Z-R, which can be attributed to the weakly dispersive bands in the calculation. This coexistence of light and heavy hole bands near the VBM is favorable for TE performance, as the light hole bands can contribute to good electrical conductivity while the heavy

hole bands can maintain a large Seebeck coefficient, which endows BiCuSO with promising potential for thermoelectricity [138].

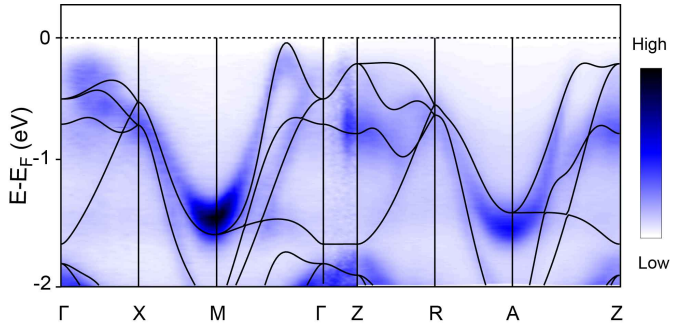

Figure 5.4: Overview of the electronic structure of BiCuSO. Electronic band dispersion along Γ-X-M-Γ-Z-R-A-Z overlapped with calculation.

The identification of Γ and Z planes was realized by the photon-energy depenedent measurement (also known as the k_z measurement) along the [110] direction [Fig. 5.5]. In the constant energy contours (CECs, in $k_y - k_z$ plane) close to the E_F, nearly-straight dispersions are observed along the k_z direction, consistent with the quasi-2D crystal structure; in the CECs at deeper binding energies, wave-like patterns with the same periodicity of the BZ are observed. By comparing the energy-momentum disperisons at peaks and nodes of the wave with calculation, we can determine 182 eV and 164 eV as the Γ and Z planes, respectively.

The CEC at the valence band top (VBT) in the plane [Fig. 5.6(a)] shows quadruple segments located between Γ and M. In the high symmetry cut along M-Γ-M measured using linear-horizontally (LH) polarized photons [Fig. 5.6(b-i)], we observe the three bands predicted by the calculation [Fig. 5.6(b-iii)]: the band α that forms the VBM the center of which locates at $k_{//} = \pm 0.35$ Å^{-1}; the hole band γ the maximum of which locates at ~ 0.24 eV below E_F ; and the band β that appears as broad features with weak intensity. By fitting the VBM to a parabola, we extract an effective mass of about –0.56 m_e [Fig. 5.7]. In the high symmetry cut measured using linear-vertically (LV) polarized photons [Fig. 5.6(b-ii)], we observe intensive band α around the VBM while diminishing bands β and γ because of orbital selection. The CEC at VBT in the Z plane [Fig. 5.6(c)] presents a weak feature at the center apart from the quadruple segments, indicating the presence of

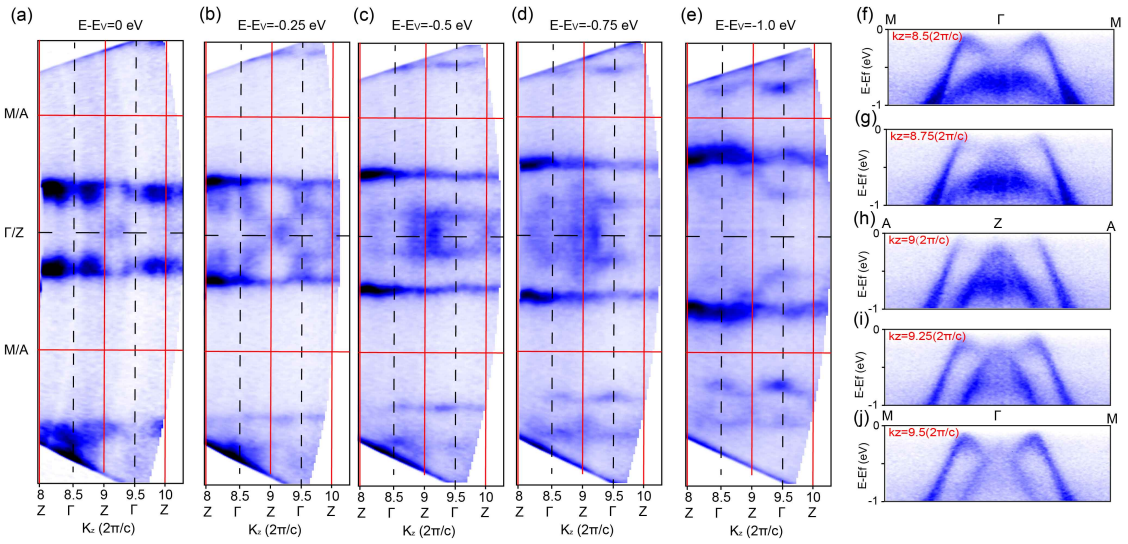

Figure 5.5: Electronic structure of BiCuSO along k_z. (a)–(e) CECs of k_z-dependent data, overlapped with the Brillouin zones along the corresponding direction. (f)–(j) Cuts along the [110] direction at the different k_z positions.

additional electronic structure near E_F . In the LH cut along A-Z-A [Fig. 5.6(d-i)], we observe similar band dispersion as along M-Γ-M, featured by the dispersive bands α' and γ'. In the LV cut along A-Z-A [Fig. 5.6(d-ii)], we determine the maximum of band α' at $k_{//} = \pm 0.38$ Å^{-1} and extract the effective mass of –0.63 m_e [Fig. 5.7]. The hole band at Z cannot be clearly identified due to the intensive triangular feature, which results from the resonance of S $2p$ orbitals [139].

It is notable that calculations predicted flat bands along R-Z-R near the VBM, which could be the origin of the high ZT value in the hole-doped BiCuSO. First, this flat band contributes to a local extremum in the DOS, which could account for the dramatic increase of carrier density and the enhancement of electrical conductivity in the p-type samples [115]. Second, according to the Pisarenko relationship [106], charge carriers with large effective mass are necessary for the large Seebeck coefficient. According to both our experimental data and the calculation, the valence band top along the [110] direction (Γ-M and Z-A) shows dispersive bands, which contributes a hole carrier with small effective masses [Fig. 5.7] and is favorable for the electrical conductivity. The heavy carriers are most likely contributed from the heavy hole bands along the [100] direction (Γ-X and Z-R), or the fine structures around Z [116, 118].

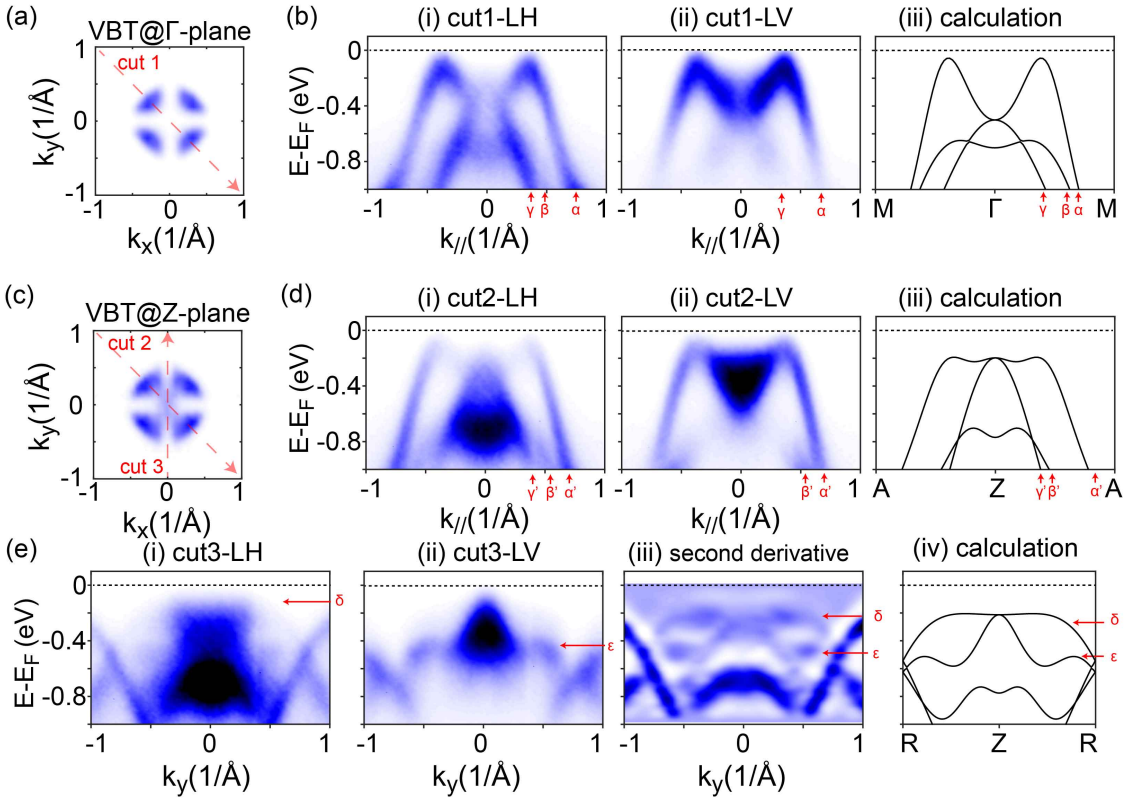

Figure 5.6: Electronic structure of BiCuSO in high-symmetry planes. (a) CEC at the valence band top (VBT) in the Γ plane, measured in LH. (b) High symmetry cuts along M-Γ-M measured in (i) LH, (ii) LV, and (iii) corresponding calculation. (c) CEC at the VBT in the Z plane, measured in LH. (d) High symmetry cuts along A-Z-A in (i) LH, (ii) LV, and (iii) corresponding calculation. (e) High symmetry cuts along R-Z-R in (i) LH, (ii) LV, (iii) the second derivative of the LH results, and (iv) corresponding calculation. The CECs are mirror symmetrized, and have an integration width of 50 meV.

Our calculation [Fig. 5.6(e-iv)] reproduces the flat band (band δ) along R-Z-R and the hole band at Z (band ϵ). In the LH cut along X-Γ-X [Fig. 5.6(e-i)], we observe flat features in the center, and weak intensity at both sides [also observed in Fig. 5(d-ii)] at ≈0.2 eV below E_F . These features are clearly presented by the second derivative along the energy axis [Fig. 5.6(e-iii)], showing the weakly dispersive band ranging from k_y = –0.4 to 0.4 Å^{-1} (band δ) and the hole band at Z (band ϵ), which are qualitatively consistent with the calculation. In the LV cut along X-Γ-X [Fig. 5.6(e-ii)], we observe the band ϵ with strong intensity around the top. From the maximum of the hole band at Z, we estimate a binding energy of ≈150 meV the flat band, which is significantly larger than k_BT at low temperature. We therefore conclude that the electrical properties of hole-doped

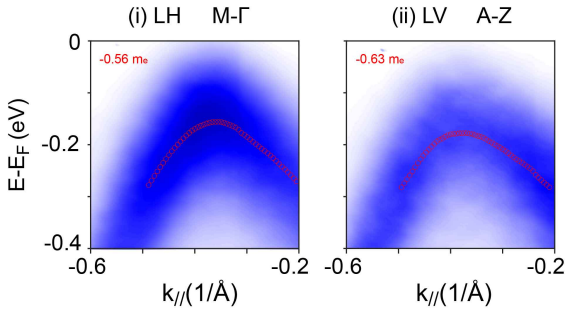

Figure 5.7: Zoom-in view around the valence band top. (i) (ii) Zoom-in views of the pocket between (i)Γ-M (ii) Z-A, respectively. The red circles show the peak positions of the energy distribution curves, which are fitted with parabolic curves to obtain the effective masses.

BiCuSO at low temperature are dominated by the quadruple hole bands between $\Gamma(Z)$ and M (A). However, in the high temperature range ($T > 1000$ K), this flat band will be involved in the TE process, and substantially contribute to the Seebeck coefficient as well as the carrier density [107, 118].

Orbital characters of BiCuSO

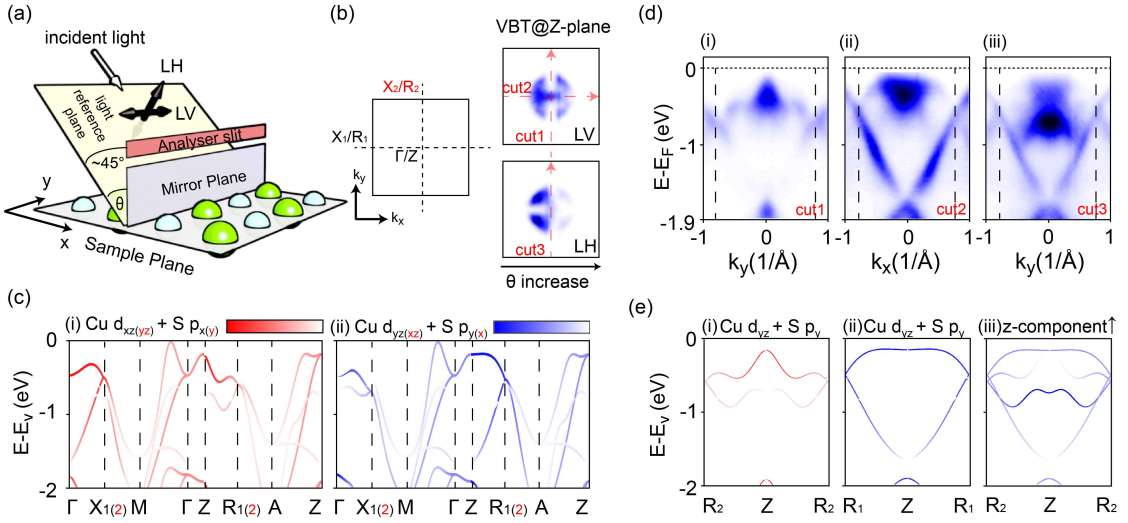

Figure 5.8: Orbital characters of the valence band in BiCuSO. (a) Schematic illustration of the ARPES experimental geometry. (b) Left panel: Brillouin zone (BZ) and notation used in the calculation of orbital character. Right panel: CECs at VBT in the Z plane measured in LV and LH. The dashed lines in the left panel are used for locating the high symmetry points. (c) Calculated orbital weights of (i) Cu d_{xz} + S p_x and (ii) Cu d_{yz} + S p_y along the horizontal direction (black notation), or orbital weights of (i) Cu d_{yz} + S p_y and (ii) Cu d_{xz} + S p_x along the vertical direction (red notation). (d) High symmetry cuts along R-Z-R measured in (i) LV and (iii) LH, and (ii) cut along R-Z-R obtained from the map data. The vertical dashed lines show the boundary of BZ. (e) Simulation results following the photoemission selection rules.

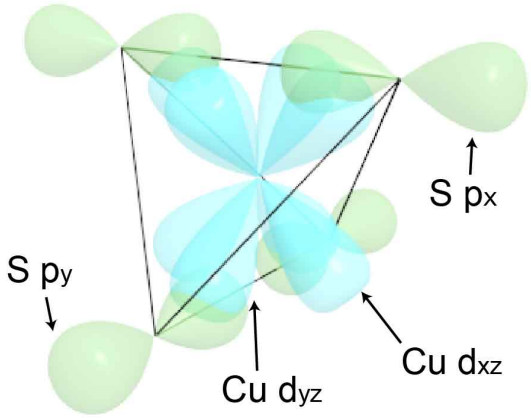

Figure 5.9: Illustration of the quasi-one-dimensional conductive chain in a CuS_4 tetrahedron.

Analysis of the polarization dependence of the ARPES results reveals the orbital characters of the valence band [Fig. 5.8]. The experimental geometry for the ARPES measurement is illustrated in Fig. 5.8(a). The sample mirror plane is aligned coincident with the direction of the analyzer slit while measuring high symmetry cuts along *R*-*Z*-*R* (cuts 1 and 3). In this geometry, the LV cut is supposed to show zero intensity of Cu $3d_{xz}$, $3d_{xy}$, and S $3p_x$ orbitals, and the LH cut is supposed to show zero intensity of Cu $3d_{yz}$, $3d_{x^2-y^2}$, and S $3p_y$ while presenting some intensity from the out-of-plane orbital components (Cu d_{z^2} and S p_z) [12, 140].

We find the electronic structure of BiCuSO no longer follows the fourfold symmetry but only mirror symmetry when orbital characters are considered, and thus redefine the BZ as the left panel of Fig. 5.8(b). This reduced symmetry is directly presented by the original data of LV and LH CECs at VBT [Fig. 5.8(b), right panels]. The calculated orbital weights show that the valence band top is mainly contributed from the hybridization of Cu $3d_{xz}$ and S $3p_x$, Cu $3d_{yz}$, and S $3p_y$ orbitals [Fig. 5.8(c)], indicating the formation of a quasi-one-dimensional electronic structure in real space [Fig. 5.9], which is favorable for the TE performance [141–144]. We also notice some contribution from the Bi orbitals at the topmost band along Γ-*X* and Γ-*Z*, the maximum percentage of which is 10.76% at Γ, which is smaller than that reported in BiCuSeO (≈20%) [141]. The flat band along *Z*-R_1

is dominantly contributed from Cu d_{yz} + S p_y orbitals while that along Z-R_2 is dominantly contributed from Cu d_{xz} + S p_x orbitals. This nonequivalence in orbital weight is demonstrated by comparing the cuts along nominally equivalent directions [Fig. 5.8(d)]. Both cuts 1 and 2 [Figs. 5.8(d-i) and (d-ii)] follow the same selection rule and present the intensity from Cu d_{yz} + S p_y orbitals as predicted by simulation [Figs. 5.8(e-i) and (e-ii)]. We attribute the intensity below the flat band [Fig. 5.8(d-ii)] to the resonance induced broadening [139]. Compared with cut 2, cut 3 shows stronger intensity at around -0.8 eV, which is contributed from the Cu d_{z^2} and S p_z electrons excited by LH photons [Fig. 5.8(e-iii)].

Comparison with BiCuSeO

To understand the communal origin of promising TE performance in the BiCuChO family, we further investigate the electronic structure of BiCuSeO. Figure 5.10(a) presents an overview of the electronic structure of BiCuSeO, featured by the coexistence of light and heavy hole bands near the VBT. The Fermi surface of BiCuSeO [Fig. 5.10(b-i)] presents a cruciform surrounded by a square cage, obviously different from the VBT of BiCuSO [Fig. 5.6(c)]. The cut along A-Z-A [Fig. 5.10(b-ii)] presents a clear E_F crossing from the outside bands, showing the VBM is above E_F. The cut along R-Z-R [Figs. 5.10(b-iii) and (b-iv)] presents a hole pocket capped by the broad intensity in the vicinity of E_F, which can be attributed to the weakly dispersive band in the calculation along Z-R [Fig. 5.10(a)].

Our observation confirms the overall similarity in the valence band structure in BiCuChO, which is rooted in the similarity of crystal structure [118]. Similar to BiCuSO, the top-most bands in BiCuSeO are strongly dispersive along the [110] direction while weakly dispersive along the [100] direction, indicating the observed "flat" band along Z-R could serve as the origin for the large Seebeck coefficient required by the Pisarenko relation [106]. Additionally, this flat band can also contribute to a large DOS at E_F , favorable for the increase of carrier density and the enhancement of electrical conductivity in the hole-doping process.

Despite the common points, our calculation also presents divergences in the VBT of BiCuChO, particularly around Z. Unlike BiCuSO, the Z-centered hole

pocket in BiCuSeO is obviously higher than the nearby hole bands; the weakly dispersive band along Z-R also shows subtle differences. We notice that these fine structures near the VBT contribute to complex thermoelectric behavior in BiCuSeO [116]. Unfortunately, these fine structures were unobservable in the ARPES measurements due to the heavily hole-doped samples. A detailed investigation on the electronic structure of BiCuSeO is needed for understanding the divergence in TE performance of the BiCuChO family.

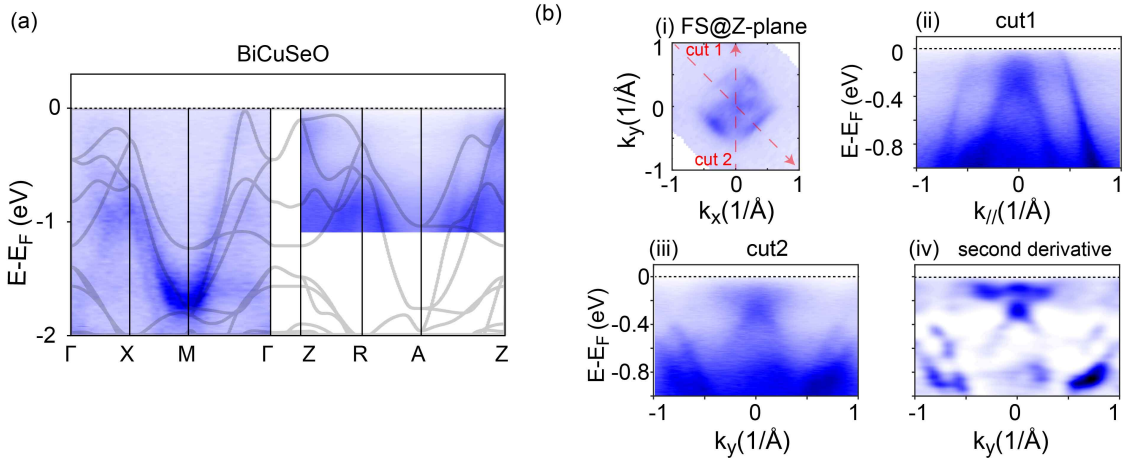

Figure 5.10: Electronic structure of BiCuSeO.(a) Electronic band dispersion along Γ-X-M-Γ-Z-R-A-Z overlapped with calculation. (b-i) Fermi surface map in the Z plane. (ii) Cut along A-Z-A. (iii) Cut along R-Z-R and (iv) corresponding second derivative. The data in the Z plane were measured in circular-left (CL) polarization at 154 eV. The data in the plane were measured in LH polarization at 186 eV.

5.1.4 Summary

In summary, we investigate the transport properties and the electronic structure of hole-doped BiCuSO single crystals. Our samples present metallic transport behaviors without superconducting transition down to 2 K. The magnetization loops at different temperatures present no magnetic order, while the increase of saturated magnetic moment at 4 K indicates possible reorientation of the easy axis. Our ARPES measurements directly visualize the valence band structure of BiCuSO and BiCuSeO, especially the weakly dispersive bands along Z-R. These flat bands could account for the enhancement of electrical conductivity in the

hole-doping process, and contribute hole carriers with a large effective mass that are favorable for a large Seebeck coefficient.

5.2 ARPES study on topological chiral semimetals PtGa family

An object that cannot be superimposed with its mirror image is defined to be chiral, a concept has found widespread applications across the modern sciences. In condensed matter physics, chirality is directly presented by the crystal structure with neither mirror nor inversion symmetries, which can be found in the 65 Sohncke space groups [145, 146]. The structural chirality can endow crystalline materials with fascinating properties, such as natural optical activity, negative refraction in metamaterials [147], non-reciprocal effects such as magneto-chiral birefringence of light or electronic magneto-chiral anisotropy [148, 149], chiral magnetic textures such as helices and skyrmions [150] or unusual superconductivity [151]. Recently, chiral crystals have been predicted to host topologically non-trivial band structure [152–154], such as multifold band crossings with large Chern number (>1), chiral arc surface states (SS) [155–158], and singular Weyl point [159, 160], which can lead to exotic electronic properties, such as quantized circular photogalvanic effect [161]. In this section, we will present ARPES study on the electronic structures of chiral semimetals PtGa, PtAl [105], PdGa [20] (the PtGa family).

5.2.1 Chiral crystal structure

The PtGa family crystallize in the B20-type structure (space group 198), the structural chirality of which is determined by the Pt/Pd and Ga/Al helices that screw around the 2_1-screw axis with C3 symmetry about [111] direction [Fig. 5.11(a)]. In the view along [111] direction, the handedness of the helices can be immediately distinguished [Fig. 5.11(b)]. In the enantiomer A, the helix of Pt/Pd atoms has a clockwise distribution from bottom to top, while the helix of Ga/Al atoms has an anti- clockwise distribution from bottom to top. In the enantiomer B, the atom distributions in both kinds of helices are opposite to those in enantiomer

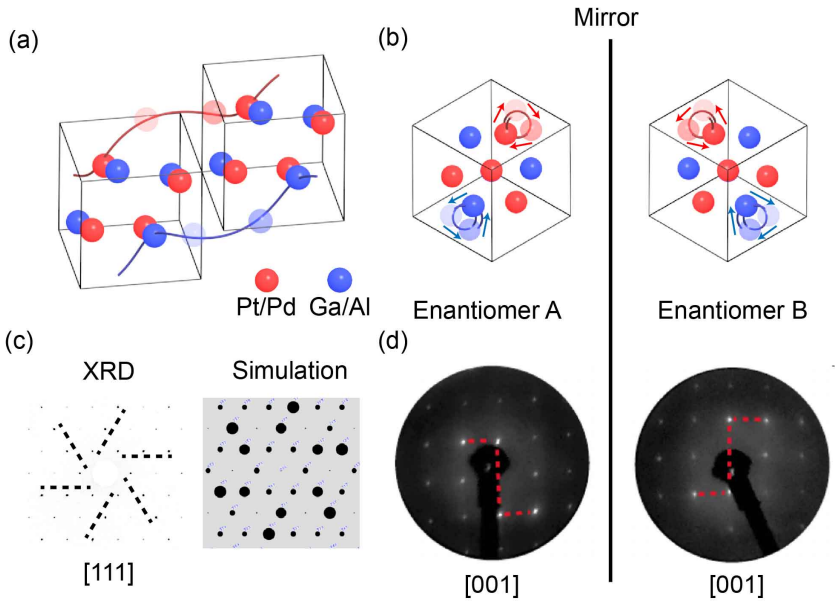

Figure 5.11: Chiral crystal structure of PtGa family.(a) Schematic illustration of the chiral crystal structure of PtGa. Red and blue helices are used to demonstrate the chiral distribution of Pt and Ga atoms along the [111] direction, respectively. (b) Crystal structures with opposite handedness in the view of the [111] direction. The transparency of the balls indicates the atomic positions from top to bottom. (c) Single crystal X-ray diffraction patterns of PtGa along the [111] direction (left) and corresponding simulation results (right). Black dashed guidelines are used to show the chiral pattern formed by the intensive diffraction spots.(d) LEED patterns for two PdGa samples with opposite chirality. The S-shaped intensity distribution of the diffraction spots (highlighted by red dashed lines as guides for the eye) reflects the handedness of the crystal structure. (d) is adapted from [20]

A. The structural chirality can be characterized by single-crystal X-ray diffraction (XRD) and low-energy electron diffraction (LEED) techniques. The propeller-like intensity distribution in the XRD pattern along [111] direction fits perfectly with the simulation and confirms the lack of mirror symmetry in the bulk structure [Fig. 5.11(c)]. The LEED pattern is more sensitive to the surface structure [20], which shows opposite S-shaped intensity distribution in two enantiomers, reflecting the chiral atom positions near the surface [Fig. 5.11(d)].

5.2.2 Topological non-triviality

The discovery of topological insulators reinvigorated the understanding of the electronic structure and inspired generalization of the topological band theory in condensed matter physics [155, 162, 163]. This led to the discovery of quasiparticle

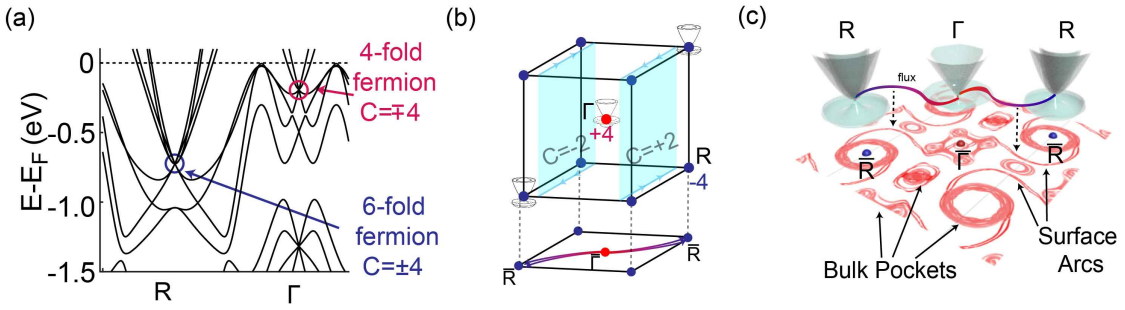

Figure 5.12: Topological properties of PtGa family.(a) Bulk band structure of PtGa, showing the six-fold and four-fold band crossings at the R (red) and Γ (blue) points, respectively. The Chern numbers associated with these crossings at R and Γ are of magnitude 4 and have opposite signs. (b) The Brillouin zone (BZ) of PtGa labelled with high symmetry points and their Chern numbers. Two light blue slices are the reference planes that separate the sinks and sources of the Berry curvature, which have Chern numbers of magnitude 2 with opposite signs. The gradient arrows in the projection plane present the direction of Berry flux. (c) Illustration of the Fermi-arc surface states (FSSs), which connect the projected Fermi pockets at the projection R and Γ points.

excitations featured by linear band crossing, such as Dirac [164, 165] and Weyl fermions [166], which can serve as a direct analogy to fundamental particles in high-energy physics. On the other hand, the so-called fermions in electronic structure need not necessarily follow the Poincare symmetry required by the real particles. Instead, they must respect the crystal symmetry of one of the 230 space groups. Therefore, there is the potential to find new types of fermionic excitations in condensed-matter system that have no counterpart in high-energy physics [154].

The multifold band crossing (the so-called multifold fermion) protected by chiral crystal symmetry is one of the unique quasiparticles in condensed-matter system. In contrast to Weyl fermions with Chern number ±1, multifold fermions in the bulk state (BS) can host large Chern numbers (>1), leading to multiple chiral Fermi arcs in the SS [154]. Moreover, as the location of multifold fermion is enforced to the high-symmetry time-reversal invariant momenta by the chiral symmetry, the Fermi-arc surface states (FSSs) should expand throughout the full Brillouin zone [152, 153]. In PtGa family, the calculated bulk band structure [Fig. 5.12(a)] shows a six-fold band crossing at the R point (blue circle) and a four-fold band crossing at the Γ point (red circle). Further calculation of topological invariants predicts a Chern number of magnitude 4 at the R and Γ points with opposite signs.

The opposite signs of the topological invariants are directly linked to the left- and right-handedness of two enantiomers of the crystal structure. If we assign the Chern numbers +4 to the Γ point and -4 to the R point, we can get sources and sinks of the Berry curvature at the center and corner of the BZ, respectively [Fig. 5.12(b)]. The Berry flux from sources to sinks endow a Chern number of magnitude 2 (the sign is determined by the direction of flux) to the reference planes which separate the Γ and R points. If we imagine this plane to be a two-dimensional quantum Hall phase, then the number of edge states of the slice is directly related to its Chern number magnitude, whereas their direction depends on its Chern number sign. As a result, quadruple arcs are expected to connect the projection of the Γ and R points, and doublet FFSs are expected in each branch of arcs [Figs. 5.12(b)(c)].

Very recently, apart from the multifold fermions and chiral FSSs, PtGa family have been also found to host singular Weyl point surrounded by charged nodal walls, detailed discussion on which is available in ref [159, 160].

5.2.3 Multifold bulk band crossings

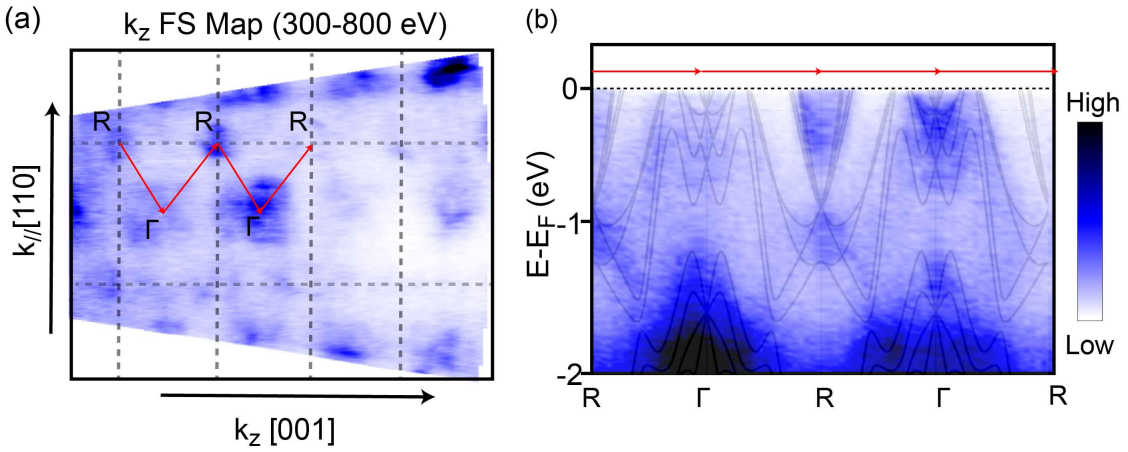

Figure 5.13: k_z **map of PtGa.**(a) Fermi surface map along k_z direction showing the periodicity in the reciprocal space. (b) Band dispersion along R-Γ-R-Γ-R direction obtained from the k_z data.

To validate the topological non-triviality of PtGa family, the first step is to confirm the existence of multifold band crossings at high-symmetry point. We used soft-X-ray ARPES (XR-ARPES) to study the bulk electronic structure. Figure 5.13

presents the fermi surface (FS) map along k_z direction and band dispersion along R-Γ-R-Γ-R direction of PtGa, where the clear periodicity serves as a reference to determine the photon energy associated with the high symmetry planes.

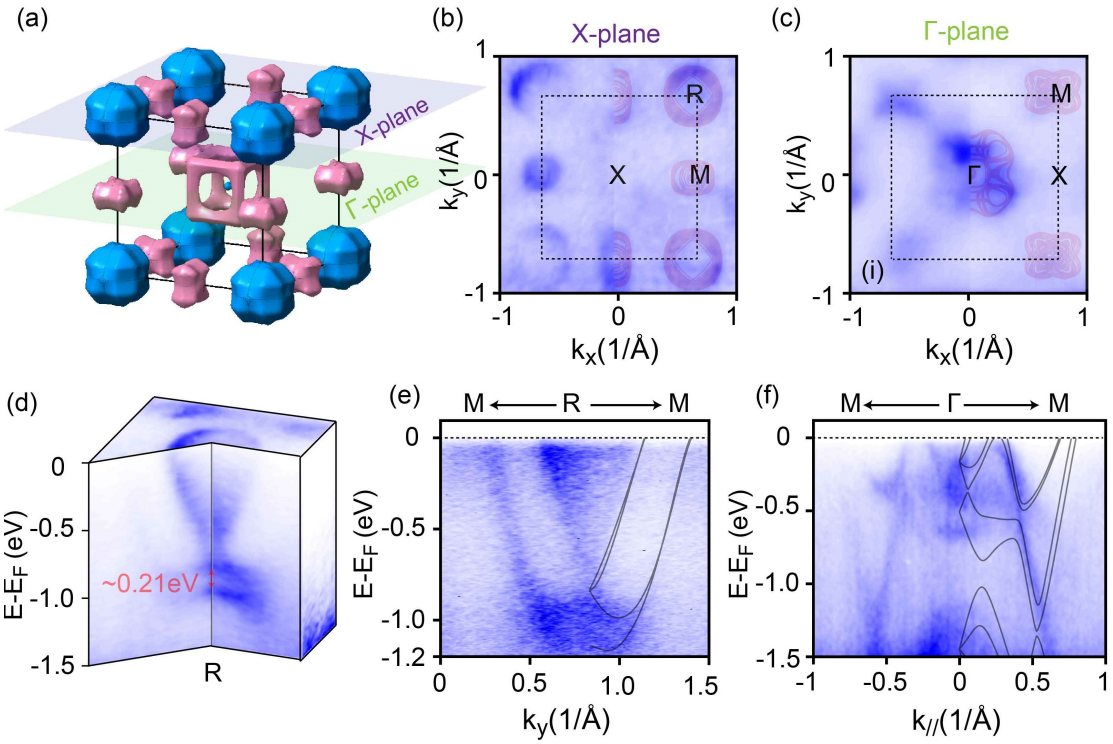

Figure 5.14: Bulk states of PtGa. (a) Illustration of the FS of PtGa in 3D BZ (hole pockets in pink and electron pockets in blue). The XMR and ΓXM planes are marked by purple and green colors, respectively. (b), (c) ARPES intensity maps at E_F showing the FSs in the (b) XMR plane and (c) ΓXM plane overlapped with calculated FSs. (d) 3D illustration of the band structure around R. (e), (f) ARPES intensity spectra along the (e) M-R-M and M-Γ-M directions overlapped with calculated band dispersions.

We performed a direct comparison between the ARPES data in high-symmetry planes and ab initio calculations [Fig. 5.14]. The calculated 3D bulk FS of PtGa is illustrated in Fig. 5.14(a). We observe large electron pockets (blue) at the R point, smaller hole pockets (pink) at the M point, and a tiny electron pocket surrounded by a cage-like hole pocket at the Γ point. Figure 4(b) displays the ARPES intensity map at the E_F in the XMR plane, showing a round pocket at the R point and a smaller pocket at the M point, consistent with the BS calculation. The FS in the ΓXM plane [Fig. 5.14(c)] that presents the butterfly-like features at the M point and cage-like structure around the Γ point also agrees well with the prediction. The

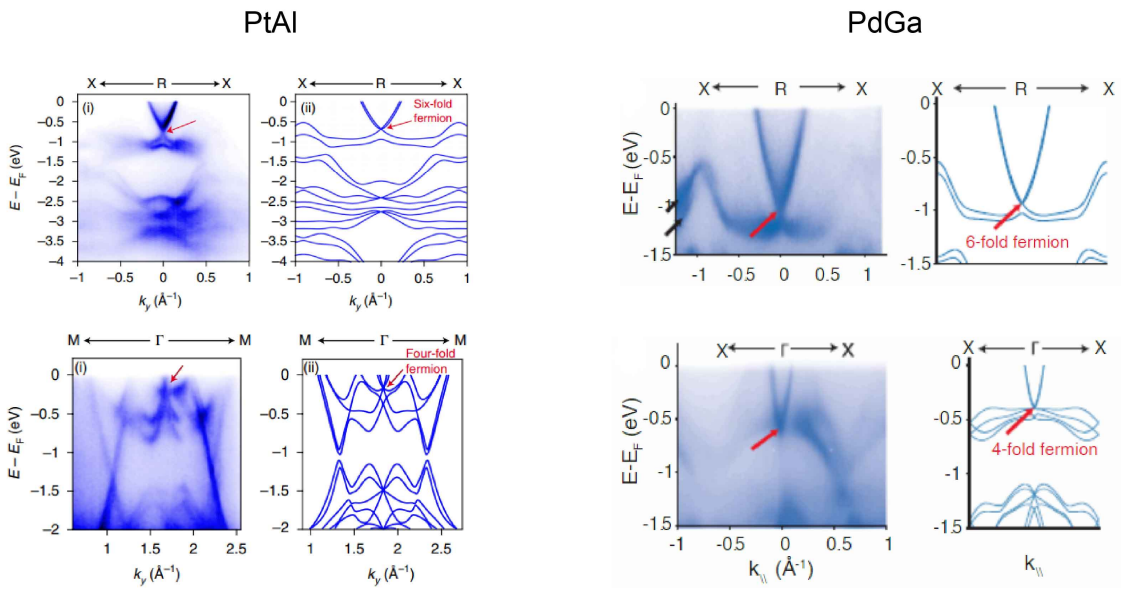

Figure 5.15: Bulk states of PtAl and PdGa. Figures are adapted from [20, 105].

3D (k_x-k_y-E) band structure around the R point is illustrated in Fig. 5.14(d), where the six-fold band crossing at the R point is directly visualized and a spin-orbit-coupling (SOC) splitting around 0.21 eV is presented. From the high symmetry cut along the M-R-M direction [Fig. 5.14(e)], we can determine the binding energy of the six-fold fermion is $E_B \approx 0.80$ eV, which is quantitatively consistent with the calculation. Figure 4(f) shows the band dispersion along the M-Γ-M direction overlapped with the calculation. Although the complex band structure near Γ makes it challenging to resolve the four-fold fermion using XR-ARPES with limited energy and momentum resolutions, we can estimate its binding energy is $E_B \approx 0.20$ eV by comparing the overall features in the calculated and experimental results. Similar multifold band crossings at R and Γ points were also observed in PtAl and PdGa, all of which show good consistence with the first-principles calculation [Fig. 5.15].

5.2.4 Chiral surface states

Next, we used ARPES measurements with lower photon energies (<150 eV) to check the existence of SSs. In the energy-momentum dispersion around the six-fold fermion (R) of PtAl [Fig. 5.16(a)], distinguishable intensity is found between the bulk bands (indicated by the red arrow). According to the curvature plot, this

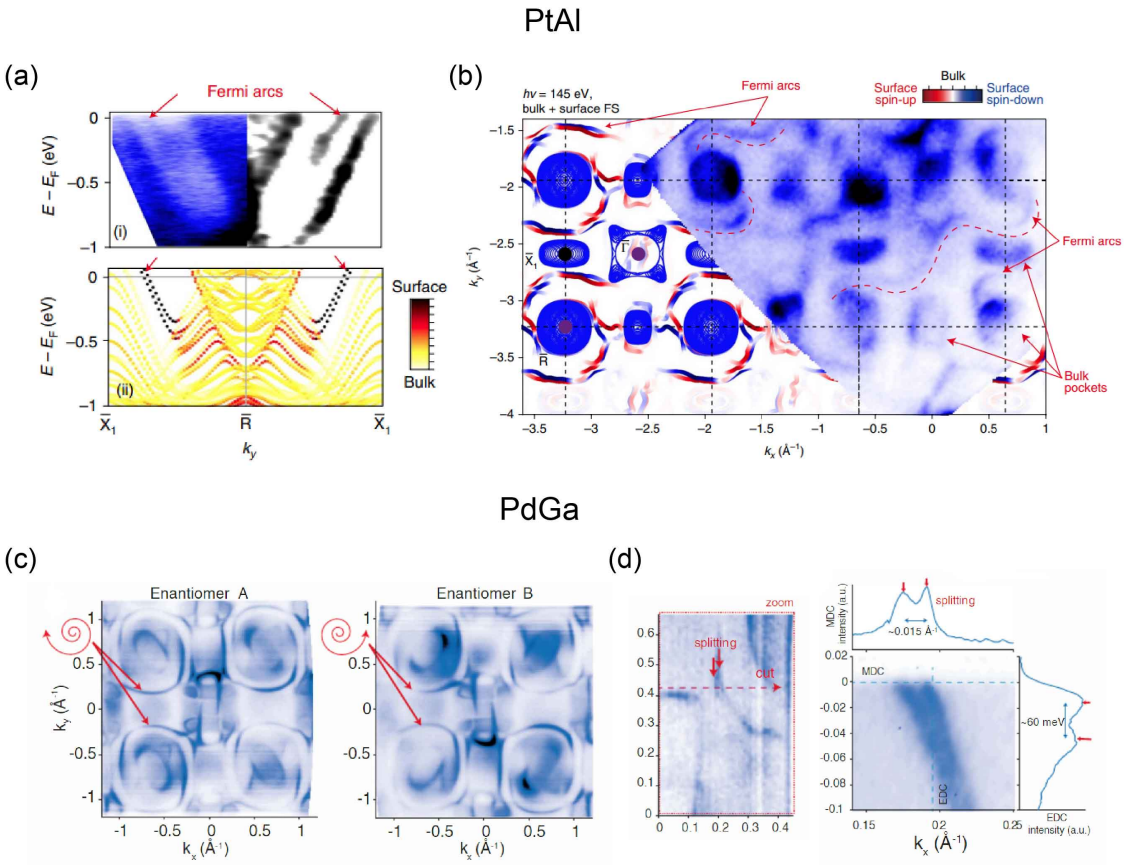

Figure 5.16: Surface states of PtAl and PdGa.(a) (i) Experimental band dispersion along the X-R-X direction (raw data on the left and curvature plot on the right). (ii) Corresponding ab initio slab calculation. (b) Experimental Fermi surface map, overlapped with ab initio slab calculations (blue and red lines), as well as the projected bulk calculations (blue contours). Red dashed lines are used to indicate the arc states. (c) Chiral arc SSs in samples with different handedness. (d) Band splitting to show the doublet arc states. Figures are adapted from [20, 105]

intensity can be recognized as an additional band, which corresponds to SSs in the slab calculation. These SSs turn out to the chiral FSSs (highlighted by red dashed lines as guides to the eye) winding across the BZ, which connect the projection of the six-fold fermion (R) and four-fold fermion (Γ). This observation is further corroborated by our ab initio slab calculations, which are also shown in Fig. 5.16(b) (showing surface spin-up and spin-down bands as red and blue lines, respectively), and projected bulk band contours (solid blue lines), which match our experimental data. The qualitative consistence between the ARPES and calculation results strongly support that the Chern numbers associated with the six-fold fermion (R) and four-fold fermion (Γ) are non-zero.

To further validate that such multifold fermions have a Chern number of ± 4, we performed ARPES measurements on the polished PdGa samples. Due to the atomically flat surface, the FSSs show less band broadening. Details of the SSs, such Chinese-knot-like SSs around the Γ point and oval-shaped SSs around the R point, are clearly presented. Prominently, we observed the SOC-induced momentum splitting of ∼0.015 $Å^{-1}$ and energy splitting of 60meV in the FSSs. This observation confirms that the chiral arcs are doublet states, consistent with the magnitude (2) of Chern number carried by the Berry flux [Fig. 5.12], which is a strong evidence to support the Chern number of ± 4 at the six-fold and four-fold fermions. Moreover, the different orientations of FSSs in enantiomers A and B are observed, which demonstrates that ARPES is competent to distinguish to chirality of crystalline samples [Fig. 5.16(c)].

Further ARPES measurements on cleaved PtGa samples reveal curious polarization selection of the FSSs. Figure 5.17(a) present the calculated FFSs, where the upper and lower branches of the SSs connected to the Γ point are marked by the red and black arrows, respectively. Interestingly, ARPES intensity map acquired with circular minus (C-) polarization only show the upper branch and the circular plus (C+) counterpart only show the lower branch [Figs. 5.17(b)(c)], though the combined data [Fig. 5.17(d)] show similar features with the calculation. These results have been repeated on another sample in a nano-ARPES measurement [Figs. 5.17(e)-(i)], where the circular polarization (CL or CR) only presents one branch of the SSs while the linear polarization (LH or LV) presents both. This observation is different from the commonly observed circular dichroism in ARPES measurements [167–170], since one of the branches completely disappears under certain polarization, suggesting an intrinsic circular dichroism related to the chiral crystal structure of PtGa [170]. This circular-polarization selection rule could be either the intrinsic property of the chiral crystal, or related with the direction of Berry flux [145]. Detailed studies on this phenomenon will be performed in the future work.

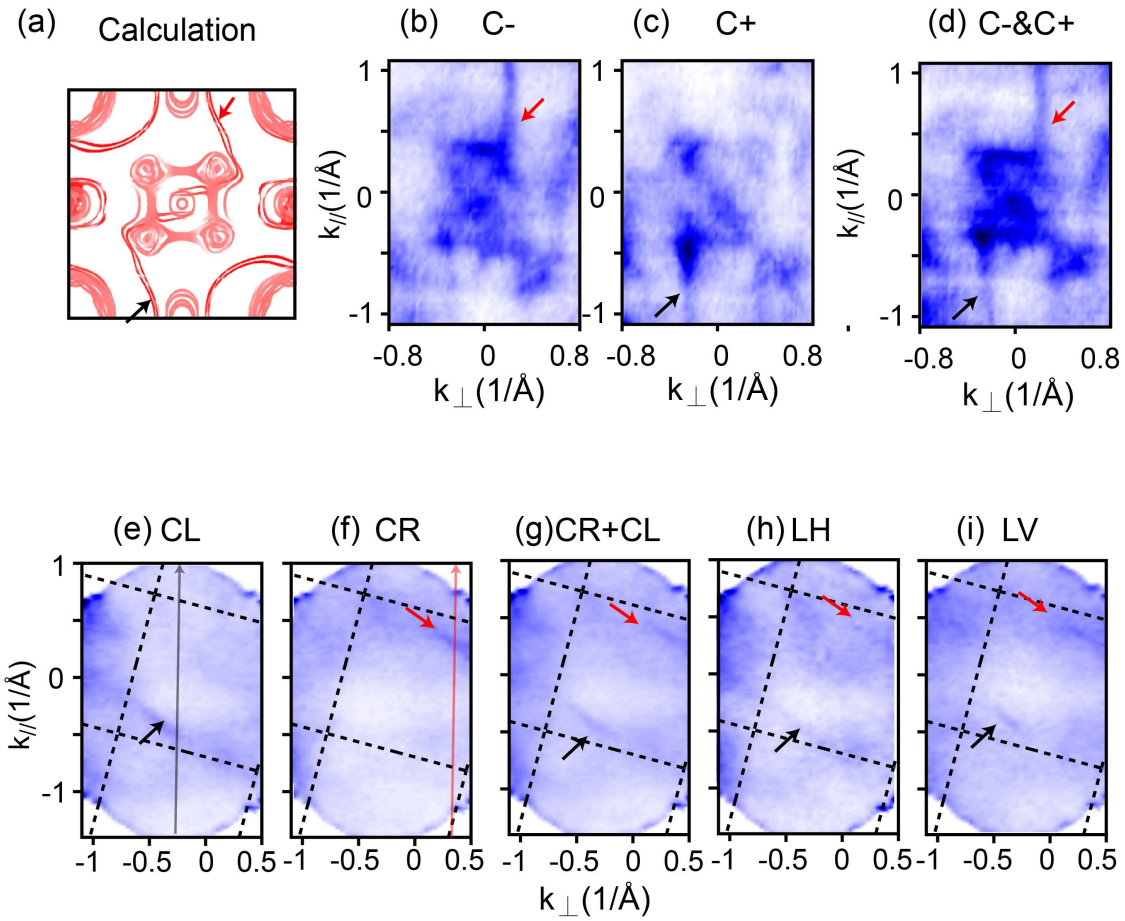

Figure 5.17: Surface states of PtGa.(a) Ab-initio calculated results of the FSSs. (b), (c) ARPES intensity maps at -0.5 eV measured with left-circular (C-) and right-circular (C+) polarization, respectively. (d) Combined data of (b) and (c). (e)-(i) ARPES intensity maps at -0.5 eV acquired with a nano-ARPES setup with different polarizations.

5.2.5 Summary

In summary, we have performed a systematic investigation on the electronic structure of PtGa family. By comparing the first-principles calculations with SX-ARPES data, we present the existence of six-fold and four-fold fermions at the R and Γ points, respectively. By visualizing the doublet FSSs, we confirm the Chern number of ± 4 associated with these multiple fermions. The polarization dependent measurements further reveal the selection rule on FSSs that is possibly related with the direction of Berry flux, which needs further experimental evidence to validate.

6
Summary

Contents

6.1 Summary

This thesis summarizes the projects that I have led or participated in during my four-year DPhil study in Oxford. In the first-two years, I mainly worked on single crystalline materials, including BiCuChO family and PtGa family, by performing regular ARPES measurements. The turning point of my Dphil was a conference, named Moiré in Paris, during which I happened to know the discovery of strongly-correlated and zero-resistance states in twisted bilayer WSe_2 (a talk given by Philip Kim). Since then, I have been working on low-dimensional systems, including twisted graphene, twisted TMDs and various 2D heterostructures, by performing nano-ARPES measurements.

In Chapter 1, we deliver a general introduction on ARPES techniques, including basic principles, equipment for synchrotron-based facilities and the experimental methods. This chapter provides the necessary background knowledge for the readers who are not familiar with ARPES and is meant to serve as a tutorial for the beginners in this field.

In Chapter 2, an overview of twisted 2D materials is presented. We briefly introduce the crystal structure and electronic structure of commonly used building blocks for 2D heterostructures, namely graphene and TMDs. Then we describe how twist affects the electronic structure of 2D heterostructures from three aspects, overlapping of interlayer orbitals, band crossing in the momentum space and Umklapp scattering induced by the competing order. Next, we introduce the moiré physics in twisted 2D materials, which is, simply speaking, twist-induced band folding and related exotic phenomena. This chapter equips readers with basic understanding of twisted 2D materials and their electronic structures.

In Chapter 3, we present a systematic investigation on the electronic structure of twisted bilayer WSe_2, by using nano-ARPES, STM and calculation. Our initial aim was to search for the K-valley flat band that is believed as the reason for the strongly correlated phases. However, it turns out that neither of our ARPES nor STM results show obvious evidence for the proposed K-valley flat band. On the

other hand, our results clearly show the Γ-valley moiré, which is associated with honeycomb- and kagome-shaped charge distribution in the real space.

In Chapter 4, we present the study of Umklapp scattering in graphene-based heterostructures, including twisted multi-layer graphene and twisted graphene/WSe_2 heterostructures. The direct observation of replica Dirac cones inside the first Brillouin zone indicates that Umklapp scattering is a universal process in graphene-based heterostructures. Curiously, the signature of flat band has been observed in the graphene/tbWSe_2 heterostructure, which hints the potential for designing flat bands by using the second order Umklapp scattering.

In Chapter 5, we describe the regular-ARPES study on single crystalline materials. In BiCuChO family, we find the dispersionless bands near the valence band top could be the origin of their excellent thermoelectric performance. In PtGa family, we confirm the topological non-triviality by presenting the chiral arc surface states with SOC-induced splitting.

In the next 2-3 years (or longer time), I will continue my research on 2D heterostructures. Some unsolved problems in my current projects will be further investigated, including the absence of K-valley flat bands in twisted bilayer WSe_2, the properties of flat bands in graphene/TMD heterostructures and the polarization-dependence in PtGa.

References

[1] S. Hufner. *Photoelectron Spectroscopy, Third Edition*. Springer, 2003.

[2] H. Yang et al. "Visualizing electronic structures of quantum materials by angle-resolved photoemission spectroscopy". In: *Nature Reviews Materials* 3.9 (2018), pp. 341–353.

[3] B. Lv, T. Qian, and H. Ding. "Angle-resolved photoemission spectroscopy and its application to topological materials". In: *Nature Reviews Physics* 1.10 (2019), pp. 609–626.

[4] J. A. Sobota, Y. He, and Z.-X. Shen. "Electronic structure of quantum materials by angle-resolved photoemission spectroscopy". In: *Reviews of Modern Physics* 93.4 (2021), pp. 1–93.

[5] A. Damascelli, Z. Hussain, and Z.-X. Shen. "Angle-resolved photoemission studies of the cuprate superconductors". In: *Reviews of Modern Physics* 75.2 (2003), pp. 473–541.

[6] M. Hengsberger et al. "Photoemission momentum mapping and wave function analysis of surface and bulk states on flat Cu(111) and stepped Cu(443) surfaces: A two-photon photoemission study". In: *Physical Review B* 77 (8 2008), p. 085425.

[7] V. N. Strocov et al. "Soft-X-ray ARPES facility at the ADRESS beamline of the SLS: Concepts, technical realisation and scientific applications". In: *Journal of synchrotron radiation* 21.1 (2014), pp. 32–44.

[8] D. K. Saldin and J. C. H. Spence. "On the mean inner potential in high-and low-energy electron diffraction". In: *Ultramicroscopy* 55.4 (1994), pp. 397–406.

[9] T. Åberg. "Theory of X-Ray Satellites". In: *Physical Review* 156 (1 1967), pp. 35–41.

[10] P. H. Citrin, G. K. Wertheim, and Y. Baer. "Many-body processes in x-ray photoemission line shapes from Li, Na, Mg, and Al metals". In: *Physical Review B* 16 (10 1977), pp. 4256–4282.

[11] M. A. Brisk and A.D. Baker. "Shake-up satellites in X-ray photoelectron spectroscopy". In: *Journal of Electron Spectroscopy and Related Phenomena* 7.3 (1975), pp. 197–213.

[12] S. Moser. "An experimentalist's guide to the matrix element in angle resolved photoemission". In: *Journal of Electron Spectroscopy and Related Phenomena* 214.1 (2017), pp. 29–52.

[13] H. Iwasawa. "High-resolution angle-resolved photoemission spectroscopy and microscopy". In: *Electronic Structure* 2.4 (2020), p. 043001.

[14] M. Hoesch et al. "A facility for the analysis of the electronic structures of solids and their surfaces by synchrotron radiation photoelectron spectroscopy". In: *Review of Scientific Instruments* 88.1 (2017), p. 013106.

[15] R. J. Koch et al. "Nano focusing of soft X-rays by a new capillary mirror optic". In: *Synchrotron Radiation News* 31.4 (2018), pp. 50–52.

[16] P. Dudin et al. "Angle-resolved photoemission spectroscopy and imaging with a submicrometre probe at the SPECTROMICROSCOPY-3.2L beamline of Elettra". In: *Journal of Synchrotron Radiation* 17.4 (2010), pp. 445–450.

[17] C. Liu. "Electronic structure of iron arsenic high temperature superconductors studied by angle resolved photoemission spectroscopy (ARPES)". In: (2011).

[18] ScientaOmicron. *Information for DA30-L-8000*. 2021. URL: `https://scientaomicron.com/en/Components/Electron-Analysers/DA30-L` (visited on 01/22/2021).

[19] P. Sessi et al. "Handedness-dependent quasiparticle interference in the two enantiomers of the topological chiral semimetal PdGa". In: *Nature Communications* 11.1 (2020), p. 3507.

[20] N. B. M. Schröter et al. "Observation and control of maximal Chern numbers in a chiral topological semimetal". In: *Science* 369.6500 (2020), pp. 179–183.

[21] A. K. Geim and I. V. Grigorieva. "Van der Waals heterostructures". In: *Nature* 499.7459 (2013), pp. 419–425.

[22] A. K. Geim and K. S. Novoselov. "The rise of graphene". In: *Nature Materials* 6.3 (2007), pp. 183–191.

[23] K. S. Novoselov et al. "Electric field effect in atomically thin carbon films". In: *Science* 306.5696 (2004), pp. 666–669.

[24] Q. H. Wang et al. "Electronics and optoelectronics of two-dimensional transition metal dichalcogenides". In: *Nature Nanotechnology* 7.11 (2012), pp. 699–712.

[25] K. Zhang et al. "Two dimensional hexagonal boron nitride (2D-hBN): synthesis, properties and applications". In: *Journal of Materials Chemistry C* 5.46 (2017), pp. 11992–12022.

[26] Y. Zhan et al. "Large-area vapor-phase growth and characterization of MoS_2 atomic layers on a SiO_2 substrate". In: *Small* 8.7 (2012), pp. 966–971.

[27] A. Reina et al. "Large area, few-layer graphene films on arbitrary substrates by chemical vapor deposition". In: *Nano Letters* 9.1 (2009), pp. 30–35.

[28] H. J. Liu et al. "Molecular-beam epitaxy of monolayer and bilayer WSe_2 : a scanning tunneling microscopy/spectroscopy study and deduction of exciton binding energy". In: *2D Materials* 2.3 (2015), p. 034004.

[29] Q. Feng et al. "Growth of $MoS_{2(1-2x)}Se_{2x}$ (x = 0.41–1.00) monolayer alloys with controlled morphology by physical vapor deposition". In: *ACS Nano* 9.7 (2015), pp. 7450–7455.

[30] G. Eda et al. "Photoluminescence from chemically exfoliated MoS_2". In: *Nano Letters* 11.12 (2011), pp. 5111–5116.

[31] V. N. Kotov et al. "Electron-electron interactions in graphene: current status and perspectives". In: *Reviews of Modern Physics* 84.3 (2012), pp. 1067–1125.

[32] W. Shi et al. "Superconductivity series in transition metal dichalcogenides by ionic gating". In: *Scientific Reports* 5.1 (2015), p. 12534.

[33] B. Sipos et al. "From Mott state to superconductivity in 1T-TaS_2". In: *Nature Materials* 7.12 (2008), pp. 960–965.

[34] X. X. Xi et al. "Gate tuning of electronic phase transitions in two-dimensional $NbSe_2$". In: *Physical Review Letters* 117.10 (2016).

[35] Y. Zhang et al. "Experimental observation of the quantum Hall effect and Berry's phase in graphene". In: *Nature* 438.7065 (2005), pp. 201–204.

[36] E. Y. Andrei and A. H. MacDonald. "Graphene bilayers with a twist". In: *Nature Materials* 19.12 (2020), pp. 1265–1275.

[37] Y. Cao et al. "Correlated insulator behaviour at half-filling in magic-angle graphene superlattices". In: *Nature* 556.7699 (2018), pp. 80–84.

[38] X. Lu et al. "Superconductors, orbital magnets and correlated states in magic-angle bilayer graphene". In: *Nature* 574.7780 (2019), pp. 653–657.

[39] Y. Cao et al. "Unconventional superconductivity in magic-angle graphene superlattices". In: *Nature* 556.7699 (2018), pp. 43–50.

[40] M. Yankowitz et al. "Tuning superconductivity in twisted bilayer graphene". In: *Science* 363.6431 (2019), p. 1059.

[41] M. Serlin et al. "Intrinsic quantized anomalous Hall effect in a moiré heterostructure". In: *Science* 367.6480 (2020), pp. 900–903.

[42] A. H. Castro Neto et al. "The electronic properties of graphene". In: *Reviews of Modern Physics* 81.1 (2009), pp. 109–162.

[43] Y. Hatsugai, T. Fukui, and H. Aoki. "Topological analysis of the quantum Hall effect in graphene: Dirac-Fermi transition across van Hove singularities and edge versus bulk quantum numbers". In: *Physical Review B* 74.20 (2006), p. 205414.

[44] D. W. Boukhvalov, M. I. Katsnelson, and A. I. Lichtenstein. "Hydrogen on graphene: Electronic structure, total energy, structural distortions and magnetism from first-principles calculations". In: *Physical Review B* 77.3 (2008), p. 035427.

[45] S. Manzeli et al. "2D transition metal dichalcogenides". In: *Nature Reviews Materials* 2.8 (2017), p. 17033.

[46] E. J. Sie et al. "Valley-selective optical Stark effect in monolayer WS_2". In: *Nature Materials* 14.3 (2015), pp. 290–294.

[47] K. F. Mak et al. "Atomically thin MoS_2: A new direct-gap semiconductor". In: *Physical Review Letters* 105.13 (2010), p. 136805.

[48] J. M. B. Lopes dos Santos, N. M. R. Peres, and A. H. Castro Neto. "Graphene bilayer with a twist: Electronic structure". In: *Physical Review Letters* 99.25 (2007), p. 256802.

[49] R. Bistritzer and A. H. MacDonald. "Moiré bands in twisted double-layer graphene". In: *Proceedings of the National Academy of Sciences* 108.30 (2011), pp. 12233–12237.

[50] Chao-Xing Liu, Shou-Cheng Zhang, and Xiao-Liang Qi. "The Quantum Anomalous Hall Effect: Theory and Experiment". In: *Annual Review of Condensed Matter Physics* 7.1 (2016), pp. 301–321.

[51] G. R. Chen et al. "Signatures of tunable superconductivity in a trilayer graphene moire superlattice". In: *Nature* 572.7768 (2019), p. 215.

[52] X. M. Liu et al. "Tunable spin-polarized correlated states in twisted double bilayer graphene". In: *Nature* 583.7815 (2020), p. 221.

[53] C. Shen et al. "Correlated states in twisted double bilayer graphene". In: *Nature Physics* 16.5 (2020), p. 520.

[54] L. Wang et al. “Correlated electronic phases in twisted bilayer transition metal dichalcogenides”. In: *Nature Materials* 19.8 (2020), pp. 861–866.

[55] K. Tran et al. “Evidence for moire excitons in van der Waals heterostructures”. In: *Nature* 567.7746 (2019), p. 71.

[56] K. L. Seyler et al. “Signatures of moire-trapped valley excitons in $MoSe_2/WSe_2$ heterobilayers”. In: *Nature* 567.7746 (2019), p. 66.

[57] C. H. Jin et al. “Observation of moire excitons in WSe_2/WS_2 heterostructure superlattices”. In: *Nature* 567.7746 (2019), p. 76.

[58] K. Xu et al. “The role of Anderson’s rule in determining electronic, optical and transport properties of transition metal dichalcogenide heterostructures”. In: *Physical Chemistry Chemical Physics* 20.48 (2018), pp. 30351–30364.

[59] W. Yin et al. “Tunable dipole and carrier mobility for a few layer Janus MoSSe structure”. In: *Journal of Materials Chemistry C* 6.7 (2018), pp. 1693–1700.

[60] P. Yeh et al. “Direct measurement of the tunable electronic structure of bilayer MoS_2 by interlayer twist”. In: *Nano Letters* 16.2 (2016), pp. 953–959.

[61] H. Peng et al. “Substrate doping effect and unusually large angle van Hove singularity evolution in twisted bi- and multilayer graphene”. In: *Advanced Materials* 29.27 (2017), p. 1606741.

[62] J. Ahn Sung et al. “Dirac electrons in a dodecagonal graphene quasicrystal”. In: *Science* 361.6404 (2018), pp. 782–786.

[63] M. Koshino and P. Moon. “Electronic properties of incommensurate atomic layers”. In: *Journal of the Physical Society of Japan* 84.12 (2015), p. 121001.

[64] M. Koshino. “Interlayer interaction in general incommensurate atomic layers”. In: *New Journal of Physics* 17.1 (2015), p. 015014.

[65] B. Amorim. “General theoretical description of angle-resolved photoemission spectroscopy of van der Waals structures”. In: *Physical Review B* 97.16 (2018), p. 165414.

[66] W. Yao et al. “Quasicrystalline 30° twisted bilayer graphene as an incommensurate superlattice with strong interlayer coupling”. In: *Proceedings of the National Academy of Sciences* 115.27 (2018), p. 6928.

[67] M. Angeli and A. H. MacDonald. “Gamma valley transition metal dichalcogenide moire bands”. In: *Proceedings of the National Academy of Sciences* 118.10 (2021), e2021826118.

[68] D. M. Kennes et al. “Moiré heterostructures as a condensed-matter quantum simulator”. In: *Nature Physics* 17.2 (2021), pp. 155–163.

[69] A. Ghiotto et al. “Quantum criticality in twisted transition metal dichalcogenides”. In: *arXiv 2103.09796* (2021).

[70] L. An et al. “Interaction effects and superconductivity signatures in twisted double-bilayer WSe_2”. In: *Nanoscale Horizons* 5.9 (2020), pp. 1309–1316.

[71] M. H. Naik and M. Jain. “Ultraflatbands and shear solitons in moire patterns of twisted bilayer transition metal dichalcogenides”. In: *Physical Review Letters* 121.26 (2018), p. 266401.

[72] F. Wu et al. “Topological insulators in twisted transition metal dichalcogenide homobilayers”. In: *Physical Review Letters* 122.8 (2019), p. 086402.

[73] T. Li et al. “Quantum anomalous Hall effect from intertwined moiré bands”. In: *arXiv 2107.01796* (2021).

[74] F. Wu et al. “Hubbard model physics in transition metal dichalcogenide moire bands”. In: *Physical Review Letters* 121.2 (2018), p. 026402.

[75] J. Liu and X. Dai. “Orbital magnetic states in moiré graphene systems”. In: *Nature Reviews Physics* 3.5 (2021), pp. 367–382.

[76] J. Kang and O. Vafek. “Symmetry, maximally localized wannier states, and a low-energy model for twisted bilayer graphene narrow bands”. In: *Physical Review X* 8.3 (2018), p. 031088.

[77] H. C. Po et al. “Origin of Mott insulating behavior and superconductivity in twisted bilayer graphene”. In: *Physical Review X* 8.3 (2018), p. 031089.

[78] N. P. Kazmierczak et al. “Strain fields in twisted bilayer graphene”. In: *Nature Materials* (2021), pp. 956–963.

[79] H. S. Arora et al. “Superconductivity in metallic twisted bilayer graphene stabilized by WSe_2”. In: *Nature* 583.7816 (2020), pp. 379–384.

[80] W. Jin et al. “Direct measurement of the thickness-dependent electronic band structure of MoS_2 using angle-resolved photoemission spectroscopy”. In: *Physical Review Letters* 111.10 (2013), p. 106801.

[81] Y. Zhang et al. “Direct observation of the transition from indirect to direct bandgap in atomically thin epitaxial $MoSe_2$”. In: *Nature Nanotechnology* 9.2 (2014), pp. 111–115.

[82] Y. Zhang et al. “Electronic structure, surface doping, and optical response in epitaxial WSe_2 thin films”. In: *Nano Letters* 16.4 (2016), pp. 2485–2491.

[83] T. Li et al. “Continuous Mott transition in semiconductor moiré superlattices”. In: *Nature* 597.7876 (2021), pp. 350–354.

[84] M. I. B. Utama et al. “Visualization of the flat electronic band in twisted bilayer graphene near the magic angle twist”. In: *Nature Physics* 17.2 (2021), pp. 184–188.

[85] S. Ulstrup et al. “Direct observation of minibands in a twisted graphene/WS_2 bilayer”. In: *Science Advances* 6.14 (2020), eaay6104.

[86] S. Lisi et al. “Observation of flat bands in twisted bilayer graphene”. In: *Nature Physics* 17.2 (2021), pp. 189–193.

[87] S. Xie et al. “Direct observation of distinct minibands in moiré superlattices”. In: *arXiv 2010.07806* (2020).

[88] A. J. H. Jones et al. “Visualizing band structure hybridization and superlattice effects in twisted MoS_2/WS_2 heterobilayers”. In: *arXiv 2106.00403* (2021).

[89] G. Kresse and J. Furthmuller. “Efficient iterative schemes for ab initio total-energy calculations using a plane-wave basis set”. In: *Physical Review B* 54.16 (1996), pp. 11169–11185.

[90] Y. Matsushita et al. “Unfolding energy spectra of double-periodicity two-dimensional systems: Twisted bilayer graphene and MoS_2 on graphene”. In: *Physical Review Materials* 2.1 (2018), p. 010801.

[91] H. Li et al. “Imaging moire flat bands in three-dimensional reconstructed WSe_2/WS_2 superlattices”. In: *Nature Materials* (2021), pp. 945–950.

[92] C. Zhang et al. “Probing critical point energies of transition metal dichalcogenides: Surprising indirect gap of single layer WSe_2”. In: *Nano Letters* 15.10 (2015), pp. 6494–6500.

[93] Z. Zhang et al. “Flat bands in twisted bilayer transition metal dichalcogenides”. In: *Nature Physics* 16.11 (2020), pp. 1093–1096.

[94] H. Nishi, Y. Matsushita, and A. Oshiyama. “Band-unfolding approach to moiré-induced band-gap opening and Fermi level velocity reduction in twisted bilayer graphene”. In: *Physical Review B* 95.8 (2017), p. 085420.

[95] E. Tang, J. Mei, and X. Wen. “High-temperature fractional quantum Hall states”. In: *Physical Review Letters* 106.23 (2011), p. 236802.

[96] T. Neupert et al. “Fractional quantum Hall states at zero magnetic field”. In: *Physical Review Letters* 106.23 (2011), p. 236804.

[97] N. W. Ashcroft and N. D. Mermin. *Solid State Physics*. 1976, pp. 523–528.

[98] A. J. Graham et al. “Ghost anti-crossings caused by interlayer umklapp hybridization of bands in 2D heterostructures”. In: *2D Materials* 8.1 (2020), p. 015016.

[99] C. M. Polley et al. “Origin of the π-band replicas in the electronic structure of graphene grown on $4H$-SiC(0001)”. In: *Physical Review B* 99.11 (2019), p. 115404.

[100] S. Ulstrup et al. “Direct observation of minibands in a twisted graphene/WS_2 bilayer”. In: *Science Advances* 6.14 (2020), eaay6104.

[101] J. M. Cowley and A. F. Moodie. “The scattering of electrons by atoms and crystals. I. A new theoretical approach”. In: *Acta Crystallographica* 10.10 (1957), pp. 609–619.

[102] J. Voit et al. “Electronic structure of solids with competing periodic potentials”. In: *Science* 290.5491 (2000), pp. 501–503.

[103] B. Deng et al. “Interlayer decoupling in 30° twisted bilayer graphene quasicrystal”. In: *ACS Nano* 14.2 (2020), pp. 1656–1664.

[104] D. Pei et al. “Electronic structure of a thermoelectric material: BiCuSO”. In: *Physical Review B* 103 (24 2021), p. 245121.

[105] N. B. M. Schroter et al. “Chiral topological semimetal with multifold band crossings and long Fermi arcs”. In: *Nature Physics* 15.8 (2019), pp. 759–765.

[106] G. J. Snyder and E. S. Toberer. “Complex thermoelectric materials”. In: *Nature Materials* 7.2 (2008), pp. 105–114.

[107] L.-D. Zhao et al. “BiCuSeO oxyselenides: new promising thermoelectric materials”. In: *Energy and Environmental Science* 7.9 (2014), pp. 2900–2924.

[108] R. Viennois et al. “Lattice dynamics study of thermoelectric oxychalcogenide BiCuChO (Ch = Se, S)”. In: *The Journal of Physical Chemistry C* 123.26 (2019), pp. 16046–16057.

[109] S. Kumar and U. Schwingenschlogl. “Lattice thermal conductivity in layered BiCuSeO”. In: *Physical Chemistry Chemical Physics* 18.28 (2016), pp. 19158–64.

[110] Y. Liu et al. “Remarkable enhancement in thermoelectric performance of BiCuSeO by Cu deficiencies”. In: *Journal of the American Chemical Society* 133.50 (2011), pp. 20112–5.

[111] Y. Liu et al. “Synergistically optimizing electrical and thermal transport properties of BiCuSeO via a dual-doping approach”. In: *Advanced Energy Materials* 6.9 (2016), p. 1502423.

[112] J. Li et al. “Thermoelectric properties of Mg doped p-type BiCuSeO oxyselenides”. In: *Journal of Alloys and Compounds* 551 (2013), pp. 649–653.

[113] J. L. Lan et al. “Enhanced thermoelectric properties of Pb-doped BiCuSeO ceramics”. In: *Advanced Materials* 25.36 (2013), pp. 5086–90.

[114] C. Barreteau et al. “Structural and electronic transport properties in Sr-doped BiCuSeO”. In: *Chemistry of Materials* 24.16 (2012), pp. 3168–3178.

[115] J. Labegorre et al. “Electronic band structure engineering and enhanced thermoelectric transport properties in Pb-doped BiCuOS oxysulfide”. In: *Chemistry of Materials* 30.3 (2018), pp. 1085–1094.

[116] G. K. Ren et al. “Complex electronic structure and compositing effect in high performance thermoelectric BiCuSeO”. In: *Nature Communications* 10.1 (2019), p. 2814.

[117] Y. Pei et al. “High thermoelectric performance of oxyselenides: intrinsically low thermal conductivity of Ca-doped BiCuSeO”. In: *NPG Asia Materials* 5.5 (2013), e47–e47.

[118] D. Zou et al. “Electronic structures and thermoelectric properties of layered BiCuOCh oxychalcogenides (Ch = S, Se and Te): first-principles calculations”. In: *Journal of Materials Chemistry A* 1.31 (2013), p. 8888.

[119] A. Ubaldini et al. “BiOCuS: A new superconducting compound with oxypnictide-related structure”. In: *Physica C: Superconductivity and its applications* 470 (2010), S356–S357.

[120] I. I. Mazin. “Superconductivity and magnetism in CuBiSO from first principles”. In: *Physical Review B* 81.14 (2010), 140508(R).

[121] I. R. Shein and A. L. Ivanovskii. “Electronic band structure and inter-atomic bonding in tetragonal BiOCuS as a parent phase for novel layered superconductors”. In: *Solid State Communications* 150.13-14 (2010), pp. 640–643.

[122] L. Ortenzi et al. “Competition between electron-phonon coupling and spin fluctuations in superconducting hole-doped CuBiSO”. In: *Physical Review B* 83.10 (2011), 100505(R).

[123] A. Pal, H. Kishan, and V. P. S. Awana. “Synthesis and structural details of $BiOCu_{1-x}S$: Possible new entrant in a series of exotic superconductors?” In: *Journal of Superconductivity and Novel Magnetism* 23.3 (2010), pp. 301–304.

[124] D. Berthebaud et al. “The $BiCu_{1-x}OS$ oxysulfide: Copper deficiency and electronic properties”. In: *Journal of Solid State Chemistry* 237 (2016), pp. 292–299.

[125] S. K. Karna et al. “Interplay between the crystalline and magnetic structures in $BiOCu_{0.94}S$”. In: *Journal of the Physical Society of Japan* 80.SB (2011), p. 011.

[126] S. K. Karna et al. “Spin, charge and lattice couplings in Cu-deficient oxysulphide $BiOCu_{0.94}S$”. In: *Journal of Physics: Condensed Matter* 24.26 (2012), p. 266004.

[127] D. Berardan et al. “Structure and transport properties of the BiCuSeO-BiCuSO solid solution”. In: *Materials (Basel)* 8.3 (2015), pp. 1043–1058.

[128] H. Zhu et al. “High pressure synthesis, structure and thermoelectric properties of BiCuChO (Ch = S, Se, Te)”. In: *Journal of the European Ceramic Society* 37.4 (2017), pp. 1541–1546.

[129] J. Gamon et al. “Mechanochemical synthesis of iodine-substituted BiCuOS”. In: *Journal of Solid State Chemistry* 263 (2018), pp. 157–163.

[130] S.-S. Chen et al. “Comparisons of electrical/magneto-transport properties of degenerate semiconductors BiCuXO (X=S, Se and Te) and their electron-phonon-interaction evolution”. In: *Journal of Applied Physics* 126.5 (2019), p. 055108.

[131] L. Xu et al. “An electronic phase diagram of hole-doped BiCuSeO crystals determined by transport characterization under various growth conditions”. In: *CrystEngComm* 23.2 (2021), pp. 273–281.

[132] J. Heyd and G. E. Scuseria. “Assessment and validation of a screened Coulomb hybrid density functional”. In: *Journal of Chemical Physics* 120.16 (2004), pp. 7274–80.

[133] L. X. Yang et al. “Surface and bulk electronic structures of LaFeAsO studied by angle-resolved photoemission spectroscopy”. In: *Physical Review B* 82.10 (2010), p. 104519.

[134] S. Kawaji. “Weak localization and negative magnetorsistance in semiconductor two-dimensinal systems”. In: *Surface Science* 170 (1986), p. 682.

[135] W. Kutzelnigg and J. D. M. III. “Hund’s rules”. In: *Journal of Physics D* 36 (1996), pp. 197–214.

[136] Robert B. Griffiths. “Nonanalytic Behavior Above the Critical Point in a Random Ising Ferromagnet”. In: *Physical Review Letters* 23 (1 1969), pp. 17–19.

[137] C. M. Varma. “Mixed-valence compounds”. In: *Reviews of Modern Physics* 48.2 (1976), pp. 219–238.

[138] K. Kuroki and R. Arita. ““Pudding mold” band drives large thermopower in Na_xCoO_2”. In: *Journal of the Physical Society of Japan* 76.8 (2007), p. 083707.

[139] M. Cardona and Eds. L. Ley. *Photoemission in solids I: General principles*. 1st. Berlin: Springer-Verlag, 1978.

[140] H. Lohani et al. “Band inversion and topology of the bulk electronic structure in $FeSe_{0.45}Te_{0.55}$”. In: *Physical Review B* 101 (24 2020), pp. 245146–245156.

[141] M. Ochi et al. “Thermoelectric performance of materials with $CuCh_4$ (Ch=S, Se) tetrahedra: Similarities and differences among their low-dimensional electronic structure from first principles”. In: *Physical Review Materials* 2.8 (2018), p. 085401.

[142] C. Lee et al. “Seebeck coefficients of layered BiCuSeO phases: Analysis of their hole-density dependence and quantum confinement effect”. In: *Chemistry of Materials* 29.5 (2017), pp. 2348–2354.

[143] M. S Dresselhaus et al. "New directions for low-dimensional thermoelectric materials". In: *Advanced Materials* 19.8 (2007), pp. 1043–1053.

[144] L. D. Hicks and M. S. Dresselhaus. "Thermoelectric figure of merit of a one-dimensional conductor". In: *Physical Review B* 47.24 (1993), pp. 16631–16634.

[145] H. D Flack. "Chiral and achiral crystal structures". In: *Helvetica Chimica Acta* 86.4 (2003), pp. 905–921.

[146] G. Chang et al. "Topological quantum properties of chiral crystals". In: *Nature Materials* 17.11 (2018), pp. 978–985.

[147] J. B. Pendry. "A chiral route to negative refraction". In: *Science* 306.5700 (2004), pp. 1353–1355.

[148] T. Morimoto and N. Nagaosa. "Chiral anomaly and giant magnetochiral anisotropy in noncentrosymmetric Weyl semimetals". In: *Physical Review Letters* 117.14 (2016), p. 146603.

[149] G. L. J. A. Rikken, J. Fölling, and P. Wyder. "Electrical Magnetochiral Anisotropy". In: *Physical Review Letters* 87.23 (2001), p. 236602.

[150] S. Mühlbauer et al. "Skyrmion lattice in a chiral magnet". In: *Science* 323.5916 (2009), pp. 915–919.

[151] M. Carnicom Elizabeth et al. "$TaRh_2B_2$ and $NbRh_2B_2$: Superconductors with a chiral noncentrosymmetric crystal structure". In: *Science Advances* 4.5 (2018), eaar7969.

[152] B. Bradlyn et al. "Beyond Dirac and Weyl fermions: Unconventional quasiparticles in conventional crystals". In: *Science* 353.6299 (2016), aaf5037.

[153] Q. Tang P.and Zhou and S.-C. Zhang. "Multiple types of topological fermions in transition metal silicides". In: *Physical Review Letters* 119.20 (2017), p. 206402.

[154] G. Chang et al. "Unconventional Chiral Fermions and Large Topological Fermi Arcs in RhSi". In: *Physical Review Letters* 119.20 (2017), p. 206401.

[155] J. Z. Ma et al. "Observation of a singular Weyl point surrounded by charged nodal walls in PtGa". In: *Nature Communications* 12.1 (2021), p. 3994.

[156] M. Yao et al. "Observation of giant spin-split Fermi-arc with maximal Chern number in the chiral topological semimetal PtGa". In: *Nature Communications* 11.1 (2020), p. 2033.

[157] Z. Rao et al. "Observation of unconventional chiral fermions with long Fermi arcs in CoSi". In: *Nature* 567.7749 (2019), pp. 496–499.

[158] D. S. Sanchez et al. "Topological chiral crystals with helicoid-arc quantum states". In: *Nature* 567.7749 (2019), pp. 500–505.

[159] Z. Ni et al. "Giant topological longitudinal circular photo-galvanic effect in the chiral multifold semimetal CoSi". In: *Nature Communications* 12.1 (2021), p. 154.

[160] H. Li et al. "Chiral fermion reversal in chiral crystals". In: *Nature Communications* 10.1 (2019), p. 5505.

[161] M. Z. Hasan and C. L. Kane. "Colloquium: Topological insulators". In: *Reviews of Modern Physics* 82.4 (2010), pp. 3045–3067.

[162] Y. L. Chen et al. “Experimental realization of a three-dimensional topological insulator, Bi_2Te_3”. In: *Science* 325.5937 (2009), pp. 178–181.

[163] Z. K. Liu et al. “Discovery of a Three-Dimensional Topological Dirac Semimetal, Na_3Bi”. In: *Science* 343.6173 (2014), pp. 864–867.

[164] Z. K. Liu et al. “A stable three-dimensional topological Dirac semimetal Cd_3As_2”. In: *Nature Materials* 13.7 (2014), pp. 677–681.

[165] L. X. Yang et al. “Weyl semimetal phase in the non-centrosymmetric compound TaAs”. In: *Nature Physics* 11.9 (2015), pp. 728–732.

[166] Z.-M. Yu et al. “Circumventing the no-go theorem: A single Weyl point without surface Fermi arcs”. In: *Physical Review B* 100.4 (2019), p. 041118.

[167] Y. H. Wang et al. “Observation of a warped helical spin texture in Bi_2Se_3 from circular dichroism angle-resolved photoemission spectroscopy”. In: *Physical Review Letters* 107.20 (2011), p. 207602.

[168] S. R. Park et al. “Chiral orbital-angular momentum in the surface states of Bi_2Se_3”. In: *Physical Review Letters* 108.4 (2012), p. 046805.

[169] M. R. Scholz et al. “Reversal of the circular dichroism in angle-resolved photoemission from Bi_2Te_3”. In: *Physical Review Letters* 110.21 (2013), p. 216801.

[170] C. H. Min et al. “Orbital fingerprint of topological Fermi arcs in the Weyl semimetal TaP”. In: *Physical Review Letters* 122.11 (2019), p. 116402.